Milestone 3468

An Unsaturated Zone Flow and Transport Model of Yucca Mountain

Bruce A. Robinson, Andrew V. Wolfsberg,
George A. Zyvoloski, Carl W. Gable

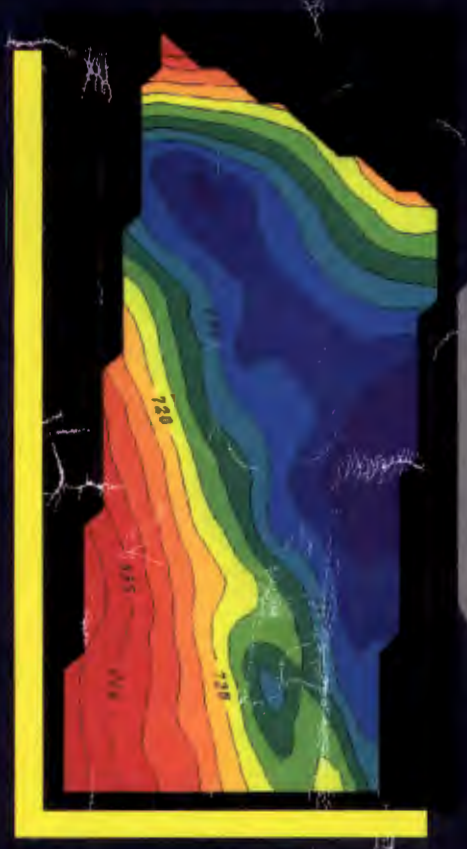

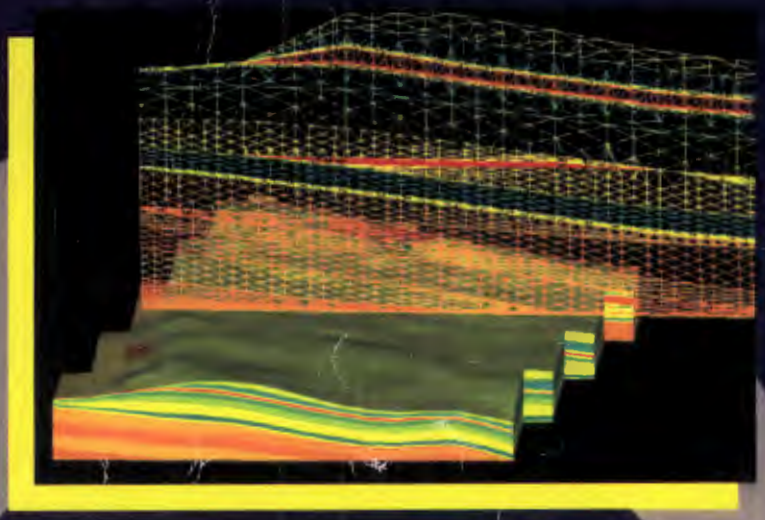

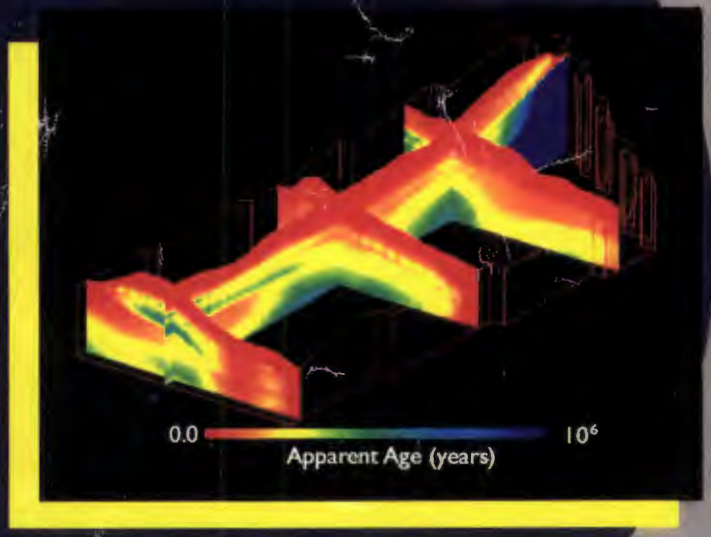

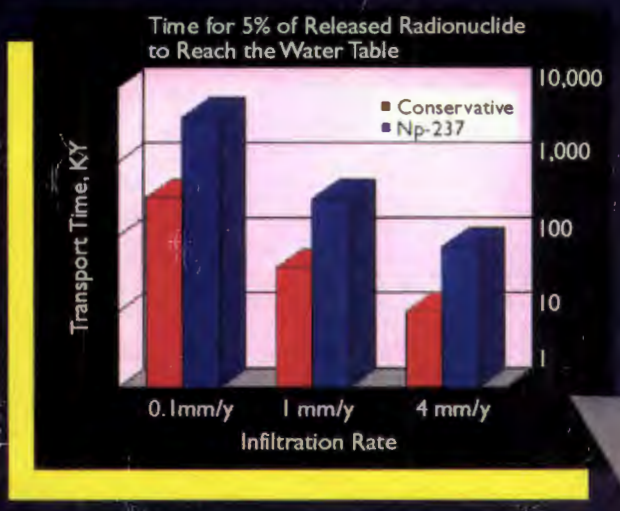

October 1995

Los Alamos

9666

DRAFT

LIBRARY COPY

MILESTONE 3468

An Unsaturated Zone Flow and Transport Model of Yucca Mountain

by

Bruce A. Robinson

Andrew V. Wolfsberg

George A. Zyvoloski

Carl W. Gable

DRAFT

Modification date: 11/8/95

DRAFT

Modification date: 11/8/95

TABLE OF CONTENTS

1.0 Introduction 13
1.1 Scope of Report 15

2.0 Laboratory Scale Measurements for Neptunium. 17
2.1 Solubility/Speciation Studies 17
2.2 Sorption Studies 18
2.3 Diffusion Studies 22
2.4 Column Transport Studies. 30

3.0 Hydrologic Considerations 37
3.1 Infiltration. 37
3.2 Delineation and Importance of Contrasting Permeabilities in Hydrostratigraphic Units. 38
3.3 Importance of Fractures and Faults 39
3.4 Evidence from isotopic tracers 40
3.5 Geochemical Composition Within Beds 43

4.0 Integration of Geologic Data of Structure and Stratigraphy into Flow and Transport Models 45
4.1 Grid Generation Goals 45
4.2 Development of Three-dimensional Hydrogeologic Framework Models. 45
4.3 Incorporating Data into Stratamodel 52
4.4 GEOMESH/X3D Grid Generation 54

5.0 Mathematical Methods Used in Transport Calculations 63
5.1 Hydrologic Flow Mathematical Models 63
5.2 Transport Mathematical Models 70

6.0 Site Scale Hydrologic Model Results 81
6.1 Summary of Previous Hydrologic Flow Modeling 81
6.2 Benchmarking the Los Alamos and LBL/USGS Flow Models. 81
6.3 Rationale for the Development of Hydrologic Solutions 85
6.4 Current Hydrologic Model Results. 86
6.5 Two-Dimensional Cross Section Simulations 87
6.6 Three-Dimensional Simulations 98
6.7 Chlorine-36 Simulations 102
6.8 Numerical Performance. 110

7.0 Neptunium Migration Results 117
7.1 Criteria Used for Assessing Neptunium Migration Rates 117
7.2 2-Dimensional Equivalent Continuum Calculations. 118
7.3 3-Dimensional Equivalent Continuum Calculations. 141
7.4 2-Dimensional Dual Permeability Calculations 144

8.0 Discussion and Conclusions 159
8.1 Hydrostratigraphic Characterization and Grid Generation 159
8.2 Hydrologic Conclusions. 160
8.3 Transport Results 162

9.0 References 171

Acknowlegements

This work was performed under the auspices of the Department of Energy, Yucca Mountain Site Characterization Project. In accordance with QP 5.1Q, there is no new data generated in this study. The authors would like to thank the following individuals who were of great assistance in putting together this report. Grid generation: Harold Trease, Terry Cherry; neptunium laboratory studies: Ines Triay; mineralogic description of the Calico Hills: Dave Vaniman, Dave Bish; description used in building the Stratamodel structural model: Bo Bodvarsson, LBL; environmental isotopes: June Fabryka-Martin; variable infiltration map: Alan Flint; FEHM simulations: Stephen Henderson. Kay Birdsell provided a thorough review that resulted in a much more readable, understandable document. We also thank the following people for assistance in the preparation of this document and the accompanying movie: Lynn Trease, Lynn McDonald, Corrine Tippett, Kay Coen. Finally, we greatly appreciate all of the efforts of Gilles Bussod in supporting this project.

Abstract

Site scale flow and transport calculations are presented for the unsaturated zone at Yucca Mountain, the proposed site of the Nation's first high level nuclear waste repository. The goal is to simulate the movement of key radionuclides, particularly ^{237}Np, from the potential repository to the water table. In the present study we integrate the relevant geochemical, hydrologic, and mineralogic data into a comprehensive numerical model for the transport of ^{237}Np through the unsaturated zone. Underpinning the model is the hydrostratigraphic understanding of the site, which controls the transport system because of the vast differences in hydrologic properties and mineralogy in the various layers. A combination of commercially available software and software developed at Los Alamos is used to perform the analyses, going from the construction of a model that honors the hydrostratigraphic and mineralogic information available for the site, to the generation of finite element computational grids upon which flow and transport calculations are made. The computer code Finite Element Heat and Mass (FEHM), a comprehensive simulator of flow and transport in two and three dimensions, is used in the flow and transport calculations of the present study. Three-dimensional simulations of the hydrologic system are compared to another flow model of the site unsaturated zone. Then, simulations of the movement of bomb-pulse ^{36}Cl and background ^{36}Cl are shown to agree qualitatively with the observed data, although an exact calibration of the model to these data is not yet possible. After reviewing in detail the extensive laboratory data base on ^{237}Np, we then present a series of two- and three-dimensional simulations of ^{237}Np transport from the potential repository to the water table. For most simulations, sorptive retardation of ^{237}Np delays the arrival at the water table by roughly an order of magnitude relative to a conservative solute. Sensitivity analyses are presented varying the position of release of the radionuclides, the sorption coefficient, and the impact of certain key uncertainties in the hydrologic parameters. The dual permeability model formulation is employed specifically to examine the role of fractures on transport. At high enough infiltration rates, substantial fracture flow is induced, but as a result of diffusion of ^{237}Np into the rock matrix, some of the negative aspects of fracture flow on waste isolation are mitigated Three-dimensional transport simulations indicate that significant lateral flow effects are present in three dimensions that are not observed in two-dimensional cross sections. As a result, three-dimensional calculations need to be included whenever possible to provide the most accurate predictions possible.

Executive Summary

Yucca Mountain, Nevada, is being studied by the U. S. Department of Energy as a potential site for the Nation's first high level nuclear waste repository. As part of the site characterization activities associated with the site, Los Alamos National Laboratory (LANL) scientists are studying the hydrologic and transport properties of the region around the potential repository location. This report summarizes modeling efforts aimed at simulating the movement of key radionuclides, particularly ^{237}Np, from the potential repository to the water table. This radionuclide is thought to be one of the more problematic radionuclides because of its large inventory, high solubility, and relatively low sorption coefficient on the Yucca Mountain tuffs. As a result, the scientists studying the geochemical aspects of the system consisting of the Yucca Mountain groundwater, rock, and radionuclides have performed comprehensive studies of solubility, speciation, sorption, and transport for ^{237}Np.

In the present study we integrate the relevant geochemical, geologic, hydrologic, and mineralogic data into a comprehensive numerical model for the transport of ^{237}Np through the unsaturated zone from the potential repository to the water table. Underpinning the model is the hydrostratigraphic understanding of the site, which controls the transport system because of the vast differences in hydrologic properties and mineralogy in the various layers. The description of the structure embodied in the LBL/USGS hydrologic model (Wittwer et al., 1994) is used as a starting point for the model calculations of the present study. The Calico Hills hydrogeologic unit beneath the potential repository was altered to better reflect the current information on this important geologic unit. Input from Project mineralogists was incorporated into this revised structural description of the Calico Hills unit.

The computer code Finite Element Heat and Mass (FEHM), a comprehensive simulator of flow and transport in two and three dimensions, is used in the flow and transport calculations of the present study. This code is intimately linked to the grid generation capability that produces finite element computational grids that honor the stratigraphic information for the site, allowing for automatic generation of grids that produce accurate numerical results. FEHM has the capability of simulating transport using either a finite element solution or a particle tracking solution, each of which are useful for examining various aspects of the transport system. Finally, the dual permeability capability of the code is an important tool for studying the role of fractures on flow and transport.

The GEOMESH software package is a powerful tool for generating finite element grids for flow and transport calculations. In the present study, three-dimensional calculations were performed on three grids: one to reproduce the LBL/USGS model for comparison purposes, one at a somewhat finer spatial resolution than the grid used for comparison, with the new representation of the Calico Hills, and a fine resolution grid with an additional level of discretization in the units beneath the potential

repository. In addition, a total of five two-dimensional grids were used: three at different degrees of resolution for an East-West cross section at Antler Ridge, one Antler Ridge cross section for a case in which the thicknesses of the zeolitic units were the maximum that could be justified by the field data, and one North-South cross section. The versatility and ease of use of the grid generation program used in the present study made it possible to use such a wide variety of computational grids.

On each of the two- and three-dimensional grids created for this study, steady state flow fields are computed, after which solute transport simulations were performed. Infiltration rates ranging from 0.1 mm/y to 4.0 mm/y as well a spatially nonuniform infiltration distribution are used in these simulations. For each infiltration rate, two different model formulations, the equivalent continuum and dual permeability methods, relating fracture and matrix characteristics are implemented. The resulting saturations for either method at a specified infiltration rate are similar, yet the resulting flow fields are substantially different. Flow paths through the unsaturated zone are visualized with simulations of the movement of tracers entering the flow system with the infiltrating water. With the dual permeability method, movement through the welded tuff near the ground surface is much more rapid than predicted with the equivalent continuum method. Also, substantially more lateral flow occurs, even under spatially uniform infiltration, with the dual permeability method. These differences are highlighted with simulations of bomb-pulse (post 1953) ^{36}Cl migration into the unsaturated zone. Only with the dual permeability method can the observed high ^{36}Cl signals measured at the bottom of and below the Tiva Canyon welded tuff be simulated. ^{36}Cl, with a half life of 301,000 years is also used as a natural tracer to help identify flow paths over a much longer time frame. Simulations of ^{36}Cl migration and radioactive decay on the three-dimensional flow field show the complex flow structure of the system which is strongly related to the structure of the hydrostratigraphy. These three-dimensional simulations show that in some locations in the study area, age inversions (younger water under older) may be expected. This result agrees with the soil moisture samples that have been collected and analyzed.

Regarding the transport of ^{237}Np and conservative solutes, the infiltration rate exerts a strong influence on the travel times of conservative radionuclides (such as ^{99}Tc) and sorbing radionuclides such as ^{237}Np. At an infiltration rate of 1 mm/y, the equivalent continuum model yields a median (50%) arrival time of between about 60-80 ky for a conservative solute and about 500-900 ky for ^{237}Np. The range depends on the position of release of the radionuclide. The ratio of conservative to ^{237}Np travel time is termed the Effective Retardation Factor (ERF). It represents the delay that can be attributed to sorptive retardation of ^{237}Np. The value of about 10 from these simulations is very typical of the simulations of the present study: there is roughly an order of magnitude difference in travel time between a conservative solute and ^{237}Np, a ratio that remains relatively constant (with a few exceptions) despite differences in the hydrologic system. Travel times scale approximately with

infiltration rate, and show interesting variations as a function of the position within the potential repository at which radionuclide is released.

The transport of ^{237}Np was also studied with respect to uncertainties in the sorptive behavior of the zeolitic units. The average sorption coefficient K_d used in the simulations was 2.5 cc/g in the zeolitic rocks and 0 elsewhere. In the K_d range from 1.1 to 3.9 cc/g, the travel time scaled approximately with the value of K_d, as expected. Assigning small sorption coefficient values (within the range suggested by the data) to the non-zeolitic rocks was shown to have a relatively minor impact on the travel times because the retardation is small compared to the large sorptive delay in the zeolitic units. The assumed thicknesses of the zeolitic units in the Calico Hills has some impact on the transport of ^{237}Np. Differences in thicknesses in the nominal versus maximum zeolites case are greatest in the West, and show little difference in the East. Thus the effects of this uncertainty on transport of ^{237}Np are seen mainly in the Western part of the unsaturated zone.

Both equivalent continuum and dual permeability models were used to explore various aspects of the transport system, and just as importantly, to determine qualitatively the uncertainty associated with our choice of conceptual models. The dual permeability model predicts much more significant lateral diversion of flow above the potential repository, at the contact between the TCw and PTn units. The impact that this has on the potential repository is significant: in general, less water percolates through the Western segment of the repository, and travel times increase accordingly. For example, 50% travel times of ^{237}Np at 1 mm/y for the dual permeability model range from about 1,000 ky to 6,000 ky for the Western Release points, while for the Eastern release points the times range from about 500 ky to 1400 ky.

Although the sensitivity of the transport system to assumptions about the hydrologic parameters of the system was not the major focus of the present study, we addressed a few key uncertainties in the flow behavior as they impact transport of ^{237}Np and other radionuclides. The fracture-matrix interaction term is crucial to predicting the transport behavior. If dual permeability flow models allow fractures to transmit flow at less than 100% matrix saturations, then the transport system results in more prevalent vertical, downward flow through the potential repository, thus mitigating some of the beneficial effects of lateral diversion above the potential repository horizon predicted in the base case dual permeability simulations. In another sensitivity analysis, the Ghost Dance fault was explicitly represented as a fault zone that acts as a drain for fluid moving laterally at the TCw-PTn contact. The resulting travel times for release points to the West of the fault were not significantly affected. Points to the East show longer travel times because the percolation rate through this segment of the potential repository is lower when the fault acts as a fluid drain.

An advantage of the dual permeability model formulation is that it allows for a more straightforward representation of rapid fracture transport using the particle tracking technique. Here

the matrix diffusion option of the particle tracking technique in FEHM was used to examine the effect of matrix diffusion coefficient on transport. The effect on a sorbing species such as ^{237}Np is profound. For radionuclides traveling in a fracture, the only mechanism allowing it to contact rock where it can sorb is matrix diffusion. Thus the travel times of ^{237}Np generally exhibit the beneficial effects of sorption even when significant fracture flow occurs. The value of the diffusion coefficient has the expected impact on the transport results: higher diffusion coefficients result in greater contact of ^{237}Np with the sorptive zeolites and, hence, longer travel times. By contrast, sorption of ^{237}Np on fracture walls appears to provide little additional delay in travel times. This conclusion may be due to the specific sorption model chosen, and only applies to ^{237}Np, rather than to all radionuclides.

Although many of the sensitivity analyses in the present study were carried out in two dimensions, a select number of three-dimensional radionuclide migration calculations were performed to assess whether differences might arise to make the two-dimensional analyses inaccurate or non-conservative. In general, there are three-dimensional effects, but except for a few instances described below, they should not invalidate the conclusions of the sensitivity analyses performed in two dimensions. In both equivalent continuum and dual permeability three-dimensional calculations, the three-dimensional simulations result in a greater degree of lateral diversion of flow. The impact on transport of radionuclides from the potential repository depends on the location of the lateral diversion. Much of this effect occurs above the potential repository, resulting in lower percolation fluxes through the repository horizon and longer travel times than in the two-dimensional calculations. There are also some effects observed in flow and transport beneath the potential repository due to increased lateral flow. For the latter case, conservative solute transport times increase dramatically, but in some cases, a fraction of the ^{237}Np bypasses the sorptive zeolitic units. It is uncertain whether this effect will be seen for all three-dimensional transport calculations or if it is an isolated result that will not be reproduced for different assumed model geometries and flow characteristics. Future simulation studies will address this issue.

Finally, the combination of grid generation capabilities of the Stratamodel/GEOMESH interface, when coupled to the FEHM flow and transport simulator, has proven to be a robust and versatile suite of software tools for modeling unsaturated zone flow and transport. The FEHM code has been shown to provide flow and transport solutions on grids containing up to 51,000 nodes and 300,000 elements in three dimensions for equivalent continuum, and 14,000 nodes and 80,000 elements in three dimensions for dual permeability.

The modeling analysis of unsaturated zone transport of ^{237}Np transport in the present study is not a complete analysis of all relevant transport processes from the potential repository to the accessible environment. First, saturated zone transport is not included as part of the analysis. When a similar modeling study is performed for the saturated zone, then the results of the present study can be

incorporated as a boundary condition to a saturated zone model. The ultimate goal is an unsaturated/ saturated zone model that will provide the most comprehensive numerical description of the entire transport system. Furthermore, the impact of repository heat on the thermohydrologic behavior and transport processes is not included in this modeling study. Thus the calculations are only strictly valid for transport that occurs after the effects of repository heat have dissipated. Despite these limitations, the simulations provide a comprehensive picture of the unsaturated zone transport of ^{237}Np under ambient conditions, which is an important step toward building a defensible model of radionuclide migration.

DRAFT

1.0 Introduction

Yucca Mountain, Nevada, is being studied by the U. S. Department of Energy as a potential site for the Nation's first high level nuclear waste repository. As part of the site characterization activities associated with the site, Los Alamos National Laboratory (LANL) scientists are studying the hydrologic and transport properties of the region around the potential repository location. The region of study includes the unsaturated zone where the potential repository may be located, and the saturated zone along the likely pathways to the accessible environment. These site characterization activities are part of a overall program strategy that applies equal weight to the engineered barrier and the geologic system as key components of a multiple barrier concept of waste isolation (DOE, 1995).

The unsaturated zone consists of alternating layers of welded and nonwelded tuffs that are tilted, uplifted, fractured, and faulted. Infiltration rates into the bedrock are thought to be low due to the low precipitation in the region and the large evapotranspiration rates. This percolating fluid is the primary carrier for most of the radionuclides of interest, which are soluble in water to some extent. For radionuclides to reach the accessible environment, the waste canisters must be breached and radionuclides must become mobilized by dissolution. They then must travel through the near field environment of backfill material (if used) and rock altered by thermally induced geochemical reactions, through the unsaturated rock beneath the potential repository, and subsequently through the saturated zone groundwater flow system. In addition to the hydrologic processes that obviously are important to radionuclide migration, transport processes such as sorption and physical retardation of radionuclides as they diffuse into dead-end pore space will control the ultimate movement of radionuclides in the geologic environment. Hydrologic and transport models must account for these processes in order to be credible.

The radionuclide of greatest interest in the present study is ^{237}Np. This radionuclide is thought to be one of the more problematic radionuclides because of its large inventory, high solubility and relatively low sorption coefficient on the Yucca Mountain tuffs. As a result, the scientists studying the geochemical processes of the chemical system consisting of the Yucca Mountain groundwater, rock, and radionuclides have performed comprehensive studies of solubility, speciation, sorption, and transport for ^{237}Np. This database of chemical behavior for ^{237}Np is being collected to provide a fundamental understanding of the transport characteristics needed for site scale transport modeling.

The goal of the present study is to integrate the relevant geochemical, hydrologic, and mineralogic data into a comprehensive numerical model for the transport of ^{237}Np through the unsaturated zone from the potential repository to the water table. Underpinning the model is the hydrostratigraphic understanding of the site, which controls the transport system because of the vast differences in hydrologic properties and mineralogy in the various layers. The description of the structure embodied in the LBL/USGS hydrologic model (Wittwer et al., 1995) is used as a starting point for the model

calculations of the present study. A map of the study region is shown in Figure 1-1.The structural description of Wittwer et al. (1995) did not adequately represent the Calico Hill hydrogeologic unit beneath the potential repository for our purposes, and thus was altered to better reflect the current information on this important geologic unit. Input from Project mineralogists was incorporated into

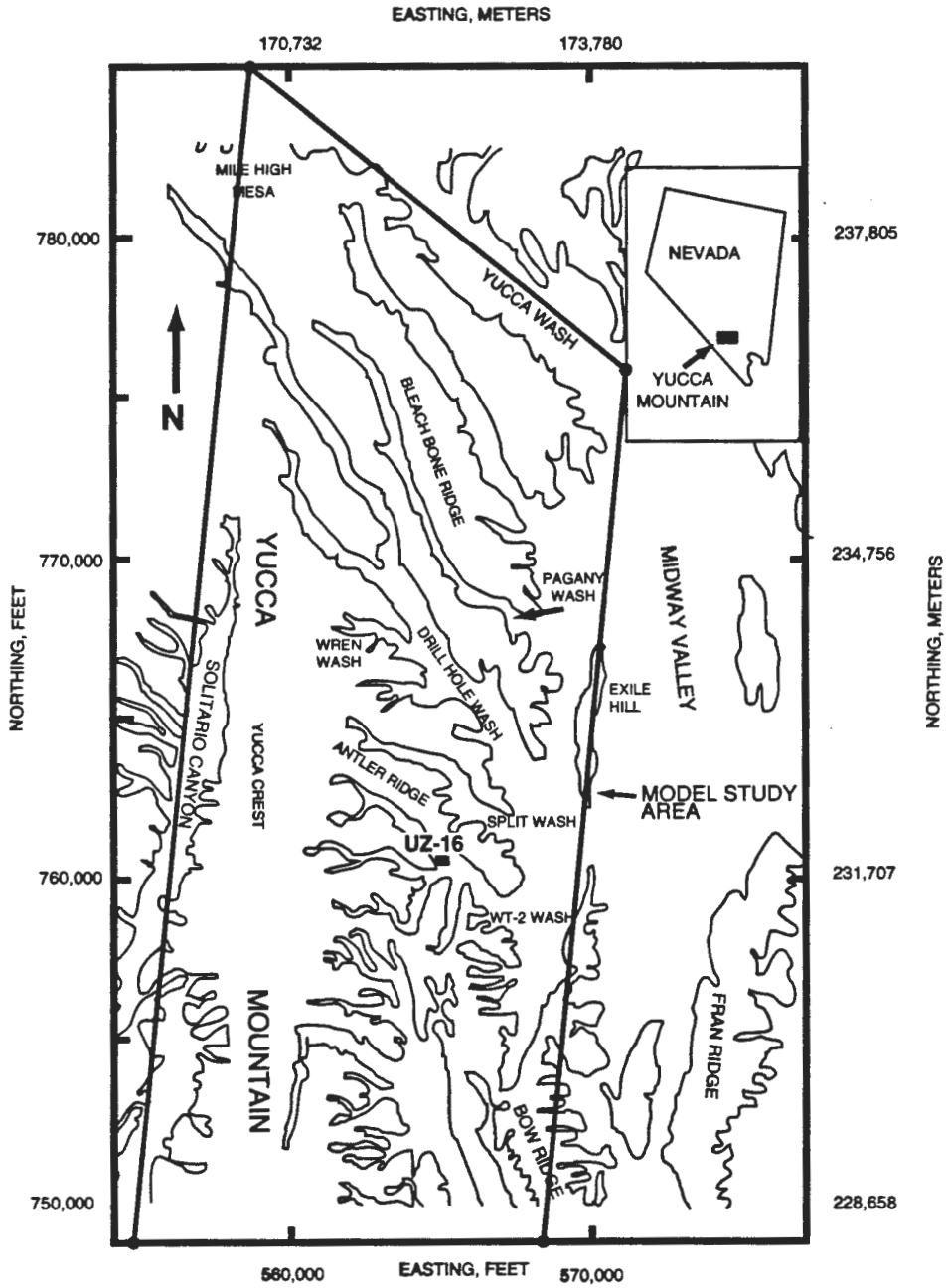

Figure 1-1.Map of the Model Study Area for the Unsaturated Zone Flow and Transport Model

DRAFT

this revised structural description of the Calico Hills unit. A sophisticated finite element grid generation program was used to ensure that the structural description is correctly incorporated into the numerical models. Next, the chemical data for ^{237}Np is synthesized to provide transport parameters for use in the numerical calculations. Finally, hydrologic information and conceptual models are input to the numerical model, with key uncertainties in parameters examined through sensitivity analyses. A key element of calibrating the hydrologic and transport model is the benchmarking against observations about the flow system based on environmental tracers such as ^{36}Cl.

The computer code Finite Element Heat and Mass (FEHM), a comprehensive simulator of flow and transport in two and three dimensions, is used in the flow and transport calculations of the present study. This code is intimately linked to the grid generation capability that produces finite element computational grids that honor the stratigraphic information on the site, allowing for automatic generation of grids that produce accurate numerical results. FEHM has the capability of simulating transport using either a finite element solution or a particle tracking solution, each of which are useful for examining various aspects of the transport system. Finally, the dual permeability capability of the code is an important tool for studying the role of fractures on flow and transport.

The modeling analysis of unsaturated zone transport of ^{237}Np transport in the present study is not a complete analysis of all relevant transport processes from the potential repository to the accessible environment. First, saturated zone transport is not included as part of the analysis. When a similar modeling study is performed for the saturated zone, then the results of the present study can be incorporated as a boundary condition to a saturated zone model. The ultimate goal is an unsaturated/ saturated zone model that will provide the most comprehensive numerical description of the entire transport system. Furthermore, the impact of repository heat on the thermohydrologic behavior and transport processes is not included in this modeling study. Thus the calculations are only strictly valid for transport that occurs after the effects of repository heat have dissipated. Despite these limitations, the simulations provide a comprehensive picture of the unsaturated zone transport of ^{237}Np under ambient conditions, which is an important step toward building a defensible model of radionuclide migration.

1.1 Scope of Report

This report is divided into eight sections with the first section being this introduction and the eighth the conclusions. Section 2 describes the laboratory scale measurements of solubility, sorption, and diffusion for Neptunium which lead to the geochemical parameters used in the site scale radionuclide migration simulations. Section 3 provides an introduction to the important hydrologic processes which are considered in the flow and transport simulations. Section 4 describes the automatic process used in this study for integrating geologic data into our flow and transport models. The mathematical methods used in flow and transport calculation are described in

Section 5 and Section 6 provides the site scale hydrologic modeling results. These results cover flow models in two- and three-dimensions for which both equivalent continuum dual permeability formulations are considered. Section 7 covers the solute transport sensitivity studies for ^{237}Np. Here, the migration of ^{237}Np is compared to the migration of a conservative tracer with both two- and three-dimensional models. The sensitivity of ^{237}Np is evaluated with respect to infiltration rate, diffusion, sorptive behavior in zeolitic units, and thickness of zeolitic units below the potential repository. Both equivalent continuum and dual permeability formulations were used in these solute transport studies. The dual permeability simulations allowed for investigation of ^{237}Np migration in fractures and the physical and chemical processes that retard that movement. Through these eight sections, this report describes a comprehensive study leading to an improved understanding of the complex processes affecting the migration of radionuclides in unsaturated tuffs at Yucca Mountain.

DRAFT

2.0 Laboratory Scale Measurements for Neptunium

Performance assessment analyses have shown that ^{237}Np is one of the radionuclides of greatest concern for assessing the safety of the site (e.g. Andrews et al., 1993, Wilson et al., 1994). Since there is no obvious mitigating factor that will limit the release of ^{237}Np to the accessible environment (extremely large sorption coefficient, low solubility, etc.), it was determined that detailed laboratory scale chemical and transport studies were required to develop a comprehensive, credible model for ^{237}Np transport. The laboratory scale chemical data collected for ^{237}Np for the Yucca Mountain Project includes solubility/speciation studies (Nitsche et al., 1993, 1994), batch sorption (Triay et al., 1994a), column sorption data in crushed tuff columns (Triay et al., 1994b), rock beaker diffusion data (Triay et al., 1993, Triay et al., 1994c), and transport through solid rock columns with and without fractures (Ware and Triay, 1995).

This chapter summarizes the laboratory scale experiments and data analyses performed for ^{237}Np. The overall goal is to provide technical justification for the model assumptions and parameter values used in subsequent site scale transport model calculations. At the beginning of each section, we demonstrate through simple models or other arguments the importance of the data being discussed. Then, we summarize the experimental data collected to date, using it to justify the simplifications employed in the site scale modeling effort. Of course, there are many experimental considerations and mechanistic studies that must be explored to gain a comprehensive understanding of a chemical transport system. Refer to the individual references cited for these details, which are beyond the scope of the present study.

2.1 Solubility/Speciation Studies

Experimental studies of the solubility and speciation behavior of neptunium and other radionuclides in Yucca Mountain groundwaters have been published by Nitsche et al. (1993) and Nitsche et al. (1994). The solubility of neptunium is clearly important because the solubility at a given set of geochemical and thermodynamic conditions represents the maximum amount of ^{237}Np that can exist in the fluid phase at equilibrium. The data base of solubilities includes measurements at temperatures ranging from 25 to 90°C in fluids with pH values from 5.9 to 8.5. Experiments starting with an undersaturated solution and the solubility-controlling steady state solid in solution yielded equilibrium concentrations that ranged from 4×10^{-5} M to 6.4×10^{-3} M. In general, solubility decreases with increasing temperature and pH. Experiments from oversaturation generally agreed with these results. Thus ^{237}Np is in fact quite soluble in Yucca Mountain groundwater, regardless of the chemical conditions likely to be encountered.

Speciation studies are important to gain a more fundamental understanding of the chemical processes that might be involved in ^{237}Np transport. The oxidation state and the chemical form of

the dissolved species of ^{237}Np will control the extent of sorption onto the rock surface, and to a lesser extent, the diffusion coefficient (through size effects). At all experimental conditions studied, Nitsche et al. (1994) showed that Neptunium (V) was the oxidation state. Furthermore, they determined that the predominant species in solution were NpO_2^+ and negatively charged carbonate complexes such as $NpO_2(CO_3)^-$. The relative amounts of each ion in solution will affect the extent of sorption, all else being equal. Cations are expected to exhibit sorption on tuffs at the groundwater conditions of Yucca Mountain, whereas the carbonate species are likely to be conservative. Thus the measured sorption coefficient K_d should be a function of the chemical conditions through the chemical processes that give rise to a certain fraction of negatively and positively charged neptunyl ions in solution.

2.2 Sorption Studies

2.2.1 Motivation

The need for comprehensive laboratory scale sorption studies of ^{237}Np on Yucca Mountain tuffs is motivated by the importance of ^{237}Np in performance assessment analyses and the relatively small but non-zero sorption coefficient (K_d). Note that even the relatively "low" sorption coefficients measured thus far are large enough to significantly impact the predicted travel time of ^{237}Np in some regions of the unsaturated zone. For example, a first order calculation of the retardation factor R_f for ^{237}Np can be made from the following expression:

$$R_f = 1 + \frac{\rho_b K_d}{\phi S} \tag{2-1}$$

where ρ_b is the bulk rock density, ϕ is the porosity, and S is liquid saturation. Assuming parameter values for the zeolitized Calico Hills of $\rho_b = 2$ g/cc, $\phi = 0.29$, $S = 0.92$ (Loeven, 1993), and $K_d = 2.5$ cc/g (Triay et al., 1994a, this study), the retardation factor computed from Eqn. (2-1) is 20. Despite the obvious importance of sorption based on this calculation, the variability of the sorption coefficient as a function of mineralogy clearly indicates that a more robust understanding of the chemical controls on sorption was required to build confidence in the validity of site scale ^{237}Np transport models. This section summarizes the batch sorption experiments for ^{237}Np sorption on single minerals and the Yucca Mountain tuff for the purposes of characterizing sorption in the site scale model. For experimental details and discussion on the potential mechanisms of the sorption reactions, see Triay et al. (1994a).

2.2.2 K_d as a function of rock type

Numerous batch sorption measurements for ^{237}Np have been performed for the Yucca Mountain tuffs. For the purposes of compiling the sorption measurements, Triay et al. (1994a) classify the tuff samples as either vitric, devitrfied, or zeolitic, providing measurements of the mineral abundances (XRD analyses) and surface area (using the BET method). There is a clear dependence on the rock type (due to mineralogic differences), with measured K_d values in J-13 water at pH 7 on the order of 2.5 cc/g for the zeolitic tuffs. A range of K_d values were in fact measured (see Figure 2-1): for the 43 sorption measurements in J-13 water at pH 7 on zeolitic

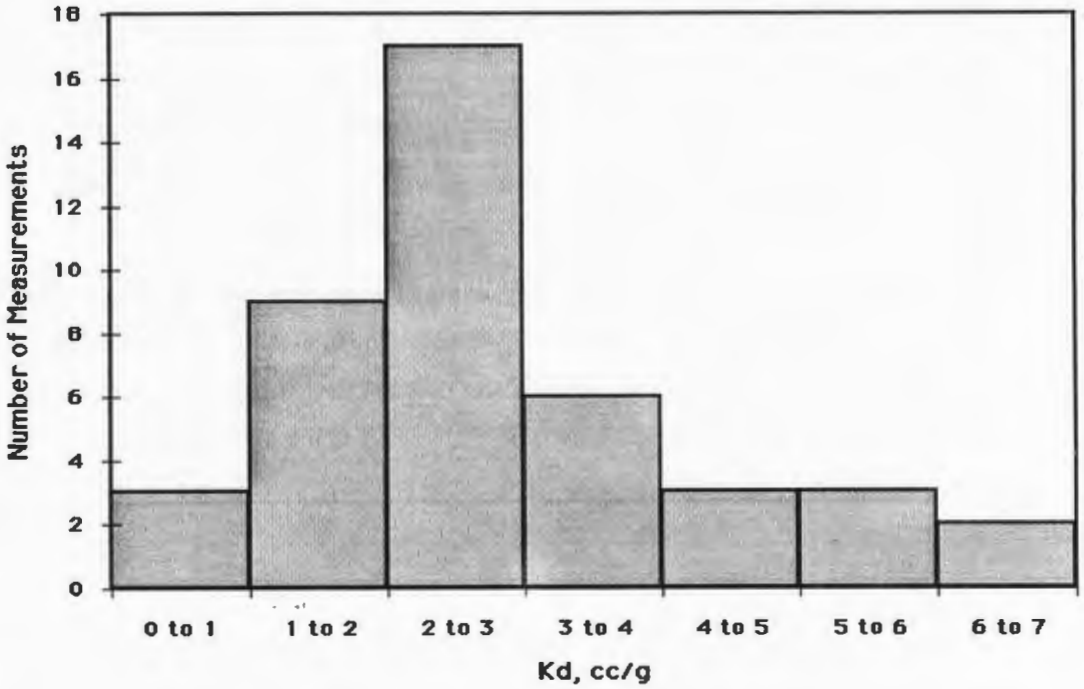

Figure 2-1. Histogram of sorption coefficients K_d for ^{237}Np on Zeolitic tuff samples from Yucca Mountain. Fluid: J-13 well water, pH 7.

tuff samples, the mean was 2.5 cc/g and the standard deviation was 1.4 cc/g.

Some vitric and devitrified samples also exhibit measurable sorption, but at much lower levels. Taking 0.2 cc/g as an typical value for vitric and devitrified tuffs, the retardation factor from Eqn. (2-1) is 3. Although this retardation factor would of course result in a travel time through these rock types a factor of 3 greater than a conservative solute, there is inherent uncertainty in the sorption values that would require much more experimental work before this retardation factor could be used with confidence in site scale models. In the interest of conservatism, we assume instead that ^{237}Np sorption is negligible on vitric and devitrified tuffs

for most of the simulations, and carry out a single analysis using 0.2 cc/g in the non-zeolitic units for comparison.

2.2.3 Effect of pH, ^{237}Np concentration, and kinetics on sorption

The primary mechanism for ^{237}Np sorption on Yucca Mountain tuffs has been shown to be ion-exchange (Tate et al.,1995). The chemistry of the groundwater solution typically impacts the sorption coefficients measured in batch and column sorption experiments. For ^{237}Np sorption on Yucca Mountain tuffs, the approach has been to attempt to bracket the sorption behavior using fluids of different ionic strengths within the range measured at Yucca Mountain (Meijer, 1992). For this purpose, fluid from wells J-13 and UE-25 p#1 were used. From the chemical analyses presented in Triay et al. (1994a), the ionic strengths of the fluids differ by about a factor of 5. In addition to ionic strength, the fluid pH is apt to affect sorption. Due to the evolution of CO_2 to the atmosphere during sampling and handling, on-site measurements of pH are typically about 7, whereas after transporting and handling, the pH of J-13 samples rises to about 8.5 and the pH of UE-25 p#1 water rises to about 9.

The impact of these parameters on ^{237}Np sorption was determined by Triay et al. (1994a). The higher ionic strength UE-25 p#1 fluid resulted in much lower sorption coefficients on zeolitized tuffs (and similarly low sorption on vitric and devitrified tuffs), even after eliminating the pH difference by applying a CO_2 atmosphere to the experiment sufficient to reduce the pH to 7. Values on the order of 0.2 cc/g or less were obtained in UE-25 p#1 fluid at pH 7 in the zeolitized units, making sorption negligible if the chemical conditions in the unsaturated zone resemble this fluid. Similarly low sorption coefficients were measured in the UE-25 p#1 fluid at pH 9. In addition to pH, the Ca^{2+} ion concentrations in the carbonate aquifer from which the UE-25 p#1 fluid came are quite high. Competetive effects of Ca^{2+} sorption may be the cause of low ^{237}Npsorption when UE-25 p#1 fluid, having a high Ca^{2+} concentration, is used.

The speciation effects discussed briefly in Section 2.1 also play a role in these K_d measurements. Chemical conditions that favor the formation of negatively charged carbonate complexes such as $NpO_2(CO_3)^-$ will result in lower sorption coefficients, all else being equal. Clearly this could be the case for the high pH and high carbonate sorption experiments.

Regarding the effect of pH, the sorption coefficient of ^{237}Np in J-13 water on zeolitic tuff decreased from about 2.5 cc/g to near zero when the pH was raised from 7 to 9 using a controlled CO_2 atmosphere (Triay et al., 1994a). Clearly, a source of uncertainty in the ^{237}Np site scale transport analysis presented below is the uncertainty of the pH values and chemical

composition of fluid in the zeolitic tuffs and how that impacts sorption. The beneficial effects of sorption in the zeolitic tuffs will be largely reduced if the pH of these waters is 8.5 to 9 rather than of order 7, or if high concentrations of Ca^{2+} result in competitive effects for available sorption sites.

Thus far, sorption data have been presented as sorption coefficient K_d, which can only be used in transport models if the sorption is linear in fluid concentration, rapid compared to transport times, and reversible. In Section 2.4.2 we discuss transport evidence that indeed the sorption is linear and reversible. Kinetics studies of ^{237}Np sorption on zeolitic tuffs indicates that the sorption reaction takes place within the first day of the experiment (Triay et al., 1994a). Clearly, this reaction is rapid compared to transport times within the zeolitic rocks at Yucca Mountain. The only exception would perhaps be rapid flow within fractures. However, under conditions of rapid transport in fractures, the ^{237}Np would not contact the zeolitic rock to any great degree, so the issue of kinetics is not important in this case either. For field scale transport scenarios in which the matrix rock is being contacted by ^{237}Np, kinetics effects should be negligible.

2.2.4 Single mineral sorption studies

To gain a more complete understanding of the mechanisms of ^{237}Np sorption than can be acquired on whole rock samples, sorption experiments on single minerals (clinoptilolite, hematite, and calcite) have also been performed. In addition to providing information on sorption mechanism, these measurements help to develop and strengthen correlations between sorption coefficient and mineralogy, so that a "K_d Map" of Yucca Mountain can be constructed from mineralogic measurements. This approach is obviously more cost effective than developing such a map from batch sorption measurements alone.

Existing data for ^{237}Np sorption on clinoptilolite suggests that it is probably the controlling mineral responsible for the observed sorption behavior on whole rock samples. The sorption coefficients measured on pure clinoptilolite agree closely with those of the clinoptilolite-rich tuff samples (Triay et al, 1994a). Furthermore, the kinetics of sorption onto clinoptilolite are rapid, like the sorption kinetics for the tuffs. Finally, the chemistry of the fluid (pH and ionic strength) influence the sorption coefficient similarly for clinoptilolite and the zeolitic tuffs. This correlation should come as no surprise, since the zeolitic tuffs typically consist of 50-75% clinoptilolite. Nonetheless, the tests on pure clinoptilolite establish that this mineral, rather than perhaps a trace mineral with extremely high sorptive capacity for ^{237}Np, controls sorption.

Iron oxides are one such set of minerals that could possibly exert a large influence on ^{237}Np sorption, as reported by Combes et al. (1992). Triay et al. (1994a) also measured large K_d values in pure hematite sorption experiments. However, whole rock samples containing trace amounts of hematite appear to sorb ^{237}Np no differently than rocks without hematite. Triay et al. (1994a) conclude that perhaps the sorption sites are passivated in the tuffs. Regardless of the reason, no enhanced sorption or correlation of K_d with the presence of iron oxides was found.

One other mineral that potentially has implications for the transport of ^{237}Np is calcite. Calcite coatings on fracture walls have the potential to provide delays in travel times for the very situations that the bulk rock sorption processes are minimal, namely transport in fractures. Sorption appears to be very strong onto calcite, but the K_d values for calcite varied by more than an order of magnitude depending on whether the calcite was wet-sieved or dry-sieved. Triay et al. (1994a) postulate that the difference is due to differences in the surface area depending on the preparation procedure, and conclude that it is difficult to obtain reliable K_d values from single mineral experiments. Consequently, ongoing transport experiments assessing the effect of calcite are being performed on fractures that contain calcite coatings.

2.3 Diffusion Studies

2.3.1 Motivation

Diffusion of ^{237}Np in Yucca Mountain tuffs is important for situations in which fluid flow paths of widely contrasting flow velocities co-exist in a porous medium. For example, if significant flow occurs within fractures, it is tempting to simply assume that the solute transport time is equal to the flow velocity within fractures divided by the flow path length. However, this approach ignores that solutes can readily travel by molecular diffusion alone into the surrounding rock matrix, where flow velocities are apt to be orders of magnitude lower. A wide body of evidence exists to suggest that matrix diffusion is an important transport mechanism in fractured media, both on a theoretical (Neretnicks, 1980, Robinson, 1994) and experimental basis (Maloszewski and Zuber, 1993, Reimus, 1995).

Idealized models can be employed to provide justification for including the effects of matrix diffusion in site scale transport simulations. Figure 2-2 shows the geometry of the model system used for this purpose. The geometry and flow system consists of equally spaced, parallel fractures, each of which transmits equal flow. Fluid in the rock matrix is stagnant. Transport in the fractures is governed by the one-dimensional axial dispersion equation with linear, equilibrium sorption on the fracture faces, while transport between the fracture and matrix is described by the one-dimensional diffusion equation:

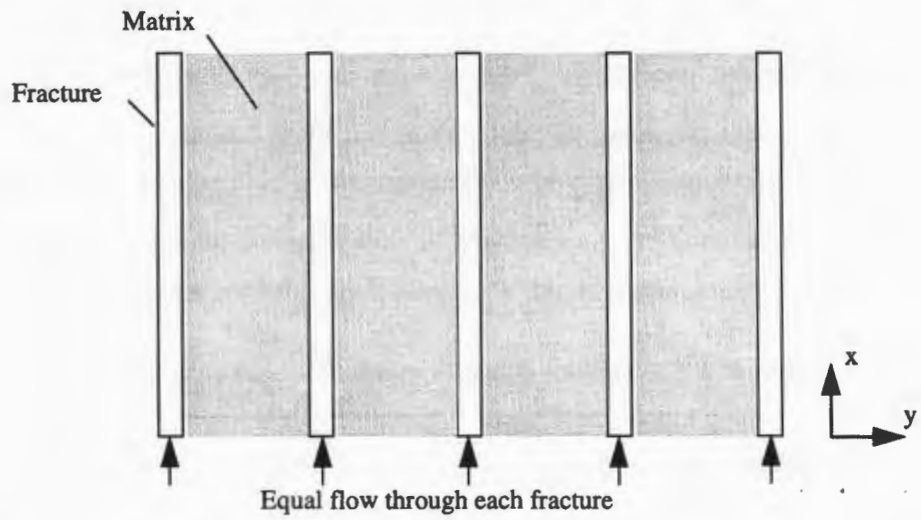

Figure 2-2.Model geometry for the matrix diffusion model.

$$R_{f,m}\frac{\partial C}{\partial t} = D_{AB}\frac{\partial^2 C}{\partial y^2} \tag{2-2}$$

where $R_{f,m}$ is the retardation coefficient for the matrix (from Eqn. (2-1)). The molecular diffusion coefficient D_{AB} is the product of the free diffusion coefficient of the solute in water and a tortuosity factor to account for the details of diffusion through a tortuous, fluid filled pore network. In this model, we treat D_{AB} as the fundamental transport parameter, recognizing that it is a property of both the solute and the medium.

Solutions to this transport problem depend on the nature of the boundary condition in the y-direction. A complex, semi-analytical solution is given by Tang et al. (1981) for the semi-infinite boundary condition $\frac{\partial C}{\partial y} = 0$ as $y \rightarrow \infty$. For the case of plug flow (no dispersion) in the fractures, Starr et al. (1985) show that the solution reduces to

$$\frac{C}{C_0} = erf\left[\frac{\phi\tau_f\sqrt{R_{f,m}D_{AB}}}{b\sqrt{t - R_f\tau_f}}\right] \tag{2-3}$$

DRAFT

for $t > R_f \tau_f$, and $C/C_0 = 0$ for $t \leq R_f \tau_f$. In Eqn. (2-3), b is the fracture aperture, τ_f is the fluid residence time, and $R_{f,m}$ is the matrix retardation factor, given by Eqn. (2-1). The semi-infinite boundary condition between fractures limits the validity of either of these solutions to situations in which the characteristic diffusion distance for the transport problem is small compared to the fracture spacing S. For the case in which this assumption is not valid, Robinson (1994) presents a numerical solution to this problem for the boundary condition $\frac{\partial C}{\partial y} = 0$ at $y = S/2$. The extent of matrix diffusion can be parameterized using the diffusion number $Di = (\phi\sqrt{R_{f,m} D_{AB}})/S$. A sensitivity analysis indicates that values of $Di > 0.1$ invalidate the assumptions of the Tang et al. solution, while for $Di < 0.1$, the solution is adequate. At much higher values of Di, diffusion into the matrix is so pervasive that the interference of solute concentration between the fractures is felt. In the extreme of very high Di, the system reverts to one-dimensional behavior, with the transport time given by the fracture transport time times the ratio of the total porosity to the fracture porosity.

Clearly, the only situation in which the transport time is equal to the fracture fluid residence time is for very low values of Di. Robinson (1994) showed that for reasonable parameter values for the saturated zone, transport reverts to the other extreme, namely that the solute transport as though the fractures do not even exist. For the vadose zone, a similar analysis can be performed. However, since there is considerable uncertainty on the nature of fracture flow, it is perhaps more informative to turn the question around to ask: what is the minimum fracture travel time that still allows sufficient time for radionuclides to diffuse into the surrounding matrix? For this calculation, the characteristic distance used in an order of magnitude analysis is the fracture aperture, rather than the fracture spacing. For a diffusion coefficient of 10^{-11} m^2/s and fracture aperture of 0.1 mm, the characteristic diffusion time is 1000 s.

The order of magnitude analysis just performed demonstrates that even for a relatively small molecular diffusion coefficient, there are physical transport processes mitigating the rapid transport of solutes through fractures. Therefore, accurate determination of the diffusion coefficient of ^{237}Np in tuff will, if they are large enough, allow us to justify an equivalent continuum model in which the matrix volumetric water content (ϕS) is used to compute transport times. Even if diffusion is insufficiently rapid for complete invasion of ^{237}Np into the matrix pore space, transport times will be much larger than would be computed from the

fracture flow velocity. Just as importantly, sorption coefficients measured on whole rock samples will apply if diffusion into the matrix is pervasive.

2.3.2 Diffusion Coefficient Measurements in Saturated Tuff

Diffusion coefficient measurements for ^{237}Np have been presented in Triay et al. (1993) and Triay et al. (1995a). Details of the experimental procedures are outlined in those reports. The apparatus used for these measurements is the so-called rock beaker, shown schematically in Figure 2-3. A void space of approximately 15 ml is created by coring a cylindrical void space

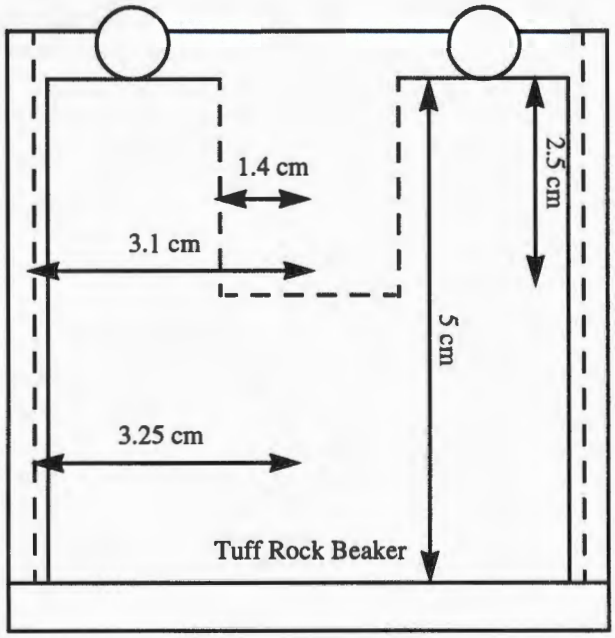

Not to Scale

Figure 2-3. Schematic of the rock beaker diffusion experimental apparatus.

inside the tuff specimen. The entire system is saturated with water, and the ^{237}Np solution is added to the contents of the beaker. The concentration decreases inside the beaker over time due to diffusion of solute into the pore space. This concentration-time behavior is modeled using the diffusion equation (the cylindrical coordinate version of Eqn. (2-2)) for various values of D_{AB}, from which the best fit is determined. Recently, the computer code FEHM has been used to perform the modeling, but the results of the simulations agree with analyses performed previously by Triay et al. (1993) using the TRACR3D code.

In the absence of sorption, the diffusion coefficient is determined directly by varying the single adjustable parameter D_{AB}. As shown in the discussion on sorption, the sorption coefficient is minimal on zeolitic tuff samples for pH values greater than about 8.5. Therefore, diffusion experiments under these conditions yield the diffusion coefficient directly. Figure 2-4 is an analysis of an experiment performed on a zeolitic tuff sample from well G1 in which both

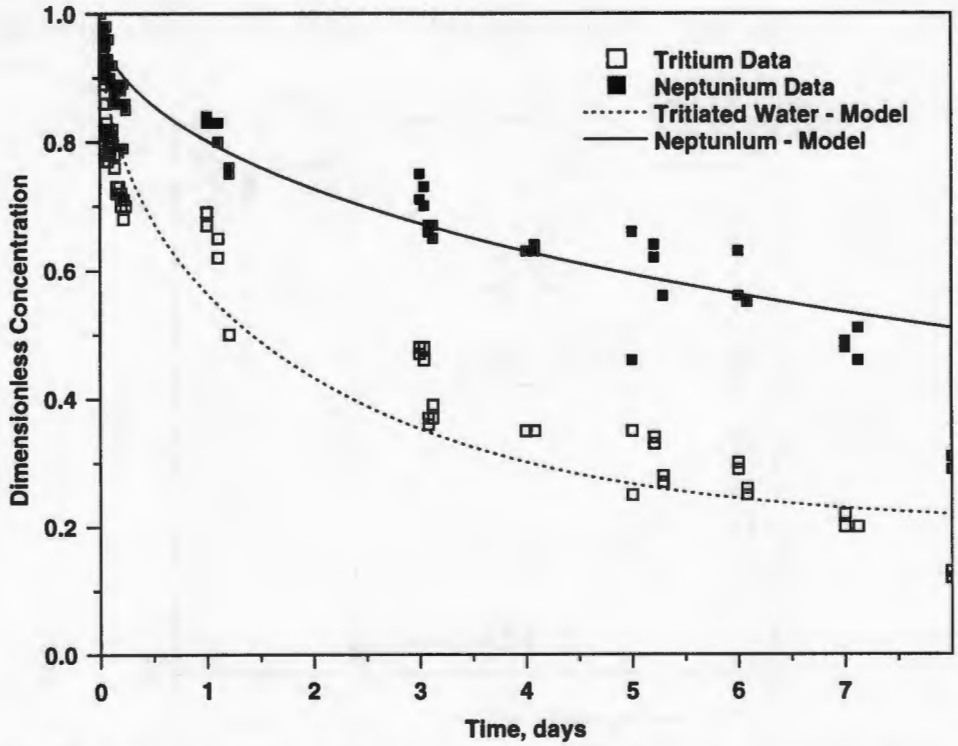

Figure 2-4. Rock beaker experimental results and model curves generated using FEHM. The best fit values for D_{AB} are 6 x 10^{-10} m^2/s for the tritiated water and 1 x 10^{-10} m^2/s for ^{237}Np. Reference: Triay et al. (1995a).

tritiated water (HTO) and ^{237}Np are introduced into the beaker. The resulting diffusion coefficients obtained are 6 x 10^{-10} m^2/s for HTO and 1 x 10^{-10} m^2/s for ^{237}Np. The tortuosity of the porous material reduces the diffusion coefficients by about an order of magnitude from their free-diffusion values. This result is to be expected for a tortuous pore space such as a tuff rock sample. The smaller diffusion coefficient for ^{237}Np is probably due to its larger size, which results in a smaller diffusion coefficient either in free water or in a porous medium.

One potential problem with using these diffusion coefficients in a matrix diffusion model is that coatings present on fracture walls could provide a barrier to diffusion that would not be

present in a rock beaker transport system. Two lines of evidence argue against this objection. First, not all natural fractures contain coatings. SEM photographs of fractures that do contain coatings show that they are in fact porous mineral assemblages, rather than the nonporous, impermeable barriers to transport that would be required to minimize interaction of solutes with the rock matrix. A more direct observation of the effect of fracture coatings is a recent experimental study using diffusion cell measurements by (Ines Triay, personal communication, 1995). In these tests, the reservoir containing the solution of ^{237}Np is in contact with a fracture surface that has significant secondary mineralization (a fracture coating). These tests show that diffusion into the tuff is not inhibited by the presence of the coating.

Experimental work is ongoing to construct the data base for diffusion of ^{237}Np in Yucca Mountain tuffs. However, the experiments are more difficult to perform than, say, batch sorption measurements, so there will always be a relatively small data base to work with. Nonetheless, the experiments suggest that appreciable diffusion within the matrix can occur in a relatively short time scale, and that the saturated diffusion coefficients to use in site scale models are of order 10^{-10} m^2/s. The selection of a value for unsaturated zone models is discussed further in the next section.

2.3.3 Diffusion Coefficient Measurements in Unsaturated Tuff

The experimental techniques for determining the diffusion coefficient of a solute in unsaturated media are relatively untried and present a more daunting experimental challenge than tests under saturated conditions. No such experiments have been performed for ^{237}Np or any other solute in the Yucca Mountain tuffs. In an investigation of the properties of gravel proposed as a backfill material, Conca and Wright (1990) developed and demonstrated a technique using their Unsaturated Flow Apparatus (UFA) for measuring flow and transport properties under unsaturated conditions. They showed that as volumetric water content decreased to low values, the diffusion coefficient decreased to extremely small values (orders of magnitude smaller), presumably due to the precipitous decline in the fluid cross sectional area available for diffusion as the largest pores emptied.

To assess the impact of unsaturated conditions in the matrix on diffusion into the matrix rock, we must consider the hydrologic conditions that are likely to exist locally in a region where fracture flow is important. Current conceptual models such as the equivalent continuum model formulation suggest that fracture flow will be minimal until fluid saturations in the matrix reach very high values (close to 1). This is a result of the widely different capillary pressure relations for the two media: the saturation in the fractures will be low and fracture flow rates will be minimal unless the saturation in the matrix is high. Of course, the equivalent

continuum model requires capillary pressure equilibrium between the media that may not exist in a medium containing fractures. Dual permeability conceptual models do allow for fracture flow without high saturations in the matrix, but in these cases there is an advective driving force for solute movement into the matrix that is likely to outweigh molecular diffusion as a mechanism for transporting solute into the matrix. Dual permeability models will reflect the relative importance of the two processes (advective versus diffusive transport). In either case, using a diffusion coefficient measured at saturated conditions is a reasonable assumption.

Finally, either the equivalent continuum or dual permeability models are idealizations that represent average property values such as fluid saturation. If fracture flow does exist, perhaps due to a temporary increase in infiltration rate, then in the matrix immediately adjacent to the fluid in the fracture, saturation will increase with time as fluid is imbibed by capillary forces. This saturation will approach unity (absent any trapped air in the rock) locally near the flowing fracture fluid and spread into the pore space gradually over time. Thus it is likely that for hydrologic conditions that could give rise to rapid fracture transit times, the solute will be diffusing into a matrix that is locally saturated, even if averaged models imply less than complete saturation. Therefore, the diffusion coefficient measured at saturated conditions is a valid *upper* bound in to use in site scale unsaturated zone models.

The above discussion assumes that our current conceptual models of the hydrologic conditions are valid. The work of Glass and associates (Nicholl et al., 1994, Tidwell et al., 1995, Glass and Nicholl, 1995) illustrates that these models are in a primitive stage of development, and that certain important physical processes and mechanisms may not be included. This is a source of conceptual model uncertainty that is difficult to quantify. The best we can do is point out that if the conceptual model is adequate, then molecular diffusion should proceed through matrix fluid that is locally saturated, allowing measured diffusion coefficients to be used without correction for unsaturated conditions. However, the uncertainty in the conceptual model dictates that a sensitivity analysis be performed to assess the performance for lower values of the diffusion coefficient. The site scale model simulations of the present study treat the diffusion coefficient as adjustable with a range of values spanning two orders of magnitude, starting with saturated value of 10^{-10} m^2/s determined in the previous section.

2.3.4 Coupling of Sorption and Diffusion

Rock beaker diffusion experiments in zeolitic tuff samples under conditions at which sorption occurs have also been performed. In these tests, ^{237}Np simultaneously diffuses and sorbs to the rock, making the interpretation more complicated. Figure 2-5 shows the concentration-time history of HTO and ^{237}Np in a typical experiment. In contrast to the

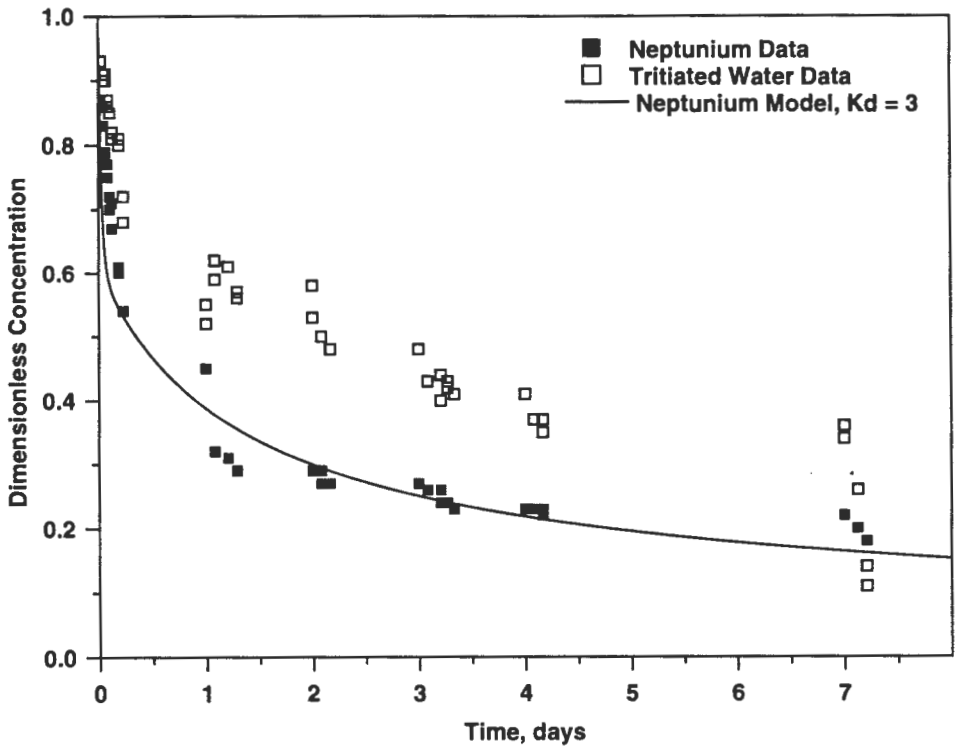

Figure 2-5. Rock beaker experimental results in a zeolitic rock sample. ^{237}Np undergoes diffusion and sorption, so that its uptake into the rock is faster than that of tritiated water. The opposite is true in the absence of sorption (Figure 2-4). Reference: Triay et al. (1995a).

nonsorbing diffusion experiment, the ^{237}Np uptake into the tuff is more rapid than that of tritiated water, indicating that sorption creates an additional driving force for ^{237}Np transport into the rock. Thus, the results qualitatively agree with intuition.

To provide quantitative backup for this argument, we assume that the tritiated water provides an estimate of the diffusion coefficient of ^{237}Np after correcting for the size effect difference in the diffusion coefficient observed in the experiment without sorption. From such an analysis we obtain a diffusion coefficient for ^{237}Np of 2×10^{-10} m^2/s. Then, we vary the sorption coefficient K_d to obtain a match to the ^{237}Np data. The fit in Figure 2-5 shows that a K_d of about 3 cc/g is required to match the ^{237}Np data. Although this model of the experiment is nonunique, the value agrees well with the average value of K_d from the batch sorption measurements, implying that the transport system of coupled sorption and diffusion is readily understood. Since the laboratory scale results are well understood, the next step is to increase the scale of the experiments substantially. Until this field testing component of the study is

performed, we must assume that the parameter values determined in laboratory tests can be used in site scale simulations.

2.4 Column Transport Studies

2.4.1 Motivation

Sorption coefficients are typically measured in batch systems due to the cost effectiveness of the technique. However, there remains an uncertainty regarding whether this sorption coefficient can be used along with Eqn. (2-1) or a more complex transport model to predict the travel time of the solute in a flowing system. Therefore, column transport studies are typically performed to verify the batch sorption results. A pulse or step change in tracer concentration is input to the column after having established steady state fluid flow. The measured concentration versus time response at the outlet can then be simulated using the one dimensional convective-dispersion equation with sorption:

$$\frac{\partial C}{\partial t} + \frac{\partial S}{\partial t} = D_e \frac{\partial^2 C}{\partial x^2} - u \frac{\partial C}{\partial x} \tag{2-4}$$

where S is the surface concentration of solute, D_e is the dispersion coefficient, and u is the fluid velocity. When sorption is rapid compared to transport through the column, a sorption isotherm relating S and C can be used to eliminate the surface concentration term from Eqn. (2-4). Linear or nonlinear isotherms can be used for this purpose. Assuming a linear sorption isotherm, Eqn. (2-4) reduces to:

$$R_f \frac{\partial C}{\partial t} = D_e \frac{\partial^2 C}{\partial x^2} - u \frac{\partial C}{\partial x} \tag{2-5}$$

where R_f is the retardation factor defined in Eqn. (2-1). When kinetics effects are present, more complex models that include the sorption reaction must be used.

Thus the process of determining the validity of batch sorption measurements in a transport system is fairly simple in a one-dimensional flow system. The situation for ^{237}Np is somewhat more complex due to the effect of mineralogy and fluid chemistry on the batch sorption behavior. Thus the goal of the column transport experimental program is to show that over the range of chemical and mineralogic conditions tested in the batch sorption experiments, the sorption characteristics of ^{237}Np are reproduced in an advective transport system. A similar

result has already been demonstrated in Section 2.3 for a diffusive system (the rock beaker experimental system).

2.4.2 Crushed Rock Column Transport Experiments

A series of column transport experiments using crushed rock have been carried out and reported by Triay et al. (1994b). In a typical experiment, crushed tuff of a known size distribution (75 to 500 μm obtained by sieving) was packed in a column of dimensions of the order of 1 m in length and 6 mm in diameter. This large aspect ratio ensures that the one dimensional transport equation will be valid for the system. After establishing a steady state flow and passing several pore volumes of the desired solution (J-13 or UE25 p#1 fluid as in the batch sorption experiments) through the column to obtain a chemically stable system, a pulse containing HTO and ^{237}Np was injected into the system and the concentration-time response of the flowing system was determined in the effluent fluid.

In a preliminary analysis of the data, Triay et al. (1994b) took the time at which 50% of each tracer exited the system and used the relation $R_f = \tau_{Np}/\tau_{HTO}$ to estimate the retardation factor and Eqn. (2-1) to determine K_d. In this expression, τ_{Np} and τ_{HTO} are the arrival times for ^{237}Np and HTO, respectively. Using this approach, they obtained good agreement between the K_d values determined from the column and batch sorption methods. Specifically, the only significant retardation due to sorption occurred on zeolitic tuffs using J-13 water at pH 7. A slight amount of sorption (but essentially no sorption for the purposes of site scale modeling) occurred on devitrified and vitric tuffs, and using UE-25 p#1 fluid resulted in similarly low sorption coefficients even on the zeolitic tuffs. These results agreed with the batch sorption tests of Triay et al. (1994a) discussed in Section 2.2.

Although the analysis performed was sufficient to fulfill the primary goal of the column transport tests, a more complete numerical analysis was carried out to examine the issues of linearity and possible kinetics effects more closely. For the ^{237}Np column sorption experiments, the computer code SORBEQ has been used on a select number of column transport tests. This code includes linear or nonlinear sorption isotherm models, and ignores kinetic effects (equilibrium sorption). A nonlinear regression of the breakthrough curve is performed to test the validity of the model and to obtain best fit model parameters. Figure 2-6 shows the best fits to the HTO and ^{237}Np breakthrough curves for a test using zeolitic tuff and J-13 water at pH 7 (conditions under which significant sorption of ^{237}Np occurs). The HTO curve fit is used to obtain the hydrodynamic parameters of the column, the breakthrough volume of a conservative

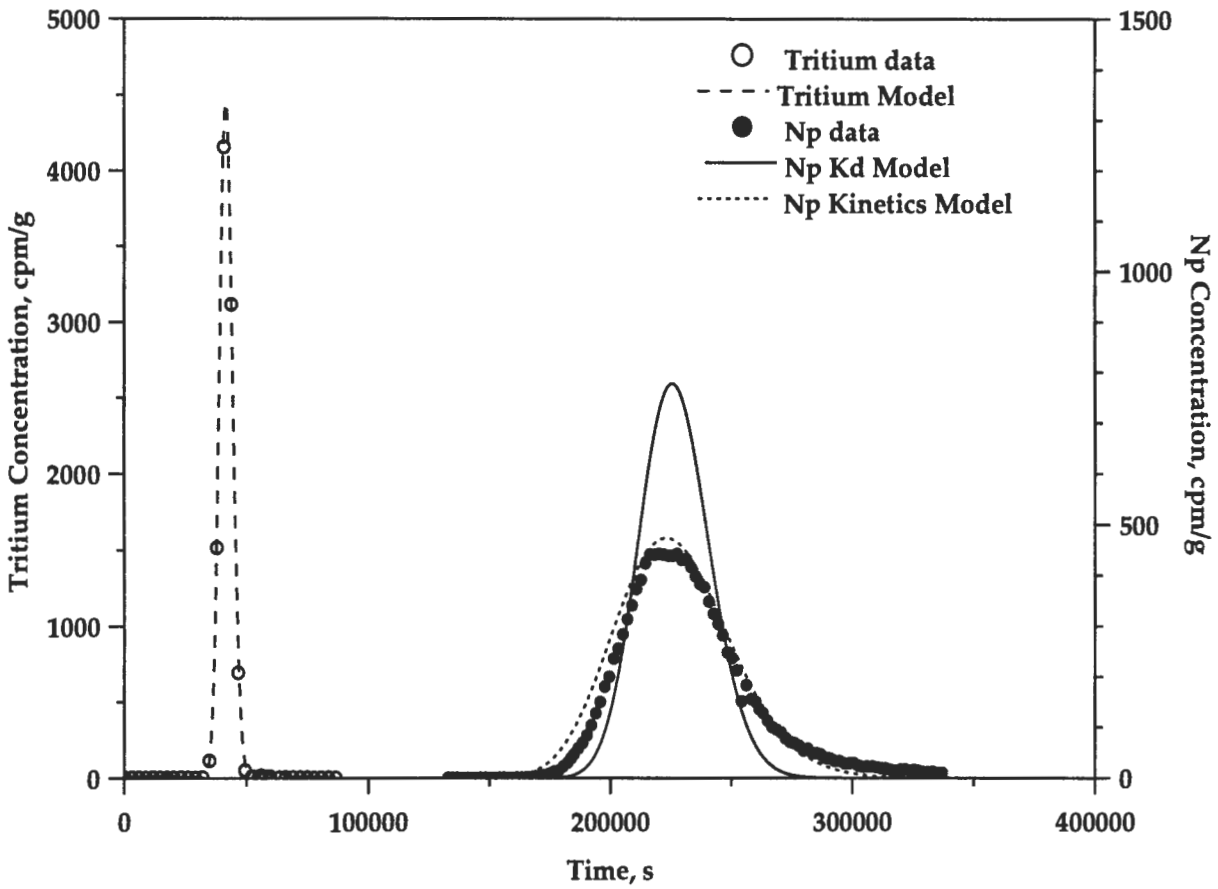

Figure 2-6. Breakthrough curves for tritiated water and ^{237}Np from column transport experiments. Rock type: zeolitic; Fluid: J-13 fluid at pH 7. Reference: Triay et al., 1994b.

solute and the Peclet number $Pe = uL/D_e$ which characterizes the extent of axial dispersion. Holding these parameters constant, the best fit to the ^{237}Np data is then obtained by varying the sorption parameters. Although the characteristic breakthrough time of ^{237}Np can be matched, the shape of the breakthrough curve cannot be reproduced either with the single-parameter linear model or the more complex multi-parameter nonlinear sorption isotherm models. The data exhibit a greater apparent dispersion than any of the models, even though there is no reason to expect that the hydrodynamic dispersion coefficient should be different for the two tracers.

Valocchi (1985) demonstrated that the sort of behavior exhibited by ^{237}Np in Figure 2-6 is consistent with a kinetic model of sorption. As a sorbing species deviates from equilibrium behavior, the breakthrough time is reproduced but the solute exhibits a greater apparent dispersion. The simple corrections to the dispersion coefficient derived by Valocchi (1985) and

Goltz and Roberts (1987) to account for kinetics effects cannot be applied to these data because the Peclet number for the columns is too small for the relations to be valid. Alternatively, we used the FEHM reactive transport model to examine the kinetics effects. In this model, two species are simulated, the sorbing, aqueous tracer and a sorbed species. A linear kinetic model was assumed to represent the term $\frac{\partial S}{\partial t}$ in Eqn. (2-4). The ratio of the forward and reverse rate constants is the equilibrium constant K_d, which we assumed to be equal to the value obtained from the linear isotherm best fit depicted in Figure 2-6. Figure 2-6 shows the model results compared to the data for a value of the Damkohler number $Da = k_r \tau_{fl}$ of 200, where k_r is the rate constant of the reverse reaction in the sorption model and τ_{fl} is the fluid residence time. A much better fit to the data than the equilibrium sorption model is achieved for $Da = 200$, corresponding to a value of k_r of 2 x 10^{-3} s^{-1}. For this rate constant, a characteristic reaction time is of order 8 minutes, which is obviously too rapid to be observed in the kinetics studies for ^{237}Np, which were designed to examine kinetics that might occur at the longer time scales of interest for field scale predictions (on the order of days).

The analysis just presented shows that a quantitative understanding of the transport of ^{237}Np in crushed rock columns has been achieved. This understanding provides supporting evidence that the sorption coefficients determined in the batch experiments can be used in site scale models. The kinetics effects found in the experimental data, though important at the time and spatial scales of the column tests, should be irrelevant at the larger time scales of the field. Thus it is consistent to use a linear, equilibrium model to characterize ^{237}Np sorption in the site scale modeling of the present study.

2.4.3 Fractured Rock Column Transport Experiment

Recent experimental results have been obtained from transport tests through fracture rock columns. These tests bear directly on the transport of ^{237}Np through fractured rock. The authors are grateful to Ines Triay, LANL, for allowing us to present these newly acquired, unpublished data, along with her group's written description of the results that we present below. In these experiments, five natural rock fractures from core samples from Yucca Mountain were encapsulated for column experiments. The rock columns were saturated with sodium bicarbonate/carbonate waters (similar to groundwaters from the wells J-13 and UE-25 p#1), a flow rate of 0.5 ml/hr was established through the columns, and the columns were injected with radionuclide solutions. The solution eluted from the columns, after injection, was collected as a function of time and analyzed for determination of the amount of radionuclide in each sample.

We present the results of the elution of Tc-95m, H-3, and ^{237}Np in J-13 water solutions, flowing at 0.5 ml/hr, through a naturally fractured core from the USW G-4 at a depth of 2,981 ft. This core is from the Tram member of the Crater Flat Tuff Formation. It was concluded that this core contained a natural fracture due to the appearance of secondary minerals (hollandite and romanechite) coating the fracture walls. The length of this column is 6.04 cm with a diameter of 5.22 cm. The aperture of the fracture has yet to be determined. Tritiated water (H-3) and technetium (Tc-95m) are not expected to sorb to Yucca Mountain tuffs and were injected to determine the flow and transport properties of the fractured system.

The results presented in Figure 2-7 indicate that:

- diffusion from the fracture into the matrix seems to take place (given that recovery of the tritium injected was only 80% as compared to 90% Tc-95m recovery). The trend observed in Figure 2-7 seems to agree with the smaller diffusion coefficients estimated for Tc-95m than for tritiated water (measured in tuff).
- ^{237}Np seems to be significantly retarded even in this fracture-flow system. The recovery of ^{237}Np is less than 10% and the first appearance of ^{237}Np is retarded with respect to ^{3}H and Tc-95m. This observation seems to indicate that ^{237}Np retardation in this experiment could be due to both diffusion into the matrix and sorption onto the minerals lining the fracture walls.

As an initial attempt to simulate these results, we assume the model of Tang et al. (1981) in which dispersion is governed by one-dimensional axial dispersion in the fracture, and molecular diffusion occurs into an infinite medium (the rock matrix). Linear reversible sorption is assumed, with different retardation factors for the fracture surface and rock matrix. All relevant parameter values for the model are not yet known, so typical values will be assumed for this analysis. Assumed parameter values are:

- fracture volume = 1 ml
- fracture aperture = 1 ml/(6.04 cmx5.22 cm) =.032 cm = 0.32 mm
- dispersivity = 0.3 cm (Peclet number = L/dispersivity = 6.04/.3 = 20)
- matrix porosity = 0.1

The Tc-95m and H-3 simulations in Figure 2-7 were obtained assuming a difference in the diffusion coefficient of a factor of five. This difference gives rise to the correct trend in the breakthrough curve. The actual values used to obtain these results were 10^{-9} m^2/s for H-3 and 2×10^{-10} m^2/s for Tc. These numbers seem somewhat high for diffusion in a tuff matrix based on rock beaker diffusion experimental results (see Section 2.3.2), but, given the uncertainties in the analysis, the results are consistent with a matrix diffusion mechanism.

For ^{237}Np, two simulations were performed: the first assumed sorption only on the matrix rock, while the second assumed sorption on the fracture wall and matrix rock. In all cases, a diffusion coefficient of 10^{-9} m^2/s was assumed. Either of these models can explain the observed

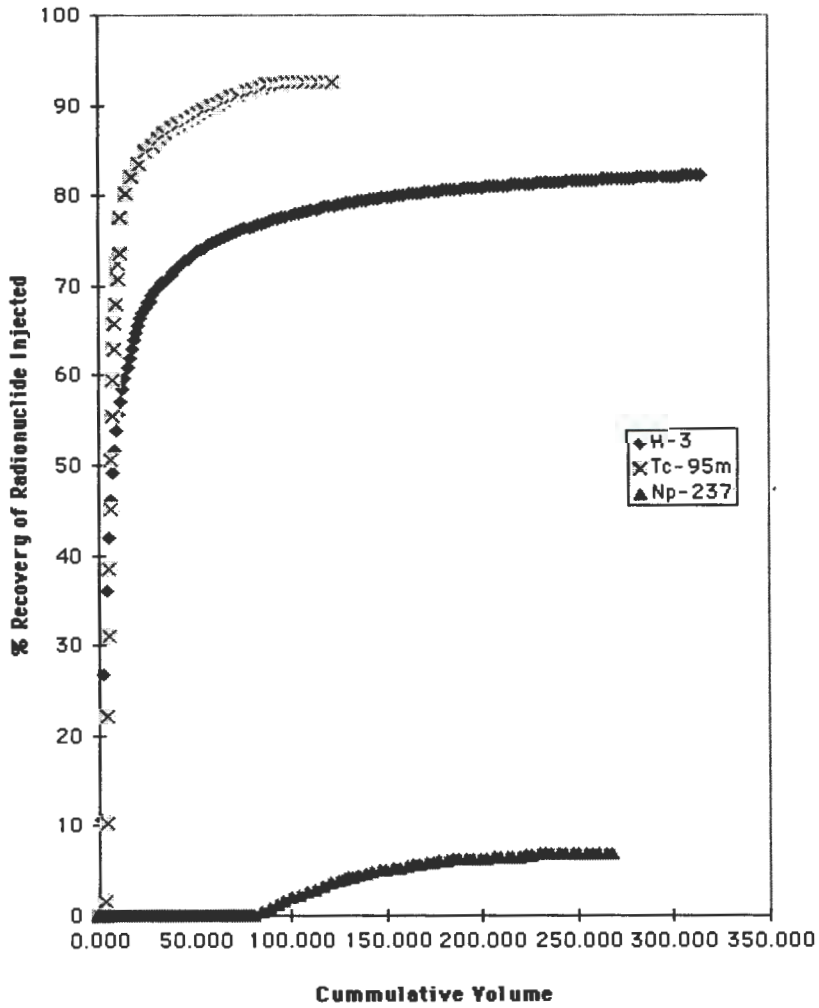

Figure 2-7. Breakthrough Curve Results of the fractured rock column transport experiment.

elution curve for ^{237}Np (at least to the accuracy of this analysis), as shown in Figure 2-7. The retardation factors used for the simulations are:

- Matrix sorption only: matrix $R_f = 1000$ ($K_d = 50$ cc/g)
- Fracture and matrix sorption: matrix $R_f = 500$, fracture $R_f = 70$.

Although there is considerable uncertainty in the parameter values and the validity of the one-dimensional analysis, it seems clear that the data are consistent with very large K_d values, at least compared to the typical value of 2.5 for ^{237}Np on zeolitic tuff. It will be very difficult or impossible to distinguish between the fracture sorption and combined fracture and matrix sorption models in these experiments because the ^{237}Np does not diffuse very far into the matrix under these conditions. Therefore, if a highly sorptive fracture lining mineral is present

even a short distance into the rock matrix, the sorption coefficient in this test will resemble that of the mineral rather than the bulk rock values measured in previous crushed rock work.

The surface of this fracture contained oxide minerals that have not specifically been tested in single-mineral studies. Other single mineral studies (Section 2.2.4) showed that iron oxides are a very strong sorbers of ^{237}Np. It is possible that minerals present in trace quantities in the bulk rock that appear to contribute insignificantly to sorption may be quite effective at retarding ^{237}Np transport when concentrated on fracture surfaces. Thus, one sensitivity study that will be performed is to assume sorption onto fracture surfaces containing sorptive minerals. The dual permeability model will be used for this analysis. Assuming that the analysis just presented is typical of ^{237}Np sorption onto fracture surfaces, a retardation factor of 70 will be used.

2.4.4 Other Planned Column Transport Experiments

The ^{237}Np transport experimental program is ongoing, with other types of transport tests being performed to investigate further the relevant processes. Solid rock transport tests are being carried out to determine if sorption coefficients determined after crushing are different than values in intact rock. Since thorough studies have already been performed on the effect of crushing on sorption (Rogers and Chipera, 1994), significant differences are not expected. However, transport tests on intact rock will have a lower porosity, and thus somewhat different transport conditions even if the sorption coefficient is the same. Unsaturated column experiments are also planned for ^{237}Np to ascertain whether unsaturated conditions affect sorption behavior. A methodology is also being developed using the UFA to investigate the transport of sorbing solutes under partial saturation. In addition, the transport tests in fractured cores discussed in the previous section will be used to determine if solute traveling in a fracture contacts the rock where it can be retained by sorption. Finally, fractures containing mineral coatings such as calcite and iron oxides will be tested to determine if sorption on calcite in fractures can be demonstrated.

All of these experiments will provide added confidence that we understand the relevant transport processes for ^{237}Np and other radionuclides. However, the experiments and analyses have not yet been performed, and thus cannot be included for this report.

3.0 Hydrologic Considerations

The hydrologic processes and the hydrologic properties of the medium through which the radionuclides may travel significantly affect the transport behavior. Some of the most important processes and properties which affect transport are discussed in the sections below, including:

- the infiltration rate and distribution in both space and time;
- the location (delineation) of and contrasting hydrologic properties of stratigraphic bedding;
- fracture properties in the various units, including the role of faults on the hydrologic system;
- evidence from environmental isotopes such as ^{36}Cl and ^{14}C; and
- the chemical composition within beds, which controls the reactivity of the immobile matrix material with radionuclides.

3.1 Infiltration

The infiltration rate ultimately governs the water flux through the unsaturated zone at Yucca Mountain. This percolating water is a potential vehicle for transport of radionuclides from a potential repository to the accessible environment. Further as the flux of infiltrating water increases, saturations of the rock units increase. As the rock saturations increase, the potential for movement of water in fractures increases. Thus, the values and distributions of infiltration are an extremely important boundary condition for flow and transport models of Yucca Mountain's unsaturated zone which in turn will either be coupled with or provide a boundary condition for models of flow and transport of the saturated zone.

A recent three-dimensional site scale hydrologic model of the unsaturated zone at Yucca Mountain (Wittwer et al., 1995) uses either an infiltration rate of 0.1 mm/y distributed uniformly over the entire surface, or a nonuniformly distributed infiltration rate with an areal average of about 0.1 mm/y (higher infiltration rates near faults, lower elsewhere). Although recent hydrologic investigations have used values of this magnitude, a literature review provided by Hudson and Flint (1995) indicates that infiltration rates may be substantially higher over much of the surface of the region of interest. Figures 23 and 30 in Wittwer et al. (1995) appear to show that, for a 0.1 mm/y uniformly distributed infiltration rate, matrix saturations rarely reach the 0.98 threshold at which point, in their model formulation, fracture flow initiates. We find similar results in our simulations with that infiltration rate (Section 6.2). However, in light of the infiltration rates estimated by Hudson and Flint (1995), Hevesi and Flint (1995), Czarnecki (1984), and Fabryka-Martin et al. (1995), greater infiltration rates must be considered to assess water flow pathways to and radionuclide pathways away from the potential repository.

3.2 Delineation and Importance of Contrasting Permeabilities in Hydrostratigraphic Units

The permeability of the media through which the water moves governs the flux of water and hence its capability to transport solutes. In the unsaturated zone, the relative permeabilities of the fracture and matrix are dependent upon the saturations of those media. The interrelationship is described mathematically in Section 5.0. The relative permeabilities are directly dependent upon the infiltration rate because with more moisture available, the matrix saturations increase. As they increase, the capillary suction in the matrix decreases, reducing the ability of the matrix to pull water out of fractures. Hence, as infiltration increases, the system moves from one dominated by matrix properties to one that is influenced by fracture properties. Property characteristics of the fractures and matrix are incorporated into the flow and transport model, which computes spatial relative permeabilities based on those properties and the saturations.

The stratigraphic beds in the unsaturated zone at Yucca Mountain exhibit sharply contrasting characteristics in hydrologic properties. Based on the conceptual model developed by Montazar and Wilson (1984), the stratigraphy of the hydrogeologic units are described by alternating zones of densely welded tuff and zones of nonwelded to partially welded tuffs and bedded tuffs. The four major hydrostratigraphic zones include, from the surface to the water table, the Tiva Canyon welded tuff unit (TCw), the Paintbrush nonwelded tuff unit (PTn), the Topopah Springs welded tuff unit (TSw), and the Calico Hills nonwelded tuff unit (CHn).

After Wittwer et al. (1995) and new geologic interpreation of units below the potential repository (Vaniman, personal communications, 1995), each of these major units is divided into 3, 3, 6, and 7 subunits, respectively, to characterize interunit property differences. The welded Tiva Canyon and Topopah Springs units are characterized by low porosities (10-15%), low matrix permeabilities ($2\text{-}4 \times 10^{-18}$ m^2) (Montazar and Wilson, 1984), and high fracture densities (8-40 fractures per cubic meter) (Scott et al., 1983). In contrast, the nonwelded Paintbrush tuff units have porosities ranging from 25 to 50% and matrix permeabilities between 1×10^{-13} and 6×10^{-15} m^2 (Montazar and Wilson, 1984; Flint and Flint, 1990). Scott et al. (1983) found the fracture densities in these units to be on the order of one per cubic meter.

The Calico Hills unit is generally referred to as a nonwelded unit. However, sharp contrasts in matrix permeability exist within the subunits and can be differentiated by whether the subunit is zeolitic or not (Loeven, 1993). Loeven showed that the matrix permeabilities of zeolitic units of the Calico Hills beds were on the order of $7 \times 10^{-18} m^2$ and that the nonzeolitic unit permeabilities were on the order of $4 \times 10^{-16} m^2$. Wittwer et al. (1995) used markedly greater values for the zeolitic and nonzeolitic units of the Calico Hills. Although they report a range from $7 \times 10^{-17} m^2$ to $5 \times 10^{-19} m^2$ for

the zeolitic unit permeabilities, they use $1x10^{-16}m^2$. Likewise, they report a range from $2x10^{-15}m^2$ to $1x10^{-18}m^2$ for the matrix permeabilities of the nonzeolitic units, yet they use a value of $2x10^{-13}m^2$. The porosities reported by Loeven (1993) match those in Wittwer et al. (1995), ranging from 8 to 48% in the nonzeolitic units and 14 to 36% in the zeolitized units.

The unsaturated relative permeability of the matrix material in each of these units is a function of the intrinsic permeability and the saturation. In the mathematical methods section of this report (Section 5.0), a detailed description of the characteristic curve relationship of van Genuchten (1980) used in the present study is presented as it is applied in the flow and transport models. Table 6-2 presents the intrinsic permeabilities, porosities, and van Genuchten parameters used to compute relative permeabilities for each of the subunits characterized in this study.

In two- and three-dimensional model formulations, accurate delineation of the interfaces between these beds of sharply contrasting hydrologic parameters is necessary for simulating the flow paths of percolating water. The permeability contrasts can cause a capillary or Richard's barrier which leads to lateral diversion of vertically infiltrating water at an interface between units of contrasting permeability. Similarly, vertically percolating water in a high permeability unit can be laterally diverted upon encountering a unit of much lower permeability which is unable to conduct the entire flux. In contrast, one-dimensional simulations are unable to represent the multi-dimensional flow component associated with dipping beds. All water entering the system in such simulations must flow through all units. The data and automatic methodology used to construct two- and three-dimensional numerical models which capture the stratigraphy are described in Section 4.0.

3.3 Importance of Fractures and Faults

Fractures are important in assessment of flow and transport because they represent potential direct pathways for fluid and solutes. These have been regarded as significant for conducting percolating water from the surface to or around the potential repository and for conducting radionuclides from the repository to the saturated zone. Of greatest concern is the high fracture density reported for the welded tuffs (Montazar and Wilson, 1984). In simulation studies, fracture effects are incorporated into flow and transport models with either the equivalent continuum approximation of Klaveter and Peters (1986) or the dual permeability method. Both of these methods attempt to incorporate the physical flow processes associated with fractured material. The basic premise is that the matrix material has to reach a certain saturation before fractures will flow. The reason for this is that until saturated, a negative potential (matrix suction) exists in the matrix and serves to pull water out of fractures and into the matrix material. The equivalent continuum method is based on an assumption of equal capillary pressures in the matrix and fractures. Once a

"threshold" saturation is achieved in the matrix, flow in the fractures is initiated. This approximation is achieved by combining the relative permeability curves for the fracture material with the matrix material to create a single curve for the equivalent continuum which represents matrix behavior at low saturations and fracture behavior at high saturations.

With the dual permeability model formulation, the fractures are considered explicitly as one continuum while the matrix is considered as another. The two are combined through coupling terms. As related to solute transport, the equivalent continuum approximation inherently assumes full diffusion between the fractures and the matrix. With dual permeability, it is possible to investigate cases in which diffusion between the fractures and matrix material is limited. With full diffusion, a significant physical retarding mechanism exists which reduces the travel time of solutes even in systems exhibiting fracture flow. These methods are compared in Section 7.4.3, in which a sensitivity analysis to diffusion coefficient and method of simulation is performed. The condition under which such an analysis is important is high infiltration, which leads to high matrix saturation in the welded tuff, and fracture flow.

Although fractures have been identified throughout the welded tuff units of Yucca Mountain, their properties and densities are of particular interest in the vicinity of faults. The effect of fault zones on the distribution of flow within Yucca Mountain has been discussed by Wang and Narisimhan (1987), Rockhold et al. (1990), Tsang et al. (1993), and Wittwer et al. (1995). Although fault properties have not yet been explicitly characterized for Yucca mountain, Wittwer et al. (1995) examined the extreme cases which included either very high or very low matrix permeabilities in fault zones. They also examined the flow field arising from elevated infiltration rates over the fault zones for an otherwise zero net uniform infiltration distribution. Their results show that the relatively concentrated infiltration flux is dispersed laterally as well as vertically. Hudson and Flint (1995) have also suggested that due to dense fracture distributions near faults, elevated infiltration may occur in those regions. The increase has not been determined yet, thus indicating the need for improved property characterization and process measurement in those regions.

3.4 Evidence from isotopic tracers

Isotopic measurements of soil, tuff, and water samples have been collected to help quantify the amount of percolation from precipitation and the flow paths into the unsaturated zone at Yucca Mountain (Liu et al., 1995; Fabryka-Martin et al., 1995; Yang, 1994). Chlorine-36 and carbon-14, produced by cosmic ray secondaries interacting with atoms in the atmosphere, have half lives of 301,000 and 5,730 years, respectively. They also occur, along with tritium (half life of 12.2 years), at concentrations above natural levels as a result of global fallout from nuclear weapons tests

primarily between 1952 and 1963 (Bentley et al. 1986; Broecker et al., 1980). Based on expected concentrations at the time of infiltration and known decay rates, the isotopes are being used as natural tracers for estimating apparent travel times from the surface where infiltration occurs to the point of sample collection. This approach potentially can reduce significant uncertainty in hydrologic model calibrations which are currently based primarily on matching measured saturations. An example of such a calibration is the recent site-scale flow model of Wittwer et al. (1995), which was calibrated to saturations in well UZ-16 by using a infiltration boundary condition of 0.1 mm/y. However, recent analysis of data indicate substantially greater infiltration rates at Yucca Mountain (Hudson and Flint, 1995). Although preliminary, the work of Hudson and Flint estimates shallow infiltration rates that average greater than 20 mm/y over the area of interest. The isotopic tracer studies should prove beneficial in assessing how much of the shallow infiltration results in deep percolation.

Measured ^{36}Cl data for UZ-16 (Figure 3-1) show $^{36}Cl/Cl$ values ranging between 4×10^{-13} and 1×10^{-13}, corresponding to apparent ^{36}Cl residence times of between 100 and 700 ky. However, elevated $^{36}Cl/Cl$ values (relative to that of the pre-bomb meteoric water in this area) in the Calico Hills nonwelded unit (CHn) at 400 to 440 m depth indicate that water reaching this sample point is younger (fell as precipitation more recently) than the overlying water in the Topopah Springs welded unit (TSw). This age reversal associated with the chlorine-36 signal is currently being examined with respect to measurement of carbon-14 and tritium. Profiles for measurements of those two isotopes are also shown in Figure 3-1. In comparing the three signals, one sees an indication that there may in fact be young and possibly even very recent (post bomb-pulse) water in the Calico Hills. Interpretation of these data, however, is subject to great uncertainties and iscurrently under investigation by investigators Fabryka-Martin at Los Alamos and Yang at the USGS.

Another age reversal in the ^{36}Cl signal as measured in UZ-16 occurs at a depth of 44 to 67 m in the Paintbrush tuff (Liu et al., 1995). Here the matrix water is younger in the Paintbrush nonwelded unit than in the overlying Tiva Canyon welded unit. The cause of this increased signal of chlorine-36 in the matrix water appears to be due to rapid vertical movement of infiltrating water in fractures of the Tiva Canon welded unit above the Paintbrush tuff. This hypothesis is supported by the shallow moisture monitoring measurements and analysis of Hudson and Flint (1995) as well as tritium, ^{14}C, and ^{36}Cl measurements made of samples from the PTn. Moisture monioring and ^{36}Cl results of samples from shallow neutron monitoring boreholes both support the conceptual model that fracture flow is initiated beneath areas in which alluvial cover is shallow or missing, such as sideslopes and ridgetops. In these locations, bomb-pulse ^{36}Cl has been observed in the PTn; In contrast, it has not been observed at locations in which the PTn is overlain by thick alluvial cover (Fabryka-Martin et al., 1995).

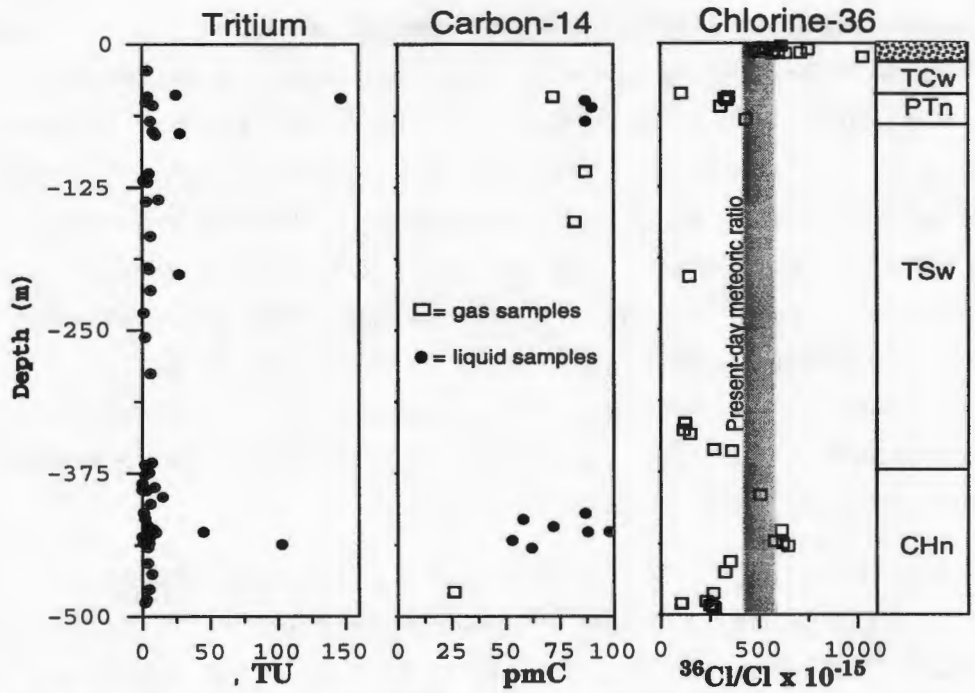

Figure 3-1.Isotopic Samples in UZ-16. TU = Tritium Units, pmC = percent modern carbon. Reference: Fabryka-Martin and Liu (1995), Yang et al. (1995).

Identifying the flow path and mechanism associated with the apparent younger water in the Calico Hills than in the overlying Topopah Springs is not as straightforward. One hypothesis suggests that infiltrating water moves vertically through all of the units (alternating welded and nonwelded tuffs) to the sample collection point in the Calico Hills. By moving through the fractures of the TSw, it would bypass the matrix, thus resulting in older matrix water measurements in that unit. One problem with this hypothesis is that it suggests a rapid travel path for vertically moving water through the nonwelded tuffs as well. An alternative hypothesis is that vertical deep percolation occurs in spatially isolated areas of significantly high infiltration. Then once it reaches the dipping beds of the Calico Hills it moves laterally to the point of sample collection.

Part of the problem associated with using isotopic tracers for these studies is that there is a discrepancy in apparent water ages depending on which isotope is considered. These discrepancies relate to the different half lives of ^{36}Cl, ^{14}C, and tritium, and the different flow paths that may be taken by the different isotopes. For example, ^{14}C, and to a lesser extent tritiated water, may travel in both the gas and liquid phase while ^{36}Cl can only travel in the liquid phase. Using the reactive transport module of FEHM, Viswanathan (1995) modeled the system as a gas-flow system with stagnant liquid, and simulated the movement of ^{14}C by treating the equilibrium carbonate chemistry. That study showed that even in the absence of any liquid movement, the younger ^{14}C

ages measured (in comparison with the ^{36}Cl apparent ages) could be explained by gas-phase transport with partitioning into the liquid phase.

Liu et al. (1995) demonstrate that such discrepancies are inevitable but, when understood, do not necessarily negate the value of isotopic studies aimed at understanding the hydrologic flow paths. As uncertainties associated with these various techniques, such as dilution with rock chloride or gas/liquid interactions of carbon, are understood and resolved, they pose a great potential to contribute to understanding a complex flow field. Better resolution of the flow paths will then lead to improved understanding of migration pathways of radionuclides.

3.5 Geochemical Composition Within Beds

The mineralogical composition of the stratigraphic beds presents a potential geochemical barrier to radionuclide migration. Also, there can be a strong correlation between changes in hydrologic properties such as permeabilities and fracture densities with changes in mineralogical composition. Of particular interest are the zeolitized subunits of the Calico Hills nonwelded tuffs. The zeolites in these zones have been shown to have substantial reactivity with radionuclides (Section 2.0). This reaction is particularly important for ^{237}Np as it has not been shown to sorb substantially to any of the other units below the potential repository. An interesting aspect of the zeolite rich units is that they tend to have lower matrix permeabilities than the devitrified nonwelded units surrounding them (Loeven, 1993).

DRAFT

4.0 Integration of Geologic Data of Structure and Stratigraphy into Flow and Transport Models

The process of transforming geologic, structural and stratigraphic data into computational physics models of flow and transport occurs into three steps. (1) A three-dimensional model is constructed which incorporates structure, stratigraphy, material boundaries, material properties, faults, as determined by geologic interpretation of data as well as surface infiltration information and the engineered infrastructure. This three-dimensional geometry model is a continuous description of geometry. (2) A computational grid is generated which involves producing a point distribution and connectivity at the resolution required for computations while preserving the geometry constructed in step (1). In addition, the grid must be optimized for computations. (3) Fluid flow and transport codes use the grid to initialize and solve differential equations representing physical processes. At this point, model output may motivate a reinterpretation of the stratigraphic model or may require new grids with changes in resolution. The section below describes the methods employed in the present study for carrying out the first two steps of this process.

4.1 Grid Generation Goals

As required by step (2) above, a numerical grid must be generated to accurately integrate complex three dimensional geometry into computational models. The creation of computational grids to represent complex three-dimensional geology, if done manually, is tedious, time consuming and prone to errors even in very simple cases. It is virtually impossible for large problems. GEOMESH, a grid generation software tool developed at Los Alamos National Laboratory (Gable et al., 1995), has streamlined the mesh generation process by interfacing to the X3D Grid Generation ToolBox (Trease, 1985; Trease, 1990; Trease, 1995; George, 1995; Khamayseh et al., 1995; and Kuprat et al., 1995). This allows more time to be spent on computations and interpretation of results. Automatic grid generation algorithms also offer flexibility. As upstream data changes or more data become available, it can easily be incorporated into computational models. Automatic grid generation can also be used to easily produce coarsened meshes for preliminary calculations and refined meshes for final, high resolution calculations.

4.2 Development of Three-dimensional Hydrogeologic Framework Models

4.2.1 Yucca Mountain Stratigraphic Section

A stratigraphic section of the three-dimensional model of Yucca Mountain based on the site scale flow model of Wittwer et al. (1995) is shown in Figure 4-1. The model contains three strata in the Tiva Canyon welded unit (TCw), three in the Paint brush Tuff nonwelded unit (PTn), six in the Topopah Springs welded unit, (TSw) and seven in the Calico Hills nonwelded

unit, (CHn). In addition, the potential repository is included within TSw and a thin unit parallel to the water table is included at the base of the model for applying boundary conditions.

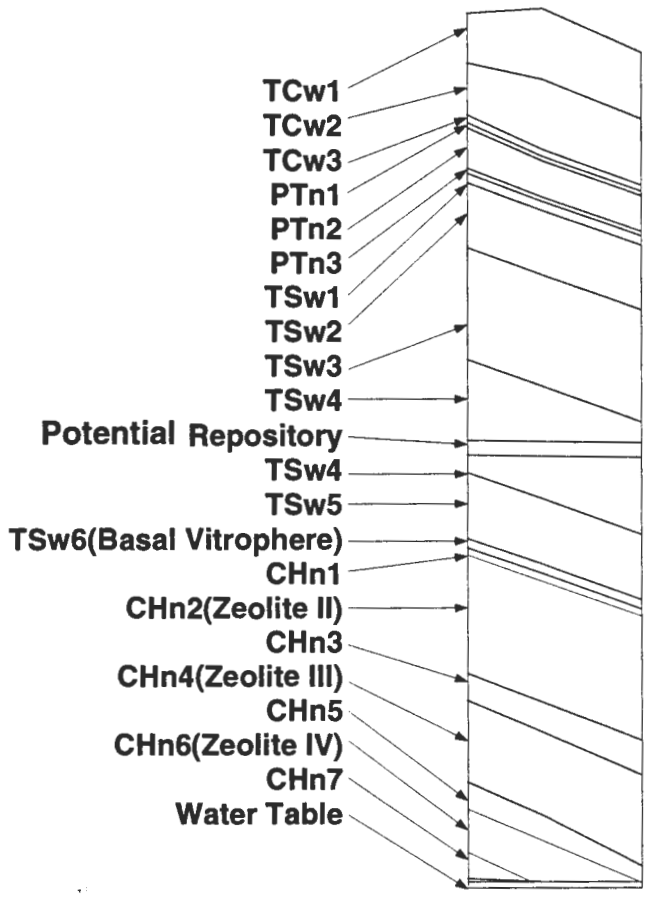

Figure 4-1. Example Stratigraphic Section of Yucca Mountain.

4.2.2 Framework Models

For this work, three different hydrogeologic frame work models are used. The first is a model that reproduces the hydrogeology of the LBL/USGS Three-Dimensional Site-Scale Model, (LBL/USGS model) (Wittwer et al., 1995), the second is a reinterpretation of the Calico Hills unit considering drill hole data to constrain the thickness and layering of zeolite subunits, (Nominal Zeolite) and the third is a model which uses the maximal credible thickness for the zeolite subunits in the Calico Hills unit, (Maximum Zeolite).

It was necessary to reinterpret stratigraphy for the Calico Hills unit because the LBL/USGS model does not accurately represent the way in which the layers of the Calico Hills unit intersect the water table. It appears that the method of subdividing the main hydrostratigraphic units by assigning the thicknesses proportionally has placed artifacts into the structural representation of the

layers. For example, an east-west cross section at Antler Ridge, Nevada State Coordinate 232750 meters North, (see Figure 4-2) illustrates that the LBL/USGS model has all of the Calico Hills units pinching out at a point, or along a line in three dimensions. In the nominal and maximum zeolite models developed for this study, a more realistic termination of the strata by the water table is used. Furthermore, the nominal and maximum zeolite models fit the drill hole data provided by LANL geologists and presented in Tables 4-1 to 4-6).

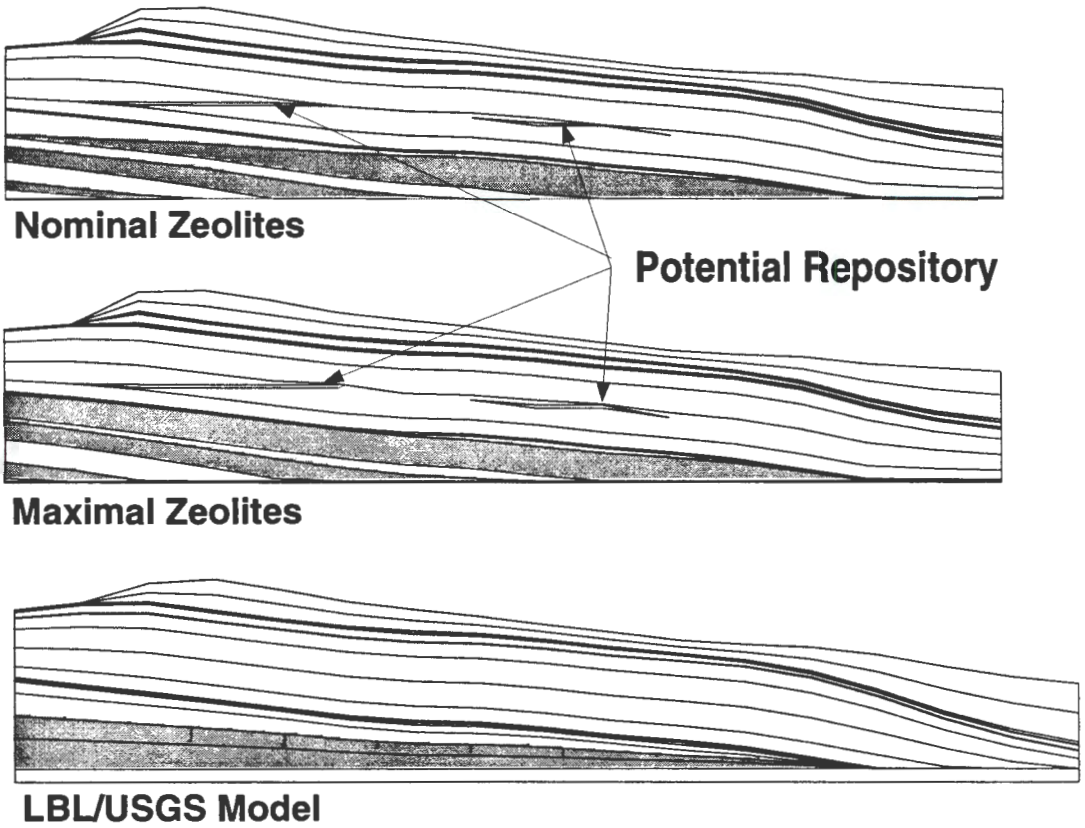

Figure 4-2. East-west cross sections through Antler Ridge illustrate the difference in the Calico Hills units for the three structural models. In the LBL/USGS model all units pinch out at a single point. The nominal and maximum zeolite models correspond more closely to drill hole data.

4.2.3 LBL/USGS Model

In this section, we briefly describe the development of a hydrostratigraphic model that is used to compare directly with the LBL/USGS unsaturated zone flow model (Wittwer et al., 1995). In Section 6.2, a comparison of calculated saturations of the two models is presented.For each of the 18 units of the LBL/USGS model, isopach data were supplied to Los Alamos at approximately 280 locations covering the site scale model. Each of the locations represents the North-South and East-West coordinates of the LBL/USGS integrated finite difference grid.

Although irregularly spaced, these cell centers are positioned with a nominal intercell spacing of approximately 500 meters. At locations where individual units were not observed due to outcrop or pinchout, the data files contained zeros. The data from each isopach is then contoured and used to construct a Stratigraphic Framework Model as described in Section 4.3.

4.2.4 Development of Calico Hills Nominal and Maximal Zeolite Stratigraphy

After constructing a computational model from the LBL/USGS Site Scale Hydrologic model, it became apparent that the zeolites of the Calico Hills unit were not represented with sufficient accuracy for this study. In order to understand sensitivity of radionuclide transport, a new model of the Calico Hills unit was developed with the help of Dave Vaniman and Dave Bish of the LANL Min/Pet staff (personal communication, 1995). The intent here was to construct a nominal model of the Calico Hills Unit as a base case and construct a maximum credible zeolite zone to test the best case scenario for ^{237}Np retardation by zeolites (see Tables 4-1 to 4-6).

Table 4-1. Vitric Nonwelded (lower Topopah/Calico Hills)

Nevada State Coordinates N-S meters	Nevada State Coordinates E-W meters	Nominal Thickness, meters	Maximum Thickness, meters	Drill Hole Designation
234841.39	170992.80	15.50	15.20	G-1
233404.87	171613.37	5.50	5.50	G-4
229407.72	170229.89	101.20	61.00	GU/G-3
230595.22	170214.34	81.70	23.80	H-3
232148.79	171877.94	30.20	29.00	H-4
233667.00	170351.81	73.50	3.40	H-5
232641.65	168909.80	72.50	22.60	H-6
233247.29	172623.48	6.10	0.00	UE-25b
231811.07	172168.72	3.10	0.00	UZ-16
229801.22	171827.65	0.00	0.00	WT-1
231849.47	171274.44	70.10	0.00	WT-2
237379.15	170844.36	2.40	0.00	G-2
230480.92	174188.63	0.00	0.00	P-1
234104.08	171172.94	4.00	1.00	SD-9
232244.49	171177.51	22.30	1.00	SD-12

DRAFT

Table 4-2. Zeolite II (lower Topopah/Calico Hills)

Nevada State Coordinates N-S meters	Nevada State Coordinates E-W meters	Nominal Thickness, meters	Maximum Thickness, meters	Drill Hole Designation
234837.73	170992.80	144.80	154.50	G-1
233399.69	171606.97	130.80	131.40	G-4
229407.11	170229.58	0.00	70.70	GU/G-3
230595.22	170214.34	0.00	114.00	H-3
232149.40	171875.81	98.80	104.90	H-4
233667.30	170350.89	36.30	112.50	H-5
232641.65	168909.80	0.00	56.10	H-6
233245.46	172618.60	166.40	172.50	UE-25b
231811.07	172168.72	94.50	110.60	UZ-16
229801.22	171827.65	74.70	85.30	WT-1
231849.47	171274.44	70.10	161.50	WT-2
237375.19	170828.21	386.50	396.20	G-2
230480.92	174188.63	57.90	64.00	P-1
234104.08	171172.94	137.20	148.20	SD-9
232244.49	171177.51	97.50	123.80	SD-12

Table 4-3. Devitrified Prow Pass

Nevada State Coordinates N-S meters	Nevada State Coordinates E-W meters	Nominal Thickness, meters	Maximum Thickness, meters	Drill Hole Designation
234832.25	170992.80	39.30	24.40	G-1
233391.76	171596.61	51.20	48.20	G-4
229401.62	170227.75	44.20	13.40	GU/G-3
230596.14	170213.12	57.90	1.80	H-3
232150.01	171874.59	36.60	27.70	H-4
233667.30	170350.28	33.50	21.30	H-5
232641.65	168908.27	53.30	34.80	H-6
233245.15	172616.47	57.90	48.80	UE-25b
231811.07	172168.72	54.90	41.20	UZ-16

DRAFT

Table 4-3. Devitrified Prow Pass (Continued)

Nevada State Coordinates N-S meters	Nevada State Coordinates E-W meters	Nominal Thickness, meters	Maximum Thickness, meters	Drill Hole Designation
N/A	N/A	N/A	N/A	WT-1
231849.47	171274.44	33.50	21.30	WT-2
237370.32	170809.92	100.60	68.90	G-2
230480.92	174188.63	73.20	61.00	P-1
234104.08	171172.94	45.70	30.00	SD-9
232244.49	171177.51	40.50	30.00	SD-12

Table 4-4. Zeolite III (basal Prow Pass)

Nevada State Coordinates N-S meters	Nevada State Coordinates E-W meters	Nominal Thickness, meters	Maximum Thickness, meters	Drill Hole Designation
234825.54	170992.80	97.50	125.00	G-1
233386.27	171587.46	90.80	94.80	G-4
229396.44	170223.18	98.80	99.40	GU/G-3
230597.35	170209.16	88.40	118.90	H-3
232151.22	171871.84	162.20	172.20	H-4
233667.30	170349.67	67.10	79.30	H-5
232641.65	168907.97	26.20	46.00	H-6
233243.32	172611.29	94.50	103.60	UE-25b
N/A	N/A	N/A	N/A	UZ-16
N/A	N/A	N/A	N/A	WT-1
231849.47	171274.44	70.10	82.30	WT-2
237368.79	170805.35	68.30	103.00	G-2
230480.92	174188.63	48.80	70.10	P-1
234104.08	171172.94	94.50	102.20	SD-9
232244.49	171177.51	83.80	89.30	SD-12

DRAFT

Table 4-5. Devitrified Bullfrog

Nevada State Coordinates N-S meters	Nevada State Coordinates E-W meters	Nominal Thickness, meters	Maximum Thickness, meters	Drill Hole Designation
234820.36	170990.36	68.90	47.20	G-1
233380.18	171571.62	129.20	127.40	G-4
229388.21	170214.95	133.50	121.00	GU/G-3
230597.05	170210.38	98.50	45.70	H-3
232151.53	171870.62	88.10	77.70	H-4
233667.30	170348.76	111.30	99.10	H-5
232641.65	168906.75	104.90	67.40	H-6
233239.36	172600.92	119.20	103.90	UE-25b
N/A	N/A	N/A	N/A	UZ-16
N/A	N/A	N/A	N/A	WT-1
N/A	N/A	N/A	N/A	WT-2
237368.49	170802.00	49.40	32.90	G-2
230480.92	174188.63	109.70	85.30	P-1
234104.08	171172.94	0.00	0.00	SD-9
232244.49	171177.51	0.00	0.00	SD-12

Table 4-6. Zeolite IV (Bullfrog/Tram)

Nevada State Coordinates N-S meters	Nevada State Coordinates E-W meters	Nominal Thickness, meters	Maximum Thickness, meters	Drill Hole Designation
234817.01	170990.36	64.30	78.00	G-1
233379.26	171568.57	44.50	47.90	G-4
229388.21	170214.95	61.00	79.30	GU/G-3
230597.35	170209.77	52.70	81.10	H-3
232151.83	171870.32	65.20	75.60	H-4
233667.30	170348.76	41.80	54.00	H-5
232641.65	168906.14	61.60	97.50	H-6
233235.40	172590.56	41.20	60.70	UE-25b
N/A	N/A	N/A	N/A	UZ-16

DRAFT

Table 4-6. Zeolite IV (Bullfrog/Tram) (Continued)

Nevada State Coordinates N-S meters	Nevada State Coordinates E-W meters	Nominal Thickness, meters	Maximum Thickness, meters	Drill Hole Designation
N/A	N/A	N/A	N/A	WT-1
N/A	N/A	N/A	N/A	WT-2
237368.18	170798.95	42.70	92.70	G-2
230480.92	174188.63	45.70	64.00	P-1
234104.08	171172.94	0.00	0.00	SD-9
232244.49	171177.51	0.00	0.00	SD-12

4.2.5 Repository Design

Incorporation of the potential repository as an integral part of the computational grid is important for studying the thermal effects of the repository and for radionuclide release and migration. The coordinates used to define the potential repository were obtained from David Jefferis of EG&G and were extracted from the Earth Vision Site Geologic Framework Model V1 (personal communication, David Jefferis, 1995). The data defines coordinates of 224 parallel drifts. The potential repository is broken into two sections; a set of drifts West of the Ghost Dance Fault and a set of drifts to the East (Figure 4-3). For this study, the potential repository coordinates are used to define the perimeter of two volumes. The coordinates defining the repository are plotted in Figure 4-3 and can be obtained from the Earth Vision Site Geologic Framework Model.

4.3 Incorporating Data into Stratamodel

The data sets described above are imported into the geologic modeling package Stratamodel in order to integrate this data into a stratigraphic framework model. First, a continuous surface is fit to the data points defined by the drill hole data (Table 4-1 to 4-6) or to the stratigraphy defined by the LBL/USGS hydrologic model. The surface is then sampled at regular intervals in the East-West and North-South directions. For this work quadrilateral grids were produced at 250m and 500m resolution.

The next step involves converting isopach data into stratigraphic layering. Beginning with a baseline defined by the water table, isopachs of stratigraphic thicknesses above the water table are added sequentially. This produces grids that represent the base of each stratigraphic unit.

DRAFT

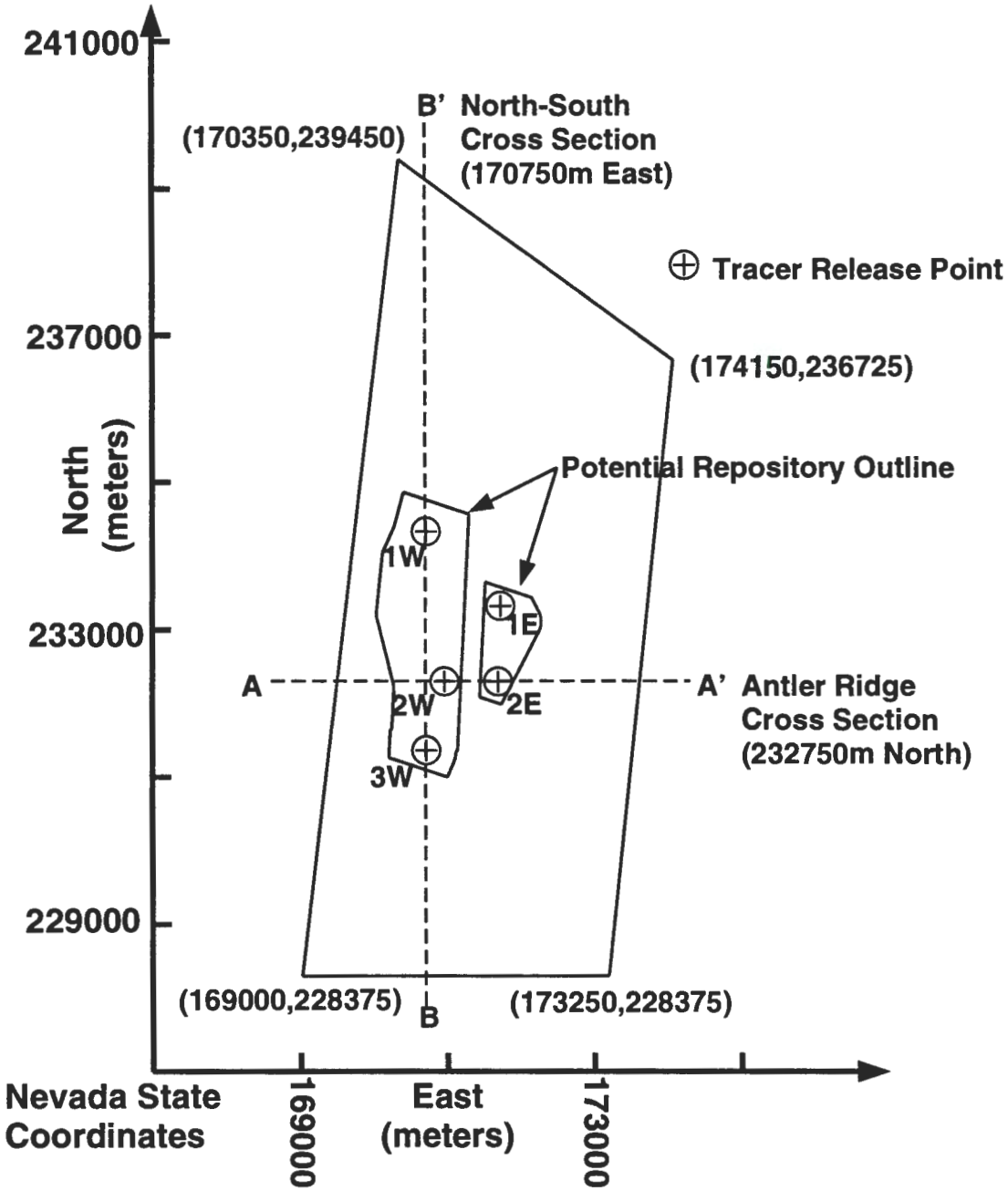

Figure 4-3.Outline of model area and potential repository.

Next, an "area of interest" is chosen to define the areal extent of the grids to be used. To reproduce the LBL/USGS model, a polygon is defined and any grid blocks that fall outside the polygon are eliminated (Table 4-7, Figure 4-3).

After all stratigraphic layers are created and imported into Stratamodel, a Stratigraphic Framework Model (SFM) is constructed with Stratamodel. This model is a logically structured

Table 4-7. Polygon Defining Stratigraphic Model Area

Nevada State Coordinates N-S meters	Nevada State Coordinates E-W meters
239450	170350
228375	169000
228375	173250
236725	174150

array of hexahedral elements with regular spacing in the x and y directions (East and North), and variable spacing in the vertical z direction. While this model provides a well defined geometric model of the three-dimensional stratigraphy, it has qualities which make it impossible to use directly for flow and transport calculations. This SFM can however be used as input into the GEOMESH grid generation software developed at Los Alamos and described in the next section.

4.4 GEOMESH/X3D Grid Generation

Automated grid generation provides a valuable link between a geologic model of structure and stratigraphy and a computational model of flow and transport. It also ensures that constraints on grid discretization are optimized to insure accuracy and stability of the numerical solutions to flow and transport physics.

The translation of a stratigraphic framework model (SFM) defined in Stratamodel to a computational mesh is accomplished using the software tool GEOMESH (Gable et al., 1995). The resulting computational grid is constructed of tetrahedra (in 3-D) or triangles (in 2-D). The grid is Delaunay, coupling coefficients are positive, and all material interfaces are accurately preserved.

GEOMESH differs from other grid generators because it has been designed to meet needs specific to geologic features such as faulting, beds which pinch out, irregular external surfaces defined by topography, and the representation of wells and tunnels. There are a number of commercial products that aid in building three dimensional representations of geologic structures (Lynx, Dynamic Graphics, Stratamodel). However, these products do not prepare output which is usable by finite element and finite difference flow and transport modeling programs. There are also products which convert stratigraphic models to computational grids. However these computational grids do not strictly honor the geometric integrity of the original model as GEOMESH does.

GEOMESH interfaces to the X3D Grid Generation ToolBox (Trease, 1985; Trease, 1990; Trease, 1995; and George, 1995) for grid generation services such as Delaunay triangulation,

Voronoi/Median grid generation, coupling coefficient calculations, grid reconnections, grid refinement and grid interpolation.

4.4.1 Delaunay Triangulation, Voronoi Grids and Median Grids

The approach to grid generation results in the construction of an unstructured grid of triangles in 2-D or tetrahedra in 3-D. In contrast, a structured grid is typically constructed of quadrilaterals in 2-D or hexahedra in 3-D. While numerical algorithms are often easier to implement on structured grids (i.e. finite difference methods), they lack adaptivity in applications that must represent complex geometry, such as the stratigraphy of Yucca Mountain.

Voronoi grids and Delaunay triangulations have been described by mathematicians and physicists for nearly one hundred years and there are many way to define them (Bern and Eppstein, 1992). A Voronoi point is defined as the center of a circle that passes through the three vertices of a triangle. If the Voronoi point is inside or on the triangle, the triangle is a Delaunay triangle. This can be generalized to 3-D with a sphere circumscribed around a Delaunay tetrahedron. A Delaunay mesh consists of a set of Delaunay triangles (or tetrahedra) such that the circle (or sphere) circumscribing each triangle (tetrahedron) contains no mesh points other than the vertices of the triangle (tetrahedron). This excludes the degenerate case where a Voronoi point falls on the edge of the triangle or the face of the tetrahedron.

A Median mesh is formed by connecting the centroid of each triangle with the midpoint of each triangle edge. Although some numerical methods use this mesh, median mesh is not used for computations presented in this study.

A Voronoi mesh and the Delaunay mesh are duals of one another, that is one can be derived from the other. The Voronoi mesh is unique. However the Delaunay mesh may not be. An example comparing the Delaunay, Voronoi, and Median mesh is shown in Figure 4-4.

An example from the western edge of an Antler Ridge cross section (Figure 4-5), shows the Delaunay and Voronoi grids used for flow and transport calculations. The Delaunay mesh is the actual finite element grid, with the triangles or tetrahedra representing the finite elements. The cells of the Voronoi grid represent the control volume and area terms associated with each grid point.

The grids produced by GEOMESH are extremely versatile and not specific to any particular computational flow and transport code. The grids can be used by any numerical algorithm that utilizes unstructured grids.

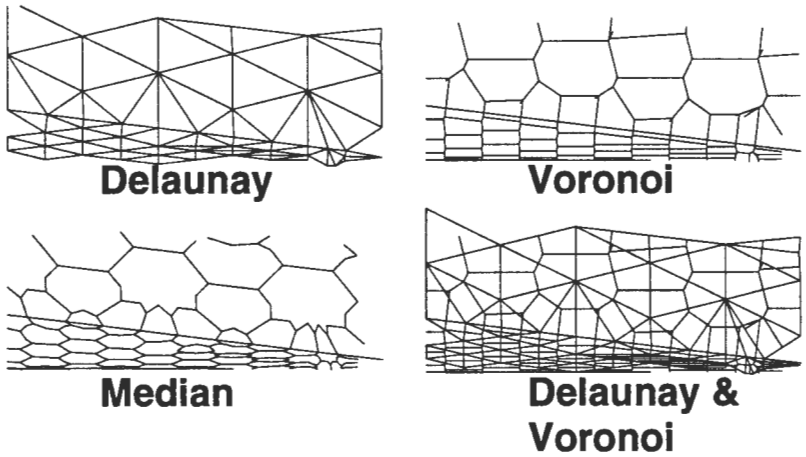

Figure 4-4. Different numerical algorithms use different discretizations of a point distribution to solve computational physics problems. GEOMESH can output grids in a variety of formats.

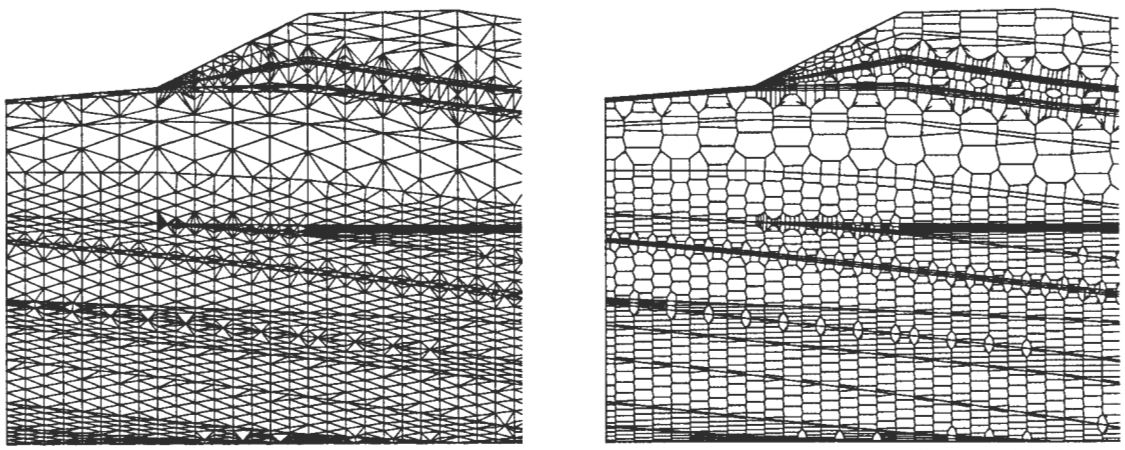

Figure 4-5. The left figure is the Delaunay triangulation, the right figure is the Voronoi mesh. A Voronoi mesh and a Delaunay mesh are duals of one another.

4.4.2 Positive Coupling Coefficients

An additional constraint that must be met in the grid generation process is to ensure that all coupling coefficients are positive. Coupling coefficients are defined as the coefficients of the matrix A in the numerical solution of the diffusion equation,

$$[A](X) = (B) \tag{4-1}$$

where,

A = Coupling coefficients between mass points

X = field variable at time = t + delta t

DRAFT

B = field sources and sinks at time = t.

Each component of the matrix $A_{i,j}$ is the vector area between grid point i and j in tetrahedron l (the Voronoi or median mesh face connecting the i,j Voronoi or median mesh points). The grid generation algorithm ensures that the matrix **A** is symmetric semi-positive definite (Trease and Dean, 1990).

4.4.3 Reconnection of Tetrahedra to Ensure Delaunay Mesh Conditions

In cases for which there is only a single material, a Delaunay mesh can be constructed by flipping element connections until the Delaunay criteria is satisfied (see Figure 4-6). However,

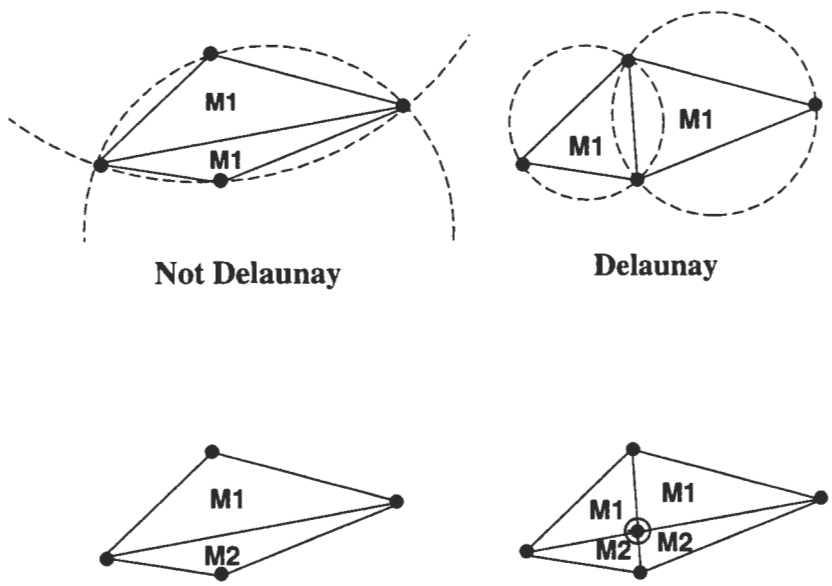

Figure 4-6. Example of a four point distribution connected to form a Delaunay triangulation. In the upper figure both triangles are the same material so the triangulation is made Delaunay by flipping a connection. In the lower figure, the triangles on the left are different material, so the triangulation is made Delaunay by adding a point on the interface and making four triangles from the original two.

when there are multiple materials, connections cannot be flipped if material interfaces are not maintained. In that case, new nodes are automatically added along the material interface. This results in a Delaunay grid that maintains the geometric integrity of complex material interface.

4.4.4 Grid refinement

Grid refinement capabilities have been developed allowing one to increase resolution of a grid. This is useful to resolve physics on a fine scale or to test the convergence of a numerical solution. Three methods of grid refinement are used; edge refinement, face refinement and volume refinement. Edge refinement is done by adding a new grid point to the center of each

edge of a tetrahedra. This results in 1 tetrahedron becoming 8 tetrahedra. Face refinement adds a new grid point to the face center of each tetrahedron, resulting in 9 tetrahedra. Volume refinement adds a new grid point to the centroid of a tetrahedron, resulting in 4 tetrahedra.

Controlling which portion of a grid is refined is accomplished by various methods. The simplest is to define a three-dimensional rectangular box by defining two points resulting in all elements falling inside the box being refined. One can also define zones of refinement based on material type.

4.4.5 Grid Interpolation

In order to restart calculations after grid refinement, or to compare solutions on completely different grids, capabilities have been developed to interpolate field values from one grid onto another. This has been utilized in two ways. First, algorithms to interpolate field quantities from one grid to another are used to speed convergence of fine grid calculations. For example, in order to obtain a steady state saturation field it is faster to interpolate a course grid solution onto a fine grid rather than start the fine grid calculation without any prior information.

The second application involves interpolating the saturation field published in Wittwer et al. (1995), provided by LBL scientists, onto grids used by FEHM. This requires the ability to calculate grid connectivity from a scattered point data set (i.e. x, y, z, coordinates and saturation values with no connectivity provided). These results and comparisons are shown in Section 6.2.

4.4.6 Output from grid generation process

The grid generation process produces information about the mesh that can be used by finite element, finite volume, and integrated finite difference physics codes. Some of the information is used to define finite difference operators (Div, Grad, Curl) while other information is used for setting initial and boundary conditions.

The data listed below is used by FEHM for model setup and is also used by graphics and postprocessing software.

- Node coordinates - x, y, z coordinates of every node in the mesh.
- Node color - any number of floating point values associated with each node. This could represent any property of the material (intrinsic variables, i.e. density, porosity, etc.) or could be values derived from a model simulation (i.e. temperature, pressure, etc.)
- Node type - Every node has an associated integer indicating if it is inside the mesh, outside the mesh or on a material interface. Outside nodes have additional information indicating which of the external faces they are on.
- Node connectivity - A list indicating the neighboring nodes connected to any node.
- Element color - Every element has an associated integer indicating which material it belongs to. This is useful for assigning material properties in physics codes and is used as a constraint during grid reconnection.

DRAFT

- Element connectivity - provides a node list associated with each element describing how nodes are connected to form an element.
- Face connectivity - A list associating any face of an element with the corresponding face of the element that shares that face.
- Area coefficients, representing the information FEHM needs for a complete set-up of the finite element calculation (FEHM *.stor file)
- Zone files - three files provide lists of nodes sorted by (a) material type, (b) material interface and (c) outside face type. These lists are useful for setting initial and boundary conditions.

4.4.7 Description of Three-dimensional Computational Grid, LBL/USGS Model

The computational grid used to compare flow results using FEHM to results of the LBL/USGS models are carried out on a grid with 14,150 nodes and 82,459 tetrahedral elements. While this is at a somewhat higher resolution than the grid used by Wittwer et al. (1995), our experience demonstrated that increased resolution is necessary, especially for resolving the very thin stratigraphic units. A flow calculation using this grid is described in Section 6.2. Transport calculations were performed only on the grids generated from the rebuilt Calico Hills unit. While a single number cannot adequately characterize the resolution of an unstructured tetrahedral grid, the nominal resolution in the horizontal direction is approximately 250 meters. The data distribution obtained from the model of Wittwer et al. (1995), has a total of 5516 nodes and appears to have a nominal horizontal resolution of approximately 500 meters.

4.4.8 Description of Three-dimensional Computational Grid, Nominal Zeolite Model

Three-dimensional flow and transport calculations (see Sections 6.6 and 7.3) use a high resolution computational grid of 51,550 nodes and 312,465 tetrahedral elements. This grid includes the potential repository as one of the zones. For these calculations, that zone was given the material properties of TSw4. The nominal horizontal resolution of the grid is 125 meters. It was determined that this higher resolution was necessary to accurately calculate transport solutions.

4.4.9 Description of 2-D cross section computational grids

Two-dimensional flow and transport calculations were carried out on an East-West cross section through Antler ridge (A-A', Figure 4-3) and on a North-South cross section (B-B', Figure 4-3). These cross sections were chosen to pass through some portion of the potential repository. The grids used for computation have the highest resolution in TSw4 and below (Figure 4-7). The increased resolution is necessary to accurately model transport of radionuclides from the potential repository which is contained in TSw4. The two-dimensional Antler Ridge grids at different spatial resolutions used in the transport analyses are shown in Figure 4-8. Table summarizes the statistics of all grids used in the present study.

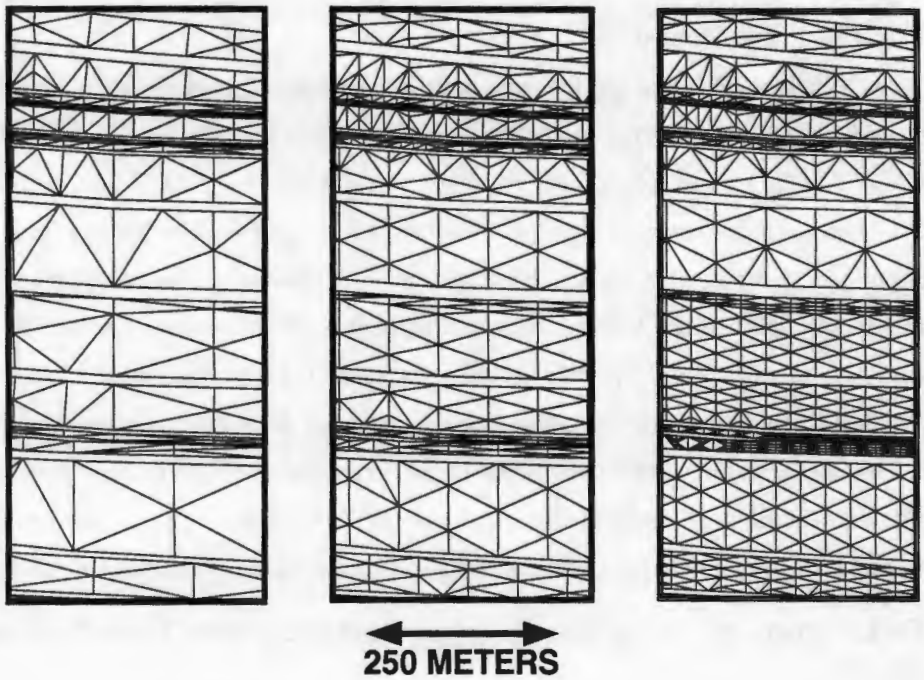

Figure 4-7. A small section of Antler Ridge cross section grids split apart at stratigraphic boundaries. Grid refinement is used to first refine the entire grid and then only the portion that is below the potential repository.

DRAFT

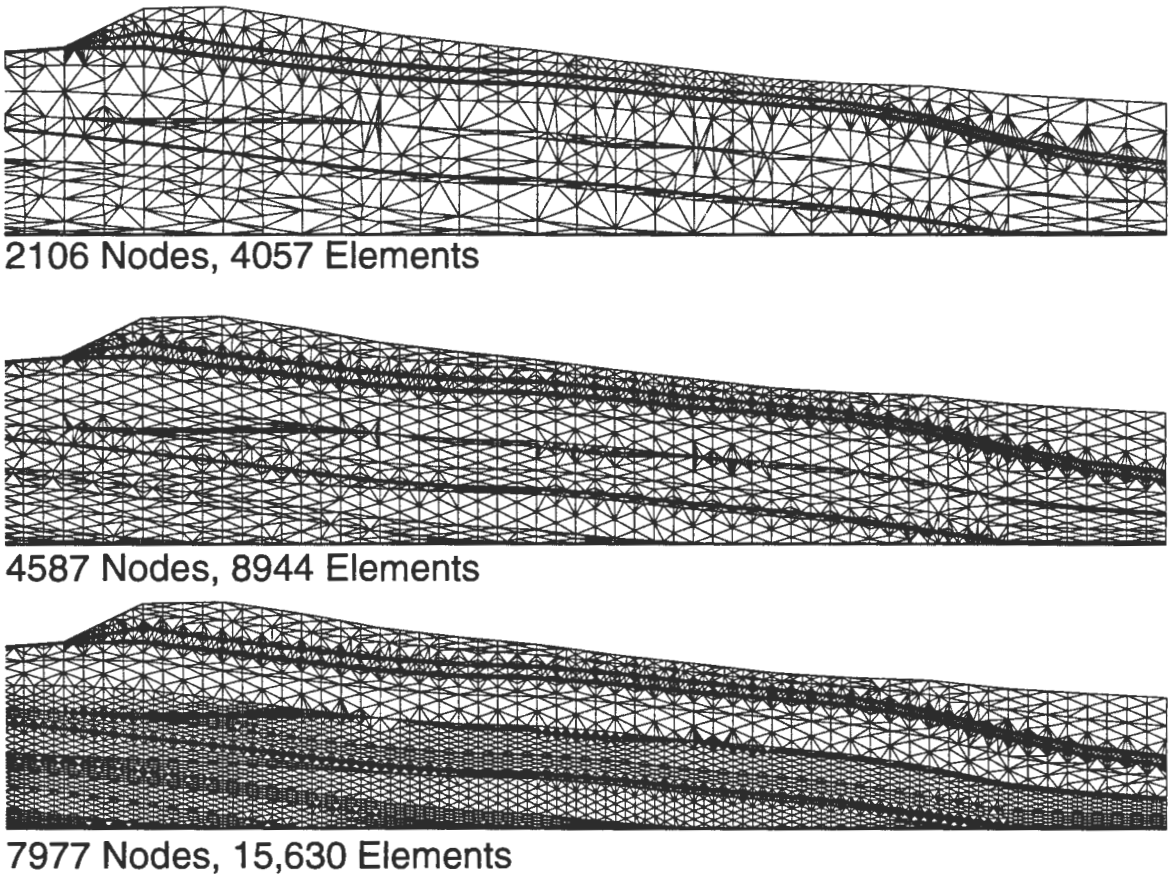

Figure 4-8. Antler Ridge cross section at three different resolutions. Initial calculations on low resolution grid indicated more resolution was required. The entire grid was then refined followed by the materials at or below the potential repository. All two-dimensional flow and transport calculations use the highest resolution grid.

Table 4-8. Computational Grids Used in Modeling Flow and Transport

Model Area	Calico Hills Zeolite Model	Number of Nodes	Number of Elements	Horizontal Resolution (meters)	Purpose
3-D Whole Site	LBL/USGS	14,150	82,459	250	Compare with LBL/ USGS Model
3-D Whole Site	Nominal Zeolite	13,491	78,463	250	Dual permeability calculations
3-D Whole Site	Nominal Zeolite	51,550	312,465	125	Flow and transport calculations
2-D East-West Antler Ridge, coarse	Nominal Zeolite	2,106	4,057	125	Grid resolution study
2-D East-West Antler Ridge, intermediate	Nominal Zeolite	3925	7628	60	Grid Resolution study
2-D East-West Antler Ridge, fine resolution	Nominal Zeolite	7,977	15,630	30	Flow and transport calculations
2-D East-West Antler Ridge	Maximum Zeolite	8467	16,604	30	Flow and transport calculations
2-D North-South West Repository	Nominal Zeolite	16,195	31,801	30	Flow and transport calculations

5.0 Mathematical Methods Used in Transport Calculations

The computer code used for the site scale flow and transport model calculations is the Finite Element Heat and Mass (FEHM) code. The code solves the equations of heat and mass transport in porous and fractured media in two or three dimensions. The code also offers a comprehensive set of models for simulating the transport of dissolved species in either the gas or liquid phase. This section outlines the mathematical models and model assumptions of the FEHM options employed in the simulations of this report. The equations are represented numerically using the finite element method, a technique for solving the conservation equations that is especially well suited for numerical grids that accurately depict irregular geometries. Refer to code documentation for additional details on other FEHM code options (Zyvoloski et al., 1995a, Zyvoloski et al., 1995b), numerical methods (Zyvoloski, 1983), and code verification problems (Dash et al., 1995a, b).

5.1 Hydrologic Flow Mathematical Models

Simulation of the transport of a dissolved species first requires that the flow of the carrier fluid (liquid water or gas) be computed, after which the solute is typically simulated as a species that is present in trace quantities, and therefore does not alter the behavior of the fluids. This assumption is almost certainly valid for the dissolved radionuclides and environmental isotopes modeled in the present study. Below we briefly outline the flow model options of FEHM used in this report.

5.1.1 Water/vapor/air/heat model

This option is the starting point for describing the FEHM heat and fluid mass transfer simulation capabilities. This model will be the primary one used in the future when the impact of repository heat on thermohydrologic conditions and radionuclide transport are studied. We outline the model equations in detail, and in subsequent sections we treat the simplifications to the model that are more computationally efficient.

Detailed derivations of the governing equations for two-phase flow including heat transfer have been presented by several authors (e.g., Mercer and Faust, 1975, and Brownell, et al. 1975), and therefore only a brief development will be presented here.

Conservation of mass for water is expressed by the equation

$$\frac{\partial A_m}{\partial t} + \overline{\nabla} \cdot \overline{f_m} + q_m = 0, \tag{5-1}$$

where the mass per unit volume, A_m, is given by

$$A_m = \phi(S_v \rho_v (1 - \eta_v) + S_l \rho_l (1 - \eta_l)) \tag{5-2}$$

and the mass flux, $\overline{f_m}$, is given by

$$\overline{f_m} = (1-\eta_v)\rho_v\overline{v_v} + (1-\eta_l)\rho_l\overline{v_l} \ . \tag{5-3}$$

Here ϕ is the porosity of the matrix, S is saturation, ρ is density, η is the concentration of the noncondensible gas and is expressed as a fraction of the total mass, and $\bar{v}$ is velocity with the subscripts v and l indicating quantities for the vapor phase and the liquid phase, respectively. Source and sink terms (such as reinjection wells, infiltration, or groundwater recharge) are represented by the term q_m.

Conservation of fluid-rock energy is expressed by the equation

$$\frac{\partial A_e}{\partial t} + \overline{\nabla} \cdot \overline{f_e} + q_e = 0, \tag{5-4}$$

where the energy per unit volume, A_e, is given by

$$A_e = (1-\phi)\rho_r u_r + \phi(S_v\rho_v u_v + S_l\rho_l u_l) \tag{5-5}$$

with $u_r = c_{pr}T$, and the energy flux, $\overline{f_e}$, is given by

$$\overline{f_e} = \rho_v h_v \overline{v_v} + \rho_l h_l \overline{v_l} - K\overline{\nabla}T \ . \tag{5-6}$$

Here the subscript r refers to the rock matrix; u_r, u_v, and u_l are specific internal energies; c_{pr} is the specific heat; h_v and h_l are specific enthalpies; K is an effective thermal conductivity; T is the temperature; and q_e is the energy contributed from sources and sinks.

To complete the governing equations it is assumed that Darcy's Law applies to the movement of each phase:

$$\overline{v_v} = -\frac{kR_v}{\mu_v}(\overline{\nabla}P_v - \rho_v\bar{g}) \tag{5-7}$$

and

DRAFT

$$\bar{v}_l = -\frac{kR_l}{\mu_l}(\bar{\nabla}P_l - \rho_l\bar{g}) \ . \tag{5-8}$$

Here k is the permeability, R_v and R_l are the relative permeabilities, μ_v and μ_l are viscosities, P_v and P_l the phase pressures, and g represents the acceleration due to gravity (the phase pressures are related by $P_v = P_l + P_{cap}$, where P_{cap} is the capillary pressure). For simplicity, the equations are shown for an isotropic medium, an assumption employed in the present study, even though this restriction does not exist in the computer code.

Using Darcy's Law the basic conservation Equations (5-1) through (5-4) can be combined

$$-\bar{\nabla}\cdot((1-\eta_v)D_{mv}\bar{\nabla}P_v) - \bar{\nabla}\cdot((1-\eta_l)D_{ml}\bar{\nabla}P_l) + q_m +$$
$$\frac{\partial}{\partial z}g((1-\eta_v)D_{mv}\rho_v + (1-\eta_l)D_{ml}\rho_l) + \frac{\partial A_m}{\partial t} = 0 \tag{5-9}$$

and

$$-\bar{\nabla}\cdot(D_{ev}\bar{\nabla}P_v) - \bar{\nabla}\cdot(D_{el}\bar{\nabla}P_l) - \bar{\nabla}\cdot(K\bar{\nabla}T) + q_e +$$
$$\frac{\partial}{\partial z}g(D_{ev}\rho_v + D_{el}\rho_l) + \frac{\partial A_e}{\partial t} = 0 \tag{5-10}$$

where z is oriented in the direction of gravity. Here the transmissibilities are given by

$$D_{mv} = \frac{kR_v\rho_v}{\mu_v}, \ D_{ml} = \frac{kR_l\rho_l}{\mu_l} \tag{5-11}$$

and

$$D_{ev} = h_v D_{mv}, \ D_{el} = h_l D_{ml} \ . \tag{5-12}$$

If the total mass withdrawal, q_m, for each sink is specified, then the energy withdrawal, q_e, is determined as follows:

$$q_e = q_v h_v + q_l h_l \tag{5-13}$$

where

DRAFT

$$q_v = \nu q_m, \; q_l = (1-\nu) q_m \tag{5-14}$$

and

$$\nu = \frac{1}{1 + \dfrac{\rho_l R_l \mu_v}{\rho_v R_v \mu_l}} \; . \tag{5-15}$$

The mass flux, $\overline{f_\eta}$, source (or sink) strength, q_η, and accumulation term, A_η, are defined as follows for the noncondensible gas conservation equation:

$$\overline{f_\eta} = \eta_v \rho_v \overline{v_v} + \eta_l \rho_l \overline{v_l} \; , \tag{5-16}$$

$$q_\eta = \eta_v q_v + \eta_l q_l \; , \tag{5-17}$$

$$A_\eta = \phi(\eta_v S_v \rho_v + \eta_l S_l \rho_l) \; . \tag{5-18}$$

The noncondensible gas conservation equation is

$$-\overline{\nabla} \cdot (\eta_v D_{mv} \overline{\nabla} P_v) - \overline{\nabla} \cdot (\eta_l D_{ml} \overline{\nabla} P_l) - \overline{\nabla} \cdot (D_{va} \overline{\nabla} \eta_v) + q_\eta +$$

$$\frac{\partial}{\partial z} g(\eta_v D_{mv} \rho_v + \eta_l D_{ml} \rho_l) + \frac{\partial A_\eta}{\partial t} = 0 \; . \tag{5-19}$$

Fluid sources and sinks are input to the model domain via either constant pressure, flow rate, or saturation boundary conditions. For the present study, the infiltration boundary condition uses a flow rate boundary condition, while the water table is simulated by holding the saturation at the nodes at a high value.

5.1.2 Isothermal air-water model

For situations in which heat effects are minimal, the hydrologic model can be simplified. Since the present study does not address through numerical simulation the impact of repository heat on radionuclide migration, the solution of the full heat and mass transfer solution is not needed. The isothermal air-water two phase system in FEHM is represented somewhat differently then the nonisothermal system defined above. Here the liquid phase is pure water and the vapor phase is pure air. The component mass balance equations are then also phase balance equations:

DRAFT

$$\frac{\partial}{\partial t}(\phi\rho_l S_l) - \overline{\nabla}\cdot(D_{ml}\overline{\nabla}P_l) + q_{ml} + \frac{\partial}{\partial z}g(D_{ml}\rho_l) = 0 \quad , \tag{5-20}$$

$$\frac{\partial}{\partial t}(\phi\rho_v S_v) - \overline{\nabla}\cdot(D_{mv}\overline{\nabla}P_v) + q_{mv} + \frac{\partial}{\partial z}g(D_{mv}\rho_v) = 0 \quad . \tag{5-21}$$

where Equation (5-20) is the water balance equation and Equation (5-21) refers to the conservation of air. Here the subscript l refers to the liquid water properties and v refers to air properties. The practical advantage of this option is to reduce the number of degrees-of-freedom (unknowns per spatial position) from three to two, thereby increasing computational efficiency.

A further simplification can be made in which the air pressure is assumed to be constant. This leads to an equation which is similar to the Richard's equation for unsaturated flow. The method reduces to one in which only Equation (5-20) is solved. The Richard's equation option is not used in the present study because it is not yet implemented for the dual permeability model, which is used widely for transport calculations.

5.1.3 Equivalent continuum model

In a medium consisting of both fractures and intact matrix rock, the equivalent continuum model is a useful approximation that provides a computationally efficient means of simulating the flow and transport behavior. The limits of applicability for the simulation of water and gas flow in unsaturated rock have been treated by Klavetter and Peters (1986) and Pruess et al. (1990). We suspect that for transport, the time scale of interest for equilibration of concentration between the fracture and matrix fluid is slower than for pressure diffusion, so the equivalent continuum model is less applicable than for hydrologic studies that do not consider transport. Therefore, we have developed both equivalent continuum and dual permeability model capabilities to examine the differences. In the discussion of the site scale model results, we explicitly treat this assumption, examining its validity for various infiltration rates and transport situations.

In FEHM, the formulation of the equivalent continuum model follows that of Pruess et al. (1990). The primary assumption is equilibrium of temperature, fluid pressure, and capillary pressure between the fractures and matrix. The saturated permeability and relative permeability of the medium then become an average between that of the fractures and matrix, weighted by the relative volume fractions of the two media.

5.1.4 Dual permeability model

As implied in the previous section, the equivalent continuum model is only valid if the communication between the fractures and matrix is rapid. For situations in which a difference

exists between the pressure or solute concentration in the two media, the dual permeability model can be used. Figure 5-1 depicts the dual permeability concept. The two media are

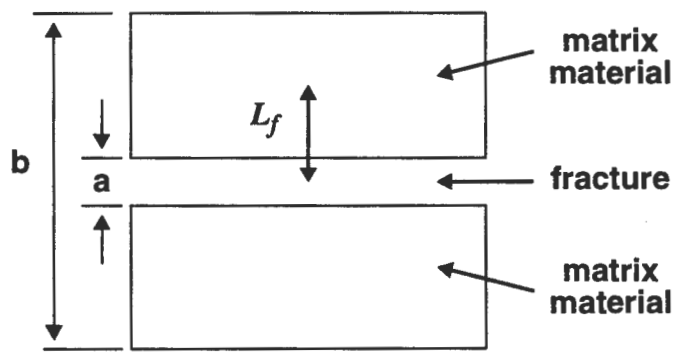

Figure 5-1. Computational volume elements showing dual permeability model parameters.

assumed to be self-contained continua through which fluid can flow. There is also an interaction term to account for communication between the fractures and matrix.

Two parameters characterize a dual permeability system. The first is the volume fraction, V_f, of the fractures in the computational cell (sometimes referred to as the fracture porosity). For the system shown in Figure 5-1, this fraction is a/b. The second parameter is related to the fracture's ability to communicate with the local matrix material. In the literature this parameter takes a variety of forms. The simplest is a length scale, L_f. This quantifies the average distance the matrix material is from the fracture. With just one node in the matrix material the transient behavior in the matrix material can only be modeled in an approximate way. The simple slab model depicted in Figure 5-1 is just one of several different geometric arrangements. Moench (1984) and Warren and Root (1963) list other representations. All of them are similar in the assumption of a local one dimensional connection of the matrix to the fracture.

A volume fraction and length scale are used to characterize the system. The equations for flow and solute transport are formulated for both the fracture and matrix computational grids. One-dimensional versions are created to locally couple the two sets of equations. The length scales are used to modify spatial difference terms and the volume fractions are used to modify the accumulation terms.

The volume fractions for the dual permeability formulation satisfy the following relationship

$$V_f + V_{f1} = 1 \tag{5-22}$$

DRAFT

where V_f is the volume fraction of fractures and V_{f1} is the fraction of the matrix volume. The length scales are partitioned for the fracture and matrix volumes using

$$L_f = L_{f0} V_f$$
$$L_{f1} = L_{f0} V_{f1} \tag{5-23}$$

where L_f is the length scale for the fracture volume, L_{f1} is the length scale of the matrix volume, and L_{f0} is a characteristic length scale.

5.1.5 Rock physical and hydrologic property models

Relative permeabilities and capillary pressures can be strong functions of saturation. Several well known relative permeability functions have been used in the past and are available with FEHM, including simple linear functions, the Corey (1954) relationships, and the van Genuchten (1980) functions. In the present study, the van Genuchten characteristic curve model is used. The van Genuchten relative permeability functions are described by the following formulae:

$$R_l = \begin{cases} \left[1.0 - \left(1.0 - \hat{S}^{\frac{1}{\lambda}}\right)^{\lambda}\right]^2 \sqrt{\hat{S}}, & \hat{S}_l < S_{lmax} \\ 1.0, & \hat{S}_l \geq S_{lmax} \end{cases} \tag{5-24}$$

$$R_v = 1.0 - R_l \tag{5-25}$$

where $\hat{S} = \dfrac{S_l - S_{lr}}{S_{lmax} - S_{lr}}$ and $\lambda = 1 - \dfrac{1}{n}$, where n is an experimentally determined parameter.

R_l and R_v are restricted by the requirement that $0.0 \leq R_l \leq 1.0$ and $0.0 \leq R_v \leq 1.0$. The relative permeability functions are truncated to the appropriate value if these conditions are violated.

The van Genuchten functions (van Genuchten, 1980) for capillary pressure are described by the following equations

$$P_{cap} = \begin{cases} P_{capmax}, & P_{cap1} \geq P_{capmax} \\ P_{cap1}, & P_{cap1} < P_{capmax} \\ 0.0\ , & S_l \geq S_{lmax} \end{cases} \tag{5-26}$$

where $P_{cap1} = P_0\left[\hat{S}^{-\frac{1}{\lambda}} - 1.0\right]^{1.0-\lambda}$, $\hat{S} = \dfrac{S_l - S_{lr}}{S_{lmax} - S_{lr}}$ and $P_0 = \dfrac{1.0}{\alpha_G}$, and $\lambda = 1 - \dfrac{1}{n}$,

where n and α_G are experimentally determined parameters.The van Genuchten capillary pressure curves approach an infinite value as S_l approaches 0, and asymptotically approaches a value of 0 as S_l approaches 1. This requires the use of extrapolation techniques. At low saturations both linear and cubic fits are available. At high saturations a linear fit is used.

5.2 Transport Mathematical Models

The solute transport models in FEHM simulate the movement of tracer solutes traveling in either the liquid or gas phases. A variety of reactive transport capabilities are present in the models. In all cases, solutes are assumed to be present in trace quantities, such that their presence does not impact the fluid properties or the computed flow fields. A related assumption is that any chemical reactions do not enter into the energy balance through endothermic or exothermic reaction terms. For the transport processes considered in the present study, these assumptions are almost certainly valid. Many other specific assumptions are built into the solute transport models related to the nature of the transport and chemical reaction behavior. These assumptions are treated in the sections below.

5.2.1 Finite Element Reactive transport model

This section outlines model equations and assumptions of the finite element reactive transport model of FEHM. Particular attention is paid to the form of the model used in the present study: for information on other model options as well as numerical solution algorithms, see Zyvoloski et al. (1995b) and Viswanathan (1995).

The solute transport equations in the reactive transport model are not directly coupled to the heat and mass transfer system, but use the flow rates and temperatures obtained by the heat and mass transfer solution. The mass flux, $\overline{f_c}$, source (or sink) strength, q_c, and accumulation term, A_c, are defined as follows for a solute:

$$\overline{f_c} = C_v \rho_v \overline{v_v} + C_l \rho_l \overline{v_l}\ , \tag{5-27}$$

DRAFT

$$q_c = C_v q_v + C_l q_l \,, \tag{5-28}$$

$$A_c = \phi(C_v S_v \rho_v + C_l S_l \rho_l) \,. \tag{5-29}$$

The transport equation for a given solute is given by

$$-\bar{\nabla} \cdot (C_v D_{mv} \bar{\nabla} P_v) - \bar{\nabla} \cdot (C_l D_{ml} \bar{\nabla} P_l) - \bar{\nabla} \cdot (D_{cv} \bar{\nabla} C_v) - \bar{\nabla} \cdot (D_{cl} \bar{\nabla} C_l) +$$

$$q_{rxn} + q_c + \frac{\partial}{\partial z} g(C_v D_{mv} \rho_v + C_l D_{ml} \rho_l) + \rho_r \frac{\partial C_R}{\partial t} + \frac{\partial A_c}{\partial t} = 0 \,. \tag{5-30}$$

Here C is the concentration of the solute. The term $\bar{\nabla} \cdot (D_c \bar{\nabla} C)$ is the dispersion term and $\rho_r \frac{\partial C_r}{\partial t}$ is an equilibrium sorption term (see section below for the formulation for sorbing solutes). C_r represents the adsorption of the solute onto the porous media. In addition, the terms q_{rxn} and q_c are source or sink terms due to chemical reaction or fluid sources and sinks, respectively.

Equation (5-30) is a general equation for a solute present in either the liquid or gas phases, or one that partitions between the liquid and gas. The model is capable of simulating any of these possibilities, as well as a solid species, for which only the accumulation and chemical reaction terms are present. Several solutes can be simulated simultaneously, and can interact with one another through the chemical reaction model. The transport terms can be set as a function of position, and there is no requirement that they be the same for all solutes present in a phase.

The next four subsections elaborate on various transport, sorption, and reaction features of the finite element reactive transport model.

Dispersion Coefficients. FEHM uses a standard formulation for the dispersion coefficient, expressed as follows for the x-direction:

$$D_{cl,x} = D_{AB} + \alpha_{dl,x} v_{l,x} \,. \tag{5-31}$$

The Darcy velocity is computed from the solution of the fluid flow equation. The dispersivity α_d and the molecular diffusion coefficient D_{AB} are properties of the medium, the fluid (liquid in the above equation) and the solute. Similar expressions are written for the y- and z-

DRAFT

directions. For the unstructured finite element grids used extensively in the present study, the vector drawn from a node to a connecting node is in general not aligned with the Cartesian axes. For this situation, the mass flux from the node to its neighbor is used to calculate a Darcy velocity, and the following expression is used to compute a direction-weighted dispersivity for any pair of connected nodes:

$$\alpha = \frac{\Delta x^2 \alpha_x + \Delta y^2 \alpha_y + \Delta z^2 \alpha_z}{L^2}, \tag{5-32}$$

where Δx, Δy, and Δz are the distances in the x, y, and z directions between the nodes, L is the distance between the nodes, and the α's are the direction dependent components of the dispersivity. In the present study, we assume that the dispersivity is isotropic since there is no information available to assume an alternative model. Thus Eqn. (5-32) results in a constant value of dispersivity for each nodal connection. Another common formulation of the dispersion coefficient is to align the dispersion with the local direction of flow using a longitudinal and transverse component of the dispersion coefficient, as opposed to aligning the vector with the coordinate axes. FEHM does not yet support this formulation, which would become quite complex for the unstructured grids used to represent the stratigraphy of the hydrogeologic system. Future work will incorporate this alternate dispersion model into the code.

Adsorbing Solutes. The general equilibrium model for adsorption of species onto the rock is given by

$$C_r = \frac{\alpha_1 C_l^{\beta}}{1 + \alpha_2 C_l^{\beta}}. \tag{5-33}$$

The parameters α_1, α_2, and β can be set so as to simulate common isotherms such as the linear (K_d), the Langmuir, or the Freundlich and modified Freundlich models. For ^{237}Np transport, we use only the linear model ($\alpha_2 = 0$, $\beta = 1$) since the data suggest that the isotherm is linear in fluid concentration.

To solve the solute mass balance equation with equilibrium sorption, C_R in Equation (5-30) is computed using Equation (5-33) to determine the mass of solute on the rock for a given fluid-

DRAFT

phase concentration. Thus, C_R is not actually present as a separate unknown in the mass balance.

Henry's Law Species. In contrast to a liquid only or vapor only species, all transport terms of Equation (5-30) are retained (both liquid and vapor) for a Henry's law species. The vapor concentration is related to the liquid concentration assuming the equilibrium Henry's law equation

$$C_v = \frac{M_w K_H C_l}{M_v P_v} \tag{5-34}$$

where M_w is the molecular weight of water, M_v is the molecular weight of the vapor, P_v is the gas pressure, and K_H is the Henry's law coefficient. In FEHM, the temperature dependence of the Henry's Law constant can be formulated using two different expressions. For the dissolution of CO_2 into the liquid phase, an empirical correlation is used to fit data for CO_2 dissolution (Plummer and Busenberg, 1982):

$$K_H = \frac{10.1325\rho_l}{M_w \hat{K}_H} \tag{5-35}$$

where $\hat{K}_H = 10^{\tilde{K}_H}$, and

$$\tilde{K}_H = A_{H,1} + A_{H,2}T + \frac{A_{H,3}}{T} + A_{H,4}\log_{10}T + \frac{A_{H,5}}{T^2} . \tag{5-36}$$

Multiple, Interacting Solutes. Thus far, only the specification of an individual solute has been discussed. In the reactive transport model, chemical reactions involving one or more components can be specified to simulate the chemical interaction of various species. In the present study, this capability is used to simulate the kinetically controlled sorption reactions of ^{237}Np. Chemical reactions are represented with any number of reactions of the following generalized form:

$$a_1B_1 + a_2B_2 + \ldots + a_mB_m = a_{m+1}B_{m+1} + a_{m+2}B_{m+2} + \ldots + a_nB_n \tag{5-37}$$

where the a's are the stoichiometric coefficients and the B's denote each solute present in a particular reaction (i.e., the mth or m+1th species). This relationship is formulated for each reaction being modeled, and a solute may be present in any number of reactions as either a reactant or a product.

The reactions may be specified either as kinetically controlled or equilibrium reactions. For a kinetically controlled reaction, the rate law governing each reversible reaction is specified as follows:

$$\frac{\partial}{\partial t}[B_j] = \pm a_j \left\{ k_{for} \prod_{i=1}^{m} [B_i]^{b_i} - k_{rev} \prod_{i=m+1}^{n} [B_i]^{b_i} \right\} \quad . \tag{5-38}$$

Here the square brackets [ ] denote concentration, the b_i are exponents in the reaction rate or equilibrium equation (specified for every reactant in each reaction), and the forward and reverse reaction rate constants k_{for} and k_{rev} are governed by the Arrhenius equation:

$$k_{for} = A_{for} exp\left(\frac{-E_{for}}{RT}\right). \tag{5-39}$$

In Equation (5-38), the stoichiometric coefficient a_j pre-multiplying the rate law expression is negative if B_j is a reactant, since it is being consumed in the reaction.

For equilibrium reactions, the following relationship is satisfied:

$$K_{eq} = \frac{\prod_{i=m+1}^{n} [B_i]^{b_i}}{\prod_{i=1}^{m} [B_i]^{b_i}} \tag{5-40}$$

where K_{eq} is the equilibrium constant for the reaction. The temperature dependence of K_{eq} can be expressed in two ways, similar to the specification of Henry's law constants above. For the carbonate reactions simulated in the present study, the following form is used:

$$K_{eq} = 10^{\hat{K}_{eq}} \tag{5-41}$$

DRAFT

where

$$\hat{K}_{eq} = A_{rxn,1} + A_{rxn,2}T + \frac{A_{rxn,3}}{T} + A_{rxn,4}\log_{10}T + \frac{A_{rxn,5}}{T^2} \qquad (5\text{-}42)$$

In Equation (5-42), the temperatures are in degrees Kelvin. For additional details on the formulation of the FEHM's reactive transport module, see Zyvoloski et al. (1995b) and Viswanathan (1995).

Solute Sources and Sinks. Solute sources or sinks are handled in a manner analogous to the fluid flow sources and sinks. If there is fluid flow out of the model domain (a fluid sink), the in-place solute concentration is used in the solute mass balance. For fluid entering the system, the solute concentration of the incoming fluid can be specified. Alternatively, the concentration at a node or nodes can be held at a fixed concentration. This boundary condition can be either a source or sink for solute, depending on the gradient in concentration at locations adjacent to the node at which the boundary condition is applied. In the present study, the fixed concentration boundary condition is used to release ^{237}Np and conservative solute from the potential repository.

5.2.2 Particle tracking model

The particle tracking model of FEHM is used as an alternative to the finite element reactive transport model to provide a cost effective transport solution when no complex chemical interactions are required. There is also a matrix diffusion sub-model for which no practical alternative exists in the finite element transport solution. Thus both the ^{237}Np transport and environmental isotope simulations utilize the particle tracking module. This section briefly outlines the model assumptions and formulation: for additional details and model capabilities, as well as a suite of verification and application simulations, see Dash et al. (1995a, b) and Robinson and Henderson (1995).

The particle tracking method developed in FEHM views the fluid flow computational domain as an interconnected network of fluid storage volumes, called cells. In FEHM, a cell is the Voronoi volume associated with a finite element grid point (see Section 4.4.1). The description that follows is applicable for steady state flow fields; the variations in the method for treating transient flow systems are discussed later. The two steps in the particle tracking approach are: 1) determine the time a particle spends in a given cell, and 2) determine which cell the particle travels to next. These two steps are detailed below.

The residence time that a particle spends in a cell is governed by a transfer function describing the probability of the particle spending a given length of time in the cell. Thus, this particle tracking approach is called the "residence time transfer function" (RTTF) method. For a cumulative probability distribution function of particle residence times, the residence time of a particle in a cell is computed by generating a random number between 0 and 1, and determining the corresponding residence time. If a large number of particles pass through the cell, the cumulative residence time distribution (RTD) of particles in the cell will be reproduced.

From the solution of the flow field in a numerical model, the mass of fluid in the computational cell, and the mass flow rate to or from each adjacent cell is obtained. In the simplest case, the residence time of a particle within each cell τ_{part} is given by

$$\tau_{part} = \tau_f = \frac{M_f}{\sum \dot{m}_{out}} \tag{5-43}$$

where M_f is the fluid mass associated with the cell and the summation term in the denominator refers to the outlet mass flow rates from the cell to adjacent cells. In the absence of dispersion or other transport mechanisms, the transfer function is a Heaviside function that is unity at the fluid residence time τ_f, since for this simple case all particles possess this residence time. Equilibrium, linear sorption is included by adjusting the residence time by a retardation factor R_f, so that $\tau_{part} = R_f \tau_f$, where R_f is given by Eqn. (2-1). Once again, in the absence of other transport processes, the transfer function is a Heaviside function.

Before discussing more complex examples of the RTTF method, the method for determining which cell a particle travels to after completing its stay at a given cell is outlined. The assumption that is consistent with the RTTF method is that the probability of traveling to a neighboring cell is proportional to the mass flow rate to that cell. Only outflows are included in this calculation; the probability of traveling to an adjacent node is 0 if flow is from that node to the current node. By generating a uniform random number from zero to one, the decision of which node to travel to is straightforward. Thus the particle tracking algorithm is: 1) compute the residence time of a particle at a cell using the RTTF method; and 2) send the particle to an adjacent cell randomly, with the probability of traveling to a given cell proportional to the mass flow rate to that cell.

DRAFT

The transfer function for transport processes such as dispersion are described now. Within a computational cell, it is assumed that one-dimensional, axial dispersion is valid. The solution to the one dimensional axial dispersion equation is given by Brigham (1974) as

$$\hat{C} = \frac{1}{2}\left[erfc\left(\frac{\sqrt{Pe}(1-\hat{\theta})}{2\sqrt{\hat{\theta}}}\right) + e^{Pe}erfc\left(\frac{\sqrt{Pe}(1+\hat{\theta})}{2\sqrt{\hat{\theta}}}\right)\right] \quad . \qquad (5\text{-}44)$$

where the Peclet number $Pe = vL/D_{eff} = L/\alpha$ and $\hat{\theta} = R_f vt/L = R_f \tau_f$. The use of this solution in the RTTF particle tracking method requires that the transport problem be advection dominated, so that during the time spent in a computational cell, solute would not tend to spread a significant distance away from that cell. Then, the approximate use of a distribution of times within the cell should be adequate. Quantitatively, the criterion for applicability is that the grid Peclet number $Pe_g = \Delta x/\alpha > 1$, where Δx is the characteristic length scale of the computational cell. Note that in contrast to conventional solutions to the advective-dispersion equations, coarse spatial discretization is helpful in satisfying this criterion, as long as the mesh spacing is small enough to provide an accurate flow solution. Highly dispersive transport invalidates the assumptions of the RTTF particle tracking technique. This is not viewed as a severe limitation of the method, since accurate solutions to the advective-dispersion equation are easily obtained by conventional finite difference or finite element techniques for this case. The niche filled by this new technique is in the solution of advection-dominated problems involving the movement of sharp concentration fronts.

For multi-dimensional flow systems, this method for simulating dispersion can be extended for the case of dispersion coefficient values aligned with the coordinate axes. For this case, the flow direction is determined by the vector drawn from the nodal position of the cell the particle traveled from to the current cell, and the dispersivity for this flow direction is given by Equation (5-32). The RTTF particle tracking technique cannot be formulated with a longitudinal and transverse dispersion coefficient model, since the flow rates between cells are defined, rather than the actual flow velocity at a position.

Matrix Diffusion. Matrix diffusion has been recognized as an important transport mechanism for fractured porous media (e.g. Neretnicks, 1980, Robinson, 1994). For many hydrologic flow systems, fluid flow is dominated by fractures, because of the orders of magnitude larger permeabilities in the fractures compared to the surrounding rock matrix. However, even when the fluid in the matrix is completely stagnant, solute can move into the matrix via molecular diffusion, resulting in a physical retardation of solute compared to pure

fracture transport. This effect has recently been demonstrated at the laboratory scale by Reimus (1995), and at the field scale by Maloszewski and Zuber (1985).

To develop a transfer function for matrix diffusion, the representation of the transport system developed in Section 2.3.1 is used. Equation (2-3) represents the transfer function for matrix diffusion in the absence of dispersion in the fracture. The semi-infinite boundary condition between fractures limits the validity of either of these solutions to situations in which the characteristic diffusion distance for the transport problem is small compared to the fracture spacing. However, as long as the solute has insufficient time to diffuse to the centerline between fractures, the solutions provided by Tang et al. (1981) or Starr et al. (1985) are valid to represent the transfer function for the particle tracking technique.

Although in principal a solution of Tang et al. (1981) solution could be used for the transfer function with dispersion and matrix diffusion, its complex form makes it very inconvenient for rapidly computing particle residence times. Instead, a two-step process is used in which the residence time within the fracture is first computed using the transfer function for one-dimensional dispersion in Eqn. (5-44) without sorption. Then, the plug-flow equation with matrix diffusion and sorption (Eqn. (2-3)) is used with the value of the fracture residence time just determined to set the transfer function for the matrix diffusion component of the model. The use of the two-step approach is justified because of the principle of superposition, which allows the decoupling of the dispersive process in the fracture from the diffusive transport in the matrix.

Radioactive decay. Radioactive decay of species such as ^{237}Np and ^{36}Cl can be treated by introducing the decay equation for an irreversible first order reaction:

$$\hat{C} = \exp(-k_{Rn}\tau_{age}) \tag{5-45}$$

where τ_{age} is the particle age since entering the system, and k_{Rn} is the rate constant for radioactive decay, related to the radioactive decay half-life $\tau_{1/2}$ by $k_{Rn} = 0.693/\tau_{1/2}$.

In this model, the concept of a fraction of a particle is used to incorporate radioactive decay into the calculation. The age of a particle, or time since entering the system, is used in Equation (5-45) to compute the fraction of the particles remaining at the current time. When concentration values are computed from the composite behavior of a large number of particles, this method accurately accounts for radioactive decay.

DRAFT

Particle Sources and Sinks. There are two methods for introducing particles into the flow system: 1) inject the particles with the source fluid entering the model domain, or 2) release the particles at a particular node or set of nodes. The first method is used to track injected fluid as it passes through the system. The number of particles entering with the source fluid at each cell is proportional to the source flow rate at that node. The method is the particle tracking equivalent to a constant solute concentration in the source fluid. In the present study, it is used to track infiltrating fluid from a given position at the surface. For method 2, an equal number of particles are released at each node specified, regardless of the source flow rate. This method is used to represent the uptake of ^{237}Np into the liquid that passes through the potential repository. For either option, the model calls for the particles to be released over a specified time interval. The code then computes a starting time for each particle.

For fluid exiting the model domain, the model treats this flow as another outlet flow from the node. The decision of whether the particle leaves the system or travels to an adjacent node is then made on a probabilistic basis, just as though the fluid sink were another connected node. When a particle leaves the system, its passage through the model domain is completed; this fact is recorded as part of the statistics of the simulation.

Transient Flow Fields. For completeness, we now discuss the implementation of the RTTF particle tracking method for a time varying fluid flow system, even though the simulations of the present study assume steady state flow. Consider a numerical simulation in which a discrete time step is taken at time t, and a new fluid flow field is computed. In this model, transient flows are handled by treating the new fluid flow time t_{new} as an intermediate time in the particle tracking calculation when the simulation must stop. The fate of all particles is tracked from time t to time t_{new} assuming that the flow field is constant over this time interval. When the simulation reaches t_{new}, the position of the particle is recorded, along with the fractional time remaining for the particle at the cell, and the randomly generated y-coordinate of the transfer function used for that particle in the cell. When the new fluid flow solution is established, the process continues, but the remaining residence time for a particle is the time determined from the new transfer function times the fractional time remaining in the cell.

Another transient effect that must be considered is that the sum of the outlet mass flow rates $\sum \dot{m}_{out}$ in Equation (5-43) does not necessarily equal the sum of the inlet mass flow rates. When there is net fluid storage in a cell, the particle tracking algorithm uses the sum of the inlet

flow rates in Equation (5-43), whereas Equation (5-43) itself is used when there is net drainage of fluid.

Dual Permeability Formulation. The matrix diffusion transport mechanism developed earlier accounts for the movement of solute into the matrix by molecular diffusion in the absence of advective fluid flow. Dual permeability flow and transport model formulations are also available in FEHM. For this model formulation, the numerical grid is identical for each continuum, so that a one-to-one correspondence exists between a fracture node and the matrix node at that same position. Fluid flow occurs within each continuum, and a transfer term accounts for fluid flow between the fracture and matrix.

Extension of the RTTF particle tracking technique to handle dual permeability systems is very straightforward, since the fracture-matrix flow term is simply an additional inlet or outlet flow rate from the node. In the algorithm, this flow term is treated like flow to any other node, except that when a particle travels from one continuum to the other, the code must now keep track of the fact that the particle has switched. The extension just described accounts only for advective movement of solute between the fracture and matrix. To simulate molecular diffusion as an additional fracture-matrix transport interaction term, the matrix diffusion option must be invoked for the nodes in the fracture continuum. Additional discussion on the validity and limits of applicability of invoking the matrix diffusion model as part of a dual permeability calculation is presented in Section 7.4.2.

6.0 Site Scale Hydrologic Model Results

6.1 Summary of Previous Hydrologic Flow Modeling

The evolution of flow and transport models at Yucca Mountain has been predictably in the sequence from one to three-dimensional simulation models. The one-dimensional models were and are used primarily for performance assessment and include simple stratigraphy (Wilson et al., 1994, Ho, 1994). Early two-dimensional models (Rulon et al., 1986; Wang and Narasimhan, 1987) identified the potential for lateral flow. The earliest three-dimensional site-scale model of Yucca Mountain was created by Birdsell et al. (1990, 1994). It is a finite difference representation with about 31,000 cells. The gravity vector is rotated 6 degrees to account for the dip in the predominate stratigraphic units at Yucca Mountain. In addition, the nominal case of 0.1 mm/y infiltration was assumed to flow through the repository and transport of several radionuclides was simulated. This was the first model to show the importance of three-dimensional effects on radionuclide transport. Gable and Zyvoloski (1994) produced a large structured grid simulation of flow and transport at Yucca Mountain using surfaces derived from the database created at Sandia National Laboratory by Ortiz et al. (1985). The model contained about 63,000 gridblocks and showed a large lateral flow due to hydrostratigraphy. Rockhold et. al (1990) developed a repository-scale three-dimensional model and concluded that lateral flow occurred and that the complex stratigraphy was important. Wittwer et al. (1995) have produced a coarse resolution, three-dimensional site-scale model of about 5000 integrated finite difference cells. This model, using the simulation code TOUGH2 (Pruess, 1990), was a joint effort between Lawrence Berkeley Laboratory and the USGS. The report shows results using the nominal infiltration rate of 0.1 mm/y distributed uniformly over the surface of the study area as well as the case of no infiltration on the surface except over the major fault zones to demonstrate the vertical and lateral dispersion for moisture flux. The report contained some interesting work on flow around faults as end-member cases of either very high or very low permeabilities in the faults were considered. In the present study, this three-dimensional model is referred to as the LBL/USGS model. An improved version of this model is under development (Bo Bodvarsson, personal communication, 1995). The site scale modeling at Yucca Mountain has established the importance of heterogeneity, fracture flow, fault flow, stratigraphic characterization, and infiltration in understanding the flow system at Yucca Mountain.

6.2 Benchmarking the Los Alamos and LBL/USGS Flow Models

The Los Alamos model differs from the LBL/USGS model primarily in grid geometry and fault representation. The LBL/USGS grid was developed using the following criteria (after Wittwer et al., 1995):

- Existing Borehole locations at centers of grid blocks.

- Incorporation of major faults into the grid.
- Incorporation of spatially distributed infiltration.
- Incorporation of outcrops.
- Gradual changes in element size to minimize model inaccuracies.
- The Los Alamos modeling effort was motivated somewhat differently:
- Automatic generation of grids to incorporate a variety of arbitrary resolution Yucca Mountain Project databases.
- Ensure maximum geometric flexibility in order to resolve outcrops and stratigraphic layer pinch-outs.
- Efficiently provide changes to the grid resolution in horizontal and vertical dimensions.
- Ensure Delaunay and Voronoi conditions to guarantee convergence while minimizing grid orientation effects.
- Implement a method to allow for simple, automatic incorporation and change of repository and ESF to quickly accommodate changes to repository design.
- Provide a flow solution to be coupled with site scale solute transport calculations.
- Provide a natural link to saturated zone site scale grid.

We believe the different philosophies both aim at the same final result, a defensible model. A defensible model must incorporate the most recent fluid and rock properties and analyses, correct hydrostratigraphy, and an accurate numerical solution. The last item means appropriate computational grid resolutions must be supplied to match the study problem. The appropriate resolution is problem dependent. For example, accurate resolution of a propagating solute front may require substantially greater resolution than the resolution required to compute accurately the flow field.

Figure 6-1 shows a plan view of the Los Alamos site-scale computational grid used in comparison with the USGS/LBL model. This grid is compared with Figure 7 in Wittwer et al. (1995) (note, however, substantially higher resolution grids are used for other flow and transport calculations in this report). The first noticeable difference in the two models is the regularity of the Los Alamos model grid spacing in plan view. The LBL/USGS grid has been oriented to represent fault trends. The Los Alamos model is designed to match hydrostratigraphic surfaces which are output from the Stratamodel framework model and visualization package. This interface was described in more detail in Section 4.3. The surfaces that were input to the framework model were those obtained from the LBL/USGS model.

The character of the grids are reversed when viewed in the vertical planes as shown in Figure 6-2 of this report and Figure 22 in Wittwer et al. (1995). Examination of these figures illustrates a difference in grid construction. The USGS/LBL model has quadrilateral cell faces whereas the Los Alamos model has triangular faces. The larger number of connections per node in the unstructured tetrahedral grids used by Los Alamos reduces grid orientation numerical effects. In comparison, the USGS/LBL grids are limited to vertical connections between layers. The primary unintended

DRAFT

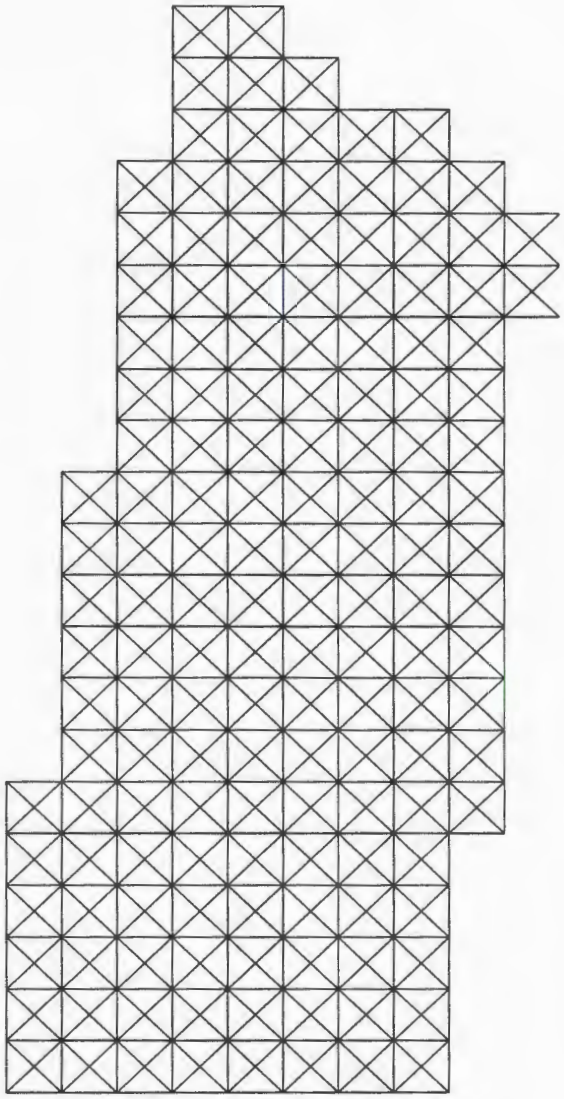

Figure 6-1. Plan view of coarse Los Alamos site scale computational grid used in comparison with USGS/LBL model.

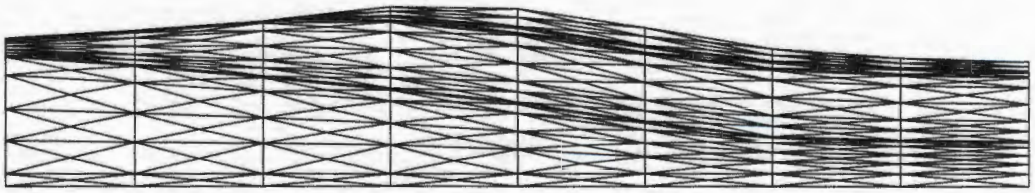

West **East**

Figure 6-2. 2-D east-west cross-section of south face of coarse Los Alamos site scale computational grid used in comparison with USGS/LBL model.

DRAFT

consequence of grid orientation errors is that fluid preferentially flows along grid lines. The details of each grid is summarized in Table 6-1. To put these numbers in perspective, a three-dimensional finite difference code on a structured grid with a standard seven point stencil averages about 3 connections per node when edges and corners are included.

Table 6-1. Grid Comparison of LBL/USGS and Los Alamos Models

	Nodes	Connections	Reference
LBL/USGS	5148	~20000	Wittwer et al. (1995)
Los Alamos	14150	99073	This document

The rock properties and hydrologic flow parameters used in the Los Alamos model were obtained from Wittwer et al. (1995), except where indicated (shown in Table 6-3 at end of Section 6.8). The boundary conditions include a uniform infiltration rate of 0.1 mm/y, no flow on all side boundaries and high liquid saturation (at least 0.95) on the bottom boundary.

The comparison of the LBL/USGS and Los Alamos site-scale models is made from saturation data that was provided by scientists from LBL. Saturations at x,y,z locations were provided, but node connectivity information was not. Therefore, the LBL/USGS saturation solution is mapped onto the Los Alamos grid for comparison purposes. Then, three two-dimensional cross sections are compared. Figure 6-3 shows three east-west cross sections with the saturation differences displayed on the Los Alamos grid. There are several obvious areas of disagreement. These are along the top boundary and at the fault zones. The top boundary may be a function of the method LBL uses to process output files. Figures 22-25 in Wittwer et al. (1995) show a boundary at the top of the grid with no color. This may be a function of the cell centered grid used in the LBL code TOUGH2. Thus we believe this area of "disagreement" actually does not exist. The fault zones show differences because of the high permeability applied to these zones in the LBL/USGS model. These regions were treated as possessing the same properties as the surrounding medium in our comparison calculations, although in the actual model analyses presented later we investigate the impact of different hydrologic properties for the Ghost Dance fault. We note that studies with low permeabilities would have shown large differences in the opposite direction. With these areas removed from consideration, The solutions matched reasonably well. We conclude from this comparison that the match of the flow solution between the LBL/USGS model and the Los Alamos model is good. Other studies (Reeves et al., 1993, Dash et al., 1995b) have shown that the LBL code TOUGH2 and the Los Alamos code FEHM produce the same results on a variety of isothermal and nonisothermal problems.

DRAFT

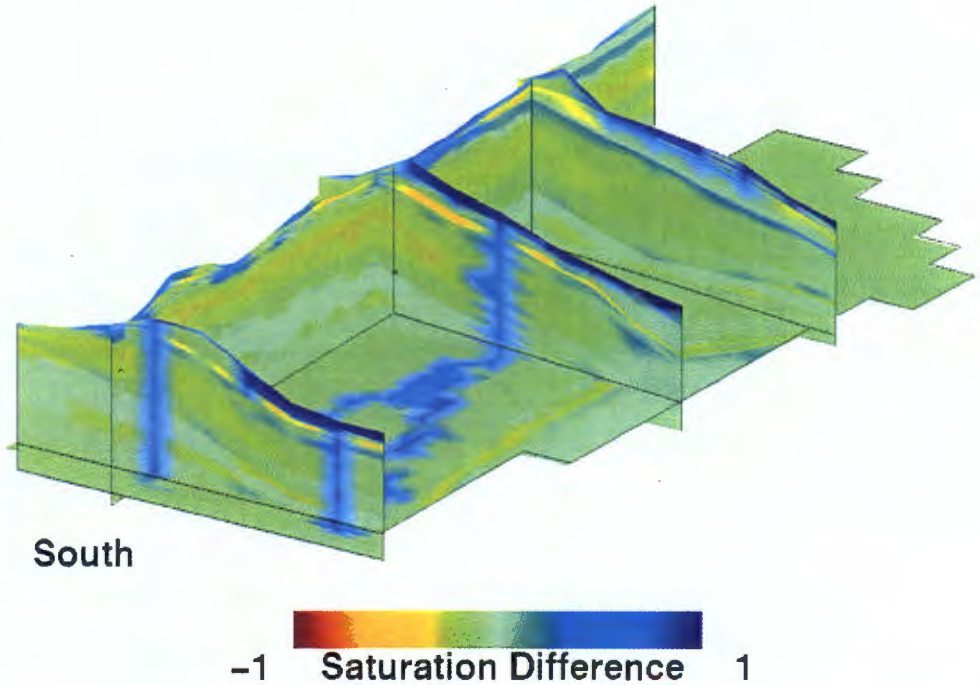

Figure 6-3. Comparison of saturations between LBL/USGS solution and Los Alamos solution. Figure shows difference in saturations between the two simulations. A positive value indicates the Los Alamos model has a larger saturation at that location.

6.3 Rationale for the Development of Hydrologic Solutions

The LBL/USGS site scale flow model has provided valuable insights into the important flow processes at Yucca Mountain. Now that the Los Alamos and LBL/USGS models have been compared, the Los Alamos model will be used in the calculations of the present study. This decision was made for the following reasons:

- The Los Alamos flow model is used directly with the Los Alamos transport model. Mapping a TOUGH2 flow solution into Los Alamos transport modeling code would be difficult, and, as shown in the previous section, not necessary.
- For model calibration, we believe that it is not sufficient to compare only saturations because small changes in saturation can cause large changes in fluid velocities. Transport modeling of naturally occurring isotopes should be used in the calibration process.
- High resolution models are needed for both the flow and transport solutions. Mapping a low resolution flow simulation onto a finer resolution grid would be inaccurate. FEHM can handle the fine resolution calculations without undue computational burden.
- The flexible, automatic, grid generation package, GEOMESH, is intimately linked with FEHM.
- Equivalent continuum and dual permeability flow and transport options are available in FEHM.
- Consistent two-dimensional and sub-scale three-dimensional grids are easily obtained from GEOMESH.

- The QA qualification of the FEHM code is very nearly complete.
- The FEHM code has memory management, which allows the memory requirements for each problem to be adjusted on input, allowing many jobs to be run simultaneously.

6.4 Current Hydrologic Model Results

Two- and three-dimensional flow simulations were performed to serve as input to the radionuclide migration studies. In each case, the flow solutions were run until a steady-state flow field was achieved. Differences in the flow fields are due to different infiltration rates (constant over time) and different characterization of the stratigraphy of the Calico Hills. In this section, the flow field is computed for the modified Calico Hills representation described in Section 4.2.4 and for infiltration rates of 0.1, 1, and 4 mm/y distributed uniformly over the surface, and for a nonuniform infiltration map based on the work of Hudson and Flint (1995). The uniform infiltration rate of 0.1 mm/y was chosen as the nominal case because that is the value used for the site scale flow model of Wittwer et al. (1995). We then increased it by an order of magnitude and then again by a factor of 4, in keeping with indications that infiltration may be much greater than 0.1 mm/y.

For each of the stratigraphic models considered here, a stratigraphic framework model exists. The three-dimensional grid incorporates all of the information from the stratigraphic framework model while the two-dimensional models are based on grids computed from cross sections of the stratigraphic framework model. The parameters characterizing matrix and fracture properties of each of the units in the stratigraphic framework model are listed in Table 6-3. Fracture characteristic curve parameters have not been measured, so we adopt the concept of a threshold saturation similar to that of Wittwer et al. (1995) to set these parameters. In our case, the code calls for van Genuchten parameters for the fractures. The parameter α_G was adjusted for each of the four major hydrostratigraphic units to a value such that in an equivalent continuum formulation, the fracture permeability begins to become a significant fraction of the total permeability at a matrix saturation of 0.99. For the dual permeability simulations fracture spacing is also required as input to FEHM. The values used for the fracture spacing in the PTn, TCw, TSw, and CHn, are 0.618 m, 2.22 m, 0.74m, and 1.62 m, respectively (Wilson et al., 1994).

The fracture and matrix properties we use in the modified Calico Hills representation are different than those cited for the Calico Hills in Wittwer et al. (1995). The matrix permeability values for the vitrified, devitrified, and zeolitized subunits come from Loeven (1993) who found significantly lower values than reported by Montazer and Wilson (1984). Of particular interest is the difference in fracture permeabilities. We use the Calico Hills saturated zone aquifer test values from Loeven (1993) to represent the fracture permeabilities. For all other units, we use the fracture permeability values from Wittwer et al. (1995) to maintain consistency until more information is available. The matrix and

fracture properties used in USGS/LBL model comparison as well as all simulations with the modified Calico Hills are given in Table 6-3.

A large number of the transport sensitivity analyses performed in this report are done on two-dimensional cross sections. This is due to the time and cost constraints of performing the number of simulations required for such an analysis. The cross section locations relative to the site scale model are shown in Figure 4-3.

6.5 Two-Dimensional Cross Section Simulations

6.5.1 Saturation Fields

Figure 6-4 shows the simulated saturations for the east-west cross section (Antler Ridge) for the uniform infiltration rates of 0.1, 1.0, and 4.0 mm/y, respectively, for the equivalent continuum method. Likewise, Figure 6-5 shows the resulting matrix saturations for the same uniform infiltration rates when the dual permeability model formulation is used on the Antler Ridge cross section. These saturation fields are computed using the matrix and fracture parameters presented in Table 6-3. In all of these saturation fields certain expected characteristics are demonstrated. First, the high permeability units of the Paintbrush and Calico Hills nonwelded tuffs demonstrated the lowest saturations. The highest saturations are found in the welded units of the Topopah Springs and the Tiva Canyon.

6.5.2 Comparisons

In comparing the matrix saturations computed with the dual permeability model and the equivalent continuum model, one sees that the major characteristics of the saturation distributions are similar, with the regions of high and low saturations closely paralleling the hydrogeologic units. The saturations in the majority of the TSw units are somewhat higher in the equivalent continuum model, and the saturation as a function of depth in the TCw units increase in the dual permeability model down to the contact between the TCw and PTn units. Although these differences are subtle, they are both suggestive of a fundamental difference in the two flow models. Figure 6-6 shows the fluid saturations in the fractures for the dual permeability model for 0.1 mm/y infiltration. Note the build-up in saturations in the fractures in the very thin TCw unit immediately adjacent to the underlying PTn units. In contrast to the equivalent continuum model, in the dual permeability model there emerges a very strong capillary barrier effect that prevents some of the infiltrating fluid from entering the PTn, even at the relatively low infiltration rate of 0.1 mm/y. Fluid instead travels laterally at the base of the TCw before moving downward in the Eastern portion of the model domain. Since the effective infiltration rate through the TSw is lower in the dual permeability model, matrix fluid saturations are lower.

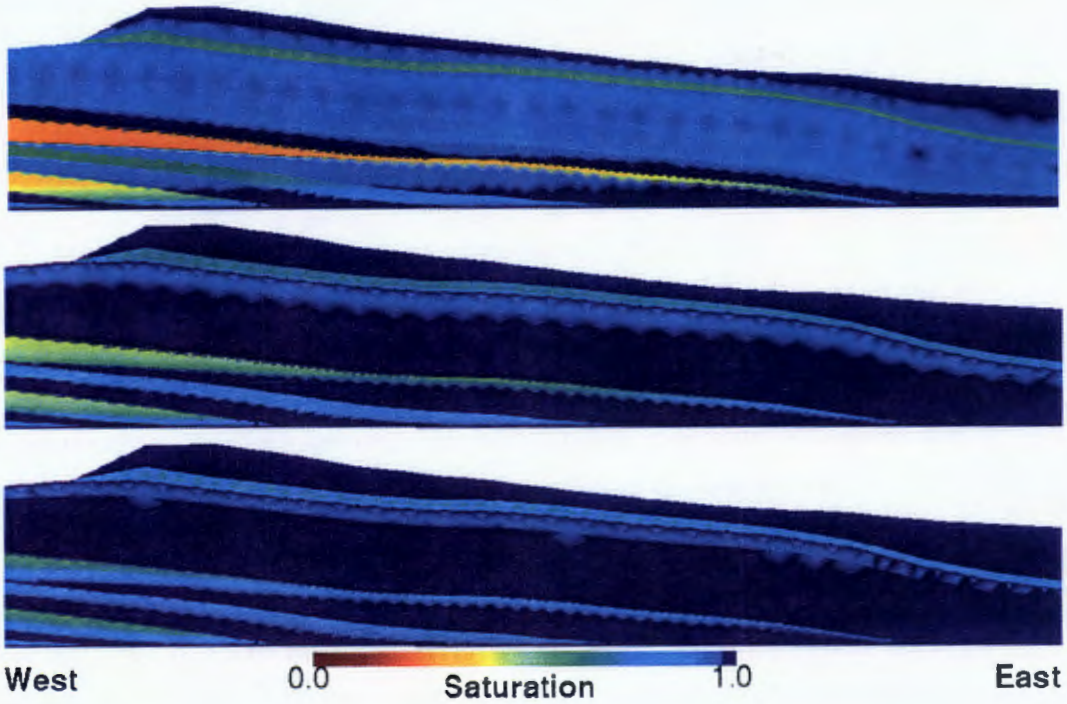

Figure 6-4. Antler Ridge cross section saturations for a) 0.1 mm/y, b) 1.0 mm/y, and c) 4.0 mm/y infiltration rate; Equivalent continuum formulation.

DRAFT

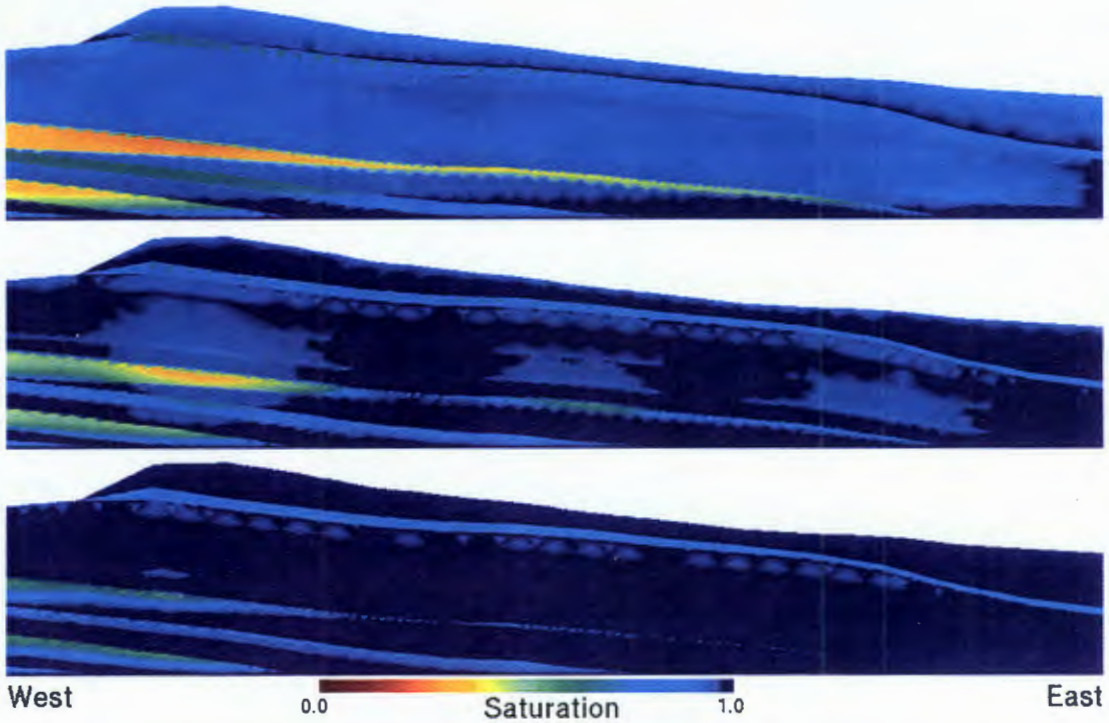

Figure 6-5. Antler Ridge cross section saturations for a) 0.1 mm/y, b) 1.0 mm/y, and c) 4.0 mm/y infiltration rate; Dual permeability formulation.

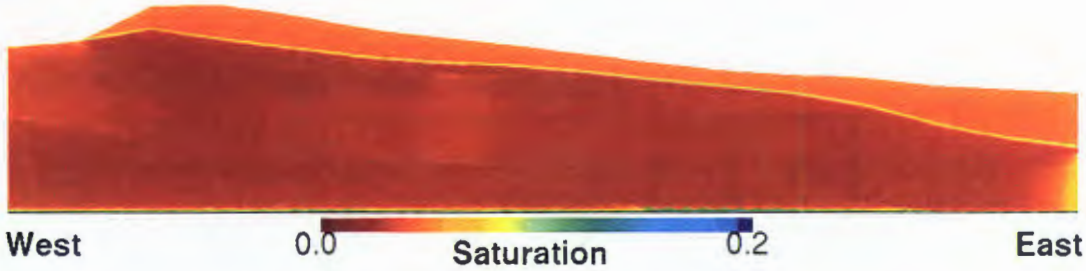

Figure 6-6. Fracture saturations for 0.1 mm/y infiltration rate; Dual permeability formulation.

Using the particle tracking model, we now trace the movement of fluid entering at the surface for the two flow models to confirm the conclusions just reached and to examine the details of the flow systems. These simulations are also represented in the movie that accompanies this report at a level of detail that is impossible to depict in a single figure. The

reader is referred to this movie to obtain a more comprehensive understanding of the fluid flow paths. Particles are injected at two positions at the surface and tracked through the model domain for which the infiltration rate is 0.1 mm/y. Advective movement with no dispersion or matrix diffusion is assumed. Figures 6-7 and 6-8 show the particle concentrations at various times for the equivalent continuum and dual permeability models, respectively. The same number of particles are injected in each case, and the logarithmic color bar is designed to accent depict the extent of solute spreading. The equivalent continuum model exhibits essentially one-dimensional, vertical flow at this infiltration rate, whereas the lateral flow at the TCw-PTn contact is apparent in the dual permeability model simulation.

Of course, the fluid traveling laterally must eventually travel downward and exit at the water table, either at the no-flow right hand boundary or elsewhere inside the model domain where lateral flow is inhibited. The particle tracking simulation indicates that this downward flow occurs primarily in two places: the rightmost boundary of the model domain and through the middle of the model. The flow path through the middle of the model corresponds to the Ghost Dance fault. Even though the fault is not explicitly embedded in this model, the representation of the stratigraphy reflects the presence of the fault offset, manifesting itself as a region of flattening of the Eastward dip of the units. In the region around the fault where there is little or no dip, gravitational forces are large enough to allow some of the lateral flow to travel downward near the fault. Thus, although the fault is not explicitly considered, its effect is felt in the flow and transport simulations in dual permeability.

The differences in the fundamental flow regime for the two models implies that we need to assess the impact on transport calculations. Regarding the question of which model is "correct," the dual permeability model is an appealing alternative to the equivalent continuum model formulation typically used because of its relaxation of the assumption of equal capillary pressures in the fractures and matrix. Thus, fracture flow is induced in some instances for which it would not be possible in the equivalent continuum model. Furthermore, the implications on transport of a model that contains fracture flow paths is profound. Although future studies should examine the differences in the models in more detail, it seems likely that dual permeability calculations should become a more standard option to be used in flow and transport model calculations. In the present study, we retain the equivalent continuum model as one model formulation while examining the sensitivity of the predictions to the choice of model formulation.

6.5.3 Fracture-Matrix Interaction Effects

A key uncertainty in the hydrologic behavior of the unsaturated zone that impacts the results of transport calculations is the nature of the fracture-matrix interaction term. In most of the

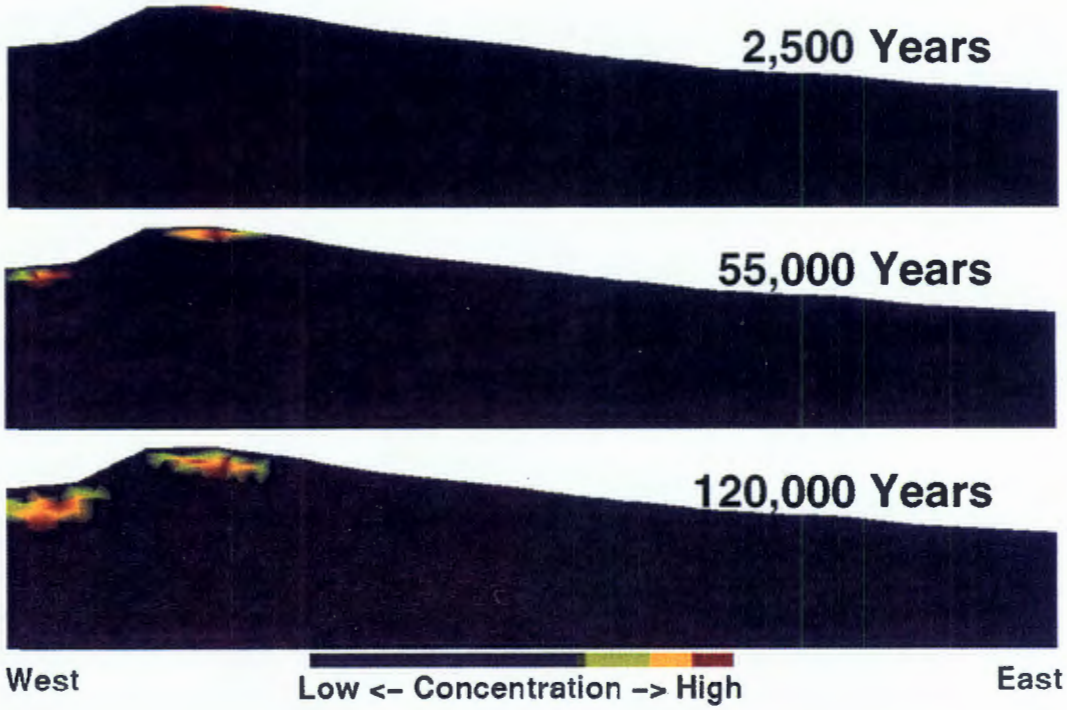

Figure 6-7. Particle concentrations at times of 2500 y, 55,000 y, and 120,000 y for the equivalent continuum model with 0.1 mm/y infiltration.

DRAFT

hydrologic modeling carried out on the Project, the nature of the capillary pressure characteristic curves of the fractures and matrix are such that the fractures become saturated enough to support flow only when the matrix is nearly fully saturated. However, the nature of the fracture-matrix interaction term is very uncertain, given that laboratory scale tests typically are performed on samples without fractures, and field scale unsaturated zone tests, those likely to exhibit the greatest effects of the fracture-matrix flow term, have not been carried out. The assignment of fracture van Genuchten parameters, specifically the α_G term in Eqn. (5-26), are based solely on theoretical grounds, such as the analysis of Wang (1992) based on fracture aperture distribution. In this section, we ask the question: what if previous representations of the fracture capillary pressure characteristic curve are incorrect, and the fractures actually possess a characteristic curve more like the intact rock? Then, fractures are likely to flow at much lower matrix rock saturations, and the resulting saturation distributions and transport behavior will be different.

In this set of dual permeability, two-dimensional simulations, the α_G term for the fractures in each unit are set to 0.1 m^{-1}, compared to values ranging from 0.5 to 10 m^{-1}, adjusted by unit to achieve an equivalent continuum matrix saturation of about 0.99 at which fractures begin to contribute significantly to the overall permeability. Using a value of 0.1 m^{-1} everywhere should result in fractures that flow at significantly lower matrix saturations. Figure 6-9 compares the saturation profiles for three cases: 0.1 mm/y, base case hydrologic properties; 4 mm/y, base case hydrologic properties; and 4 mm/y, fracture hydrologic properties adjusted to allow fractures to flow at lower matrix saturations. Note that the saturation distribution for the simulation with adjusted properties actually resembles the 0.1 mm/y case more closely than the 4 mm/y case with base case properties. This comparison shows that by changing certain parameter values for which values are quite uncertain, we can obtain similar saturation profiles despite an increase of a factor of 40 in infiltration rate. Clearly, focusing only on moisture distribution is non-unique.

6.5.4 Faults

The impact of the presence of the Ghost Dance fault on the saturation distribution was studied by Wittwer et al. (1995) using the LBL/USGS site scale model. They showed that when the fault zone is modeled as a low permeability zone, it acts as a barrier to flow, whereas with high permeability properties, the fault acts as a drain for fluid. Depending on the permeability and characteristic curves assigned for the rock in the fault zone, the fault can be a region of either low or high saturation. Current site investigations are examining the faults to determine their hydrologic characteristics.

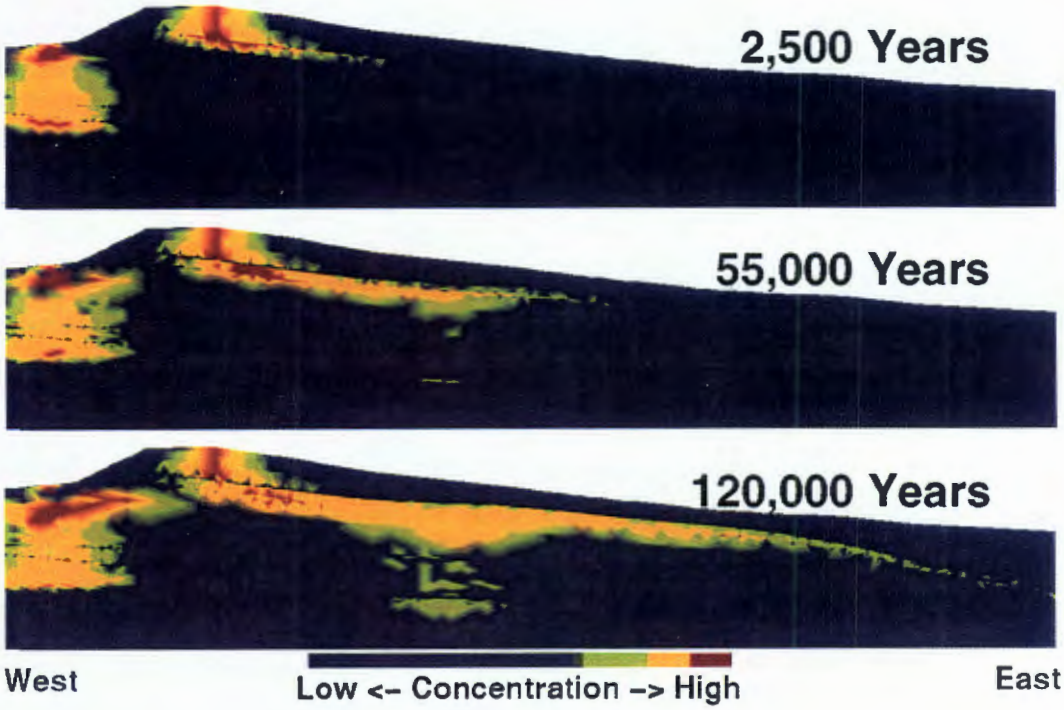

Figure 6-8. Particle concentrations at times of 2500 y, 55,000 y, and 120,000 y for the dual permeability model with 0.1 mm/y infiltration.

DRAFT

In the present study, we use the two-dimensional, 8000 node Antler Ridge cross section to examine the potential role of the Ghost Dance fault on the flow and transport system. Since this grid is finely resolved in the East-West direction, it was possible to define a vertical zone of rock in the position defined by the Ghost Dance fault that captured several grid points across the zone yet was still only approximately 130 m in width. Alternatively, the fault could be built into the grid to resolve the geometry of this region in greater detail, but for this initial calculation the approach taken here is adequate. Recall that the offset of the fault is manifested in the hydrostratigraphic representation of the system, albeit in a smoothed way. Including the fault explicitly in this way results in a hydrologic system with both offset at the fault and a thin region of distinct hydrologic properties.

The most likely impact of a fault is to divert lateral flow. Therefore, the dual permeability model is used in these simulations since it was determined earlier that lateral flow was much more prevalent in two dimensions using the dual permeability formulation. In this set of calculations, the hydrologic properties of the Ghost Dance fault are represented using the fracture properties of the TSw units (the most highly fractured units in the model), while the matrix properties are assigned values of the vitric Calico Hills units. In summary, the fault is modeled as a zone of rock 130 m thick, extending from the surface to the water table, with relatively high fracture permeability and properties of the surrounding matrix resembling one of the more permeable hydrogeologic units of the unsaturated zone. The saturation distributions in the fractures and matrix rock for a uniform infiltration rate of 1 mm/y are shown in Figure 6-10. Note the lower matrix saturations at the fault zone due to the hydrologic property values assigned for the fault. As in the case with no fault present, the fracture saturations exhibit the buildup at the base of the TCw unit, indicative of lateral flow there. The fracture saturations are also higher than average due West of the fault zone because the properties of the fault are such that some flow is prevented from entering the fault, flowing instead in the rock immediately adjacent to it. Thus some water enters the fault and flows rapidly downward while some builds up in the matrix and fractures to the west of the fault. These results are qualitatively in agreement of the work of Wittwer et al. (1995). The flow paths taken by infiltrating fluid are shown in the particle tracking calculations of Figure 6-11. Compared to the dual permeability results without the fault explicitly represented (Figure 6-8), the impact of the fault is evident.

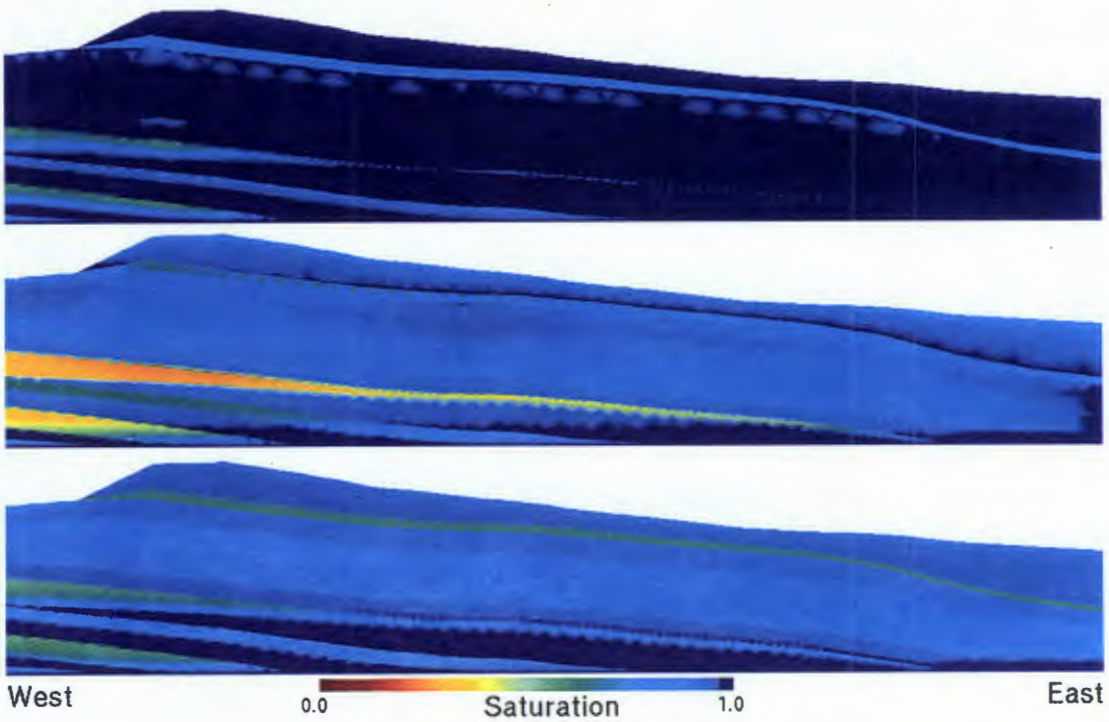

Figure 6-9. Comparison of matrix saturations for different infiltration rates and α_G values. a) infiltration = 4 mm/y, base case properties, b) infiltration = 0.1 mm/y, base case properties, c) infiltration = 4 mm/y, α_G = 0.1 m^{-1}.

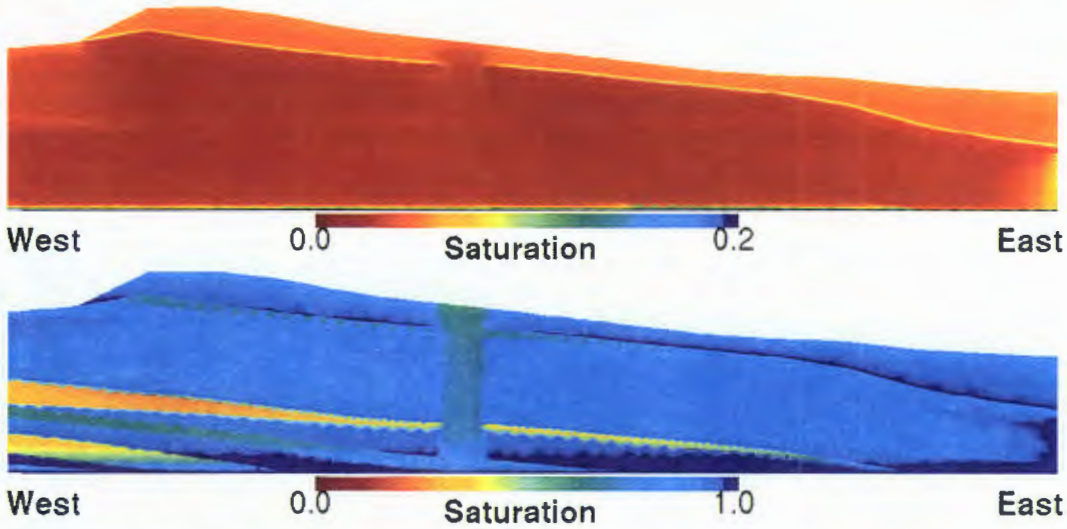

Figure 6-10. Saturation distributions in the fractures and the matrix rock for the case of the Ghost Dance Fault explicitly modeled. Top figure: fracture saturations; Bottom figure: matrix saturations.

DRAFT

Finally, as part of the investigation of the effect flow in the fault may have on transport, a simulation is performed using the dual permeability formulation in which the infiltration is increased over the fault zone by a factor of four. For this scenario, the infiltrations are 0.4 mm/y over the fault and 0.1 mm/y over the other surface area. A constant ^{36}Cl tracer concentration is injected at all points on the surface and the flow path is observed in Figure 6-12. This figure (top) shows first that even without the fault explicitly specified with unique properties and without increased infiltration, there is an increase in vertical flow in the fault region due to the changes in stratigraphic dip of the beds crossing the fault. Next, when unique fault properties are specified (in this case, high matrix permeability and high fracture density) and increased infiltration is prescribed over the fault, the increased flow in the fault does not serve to increase lateral flow in the subsurface units significantly. Rather, it functions merely as a fast conduit for the infiltrating water. In fact, some infiltrating water that would normally move into the region of the fault and then down dip to the east is channeled vertically, thereby missing the potential repository. In Figure 6-12, the increased normalized concentration indicates younger water. One sees in the figure, that even for the case of increased infiltration over the fault, the matrix water is older under the eastern section of the potential repository, for this set of model parameters.

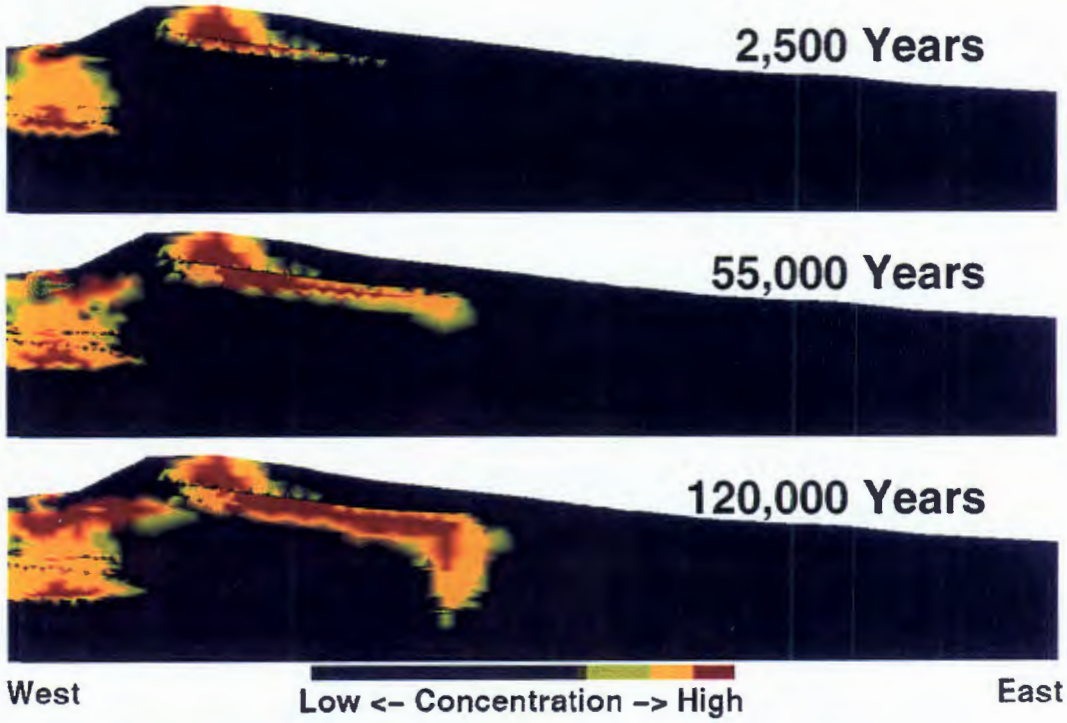

Figure 6-11.Particle concentrations at times of 2500 y, 55,000 y, and 120,000 y for the dual permeability model with 0.1 mm/y infiltration, fault explicitly represented.

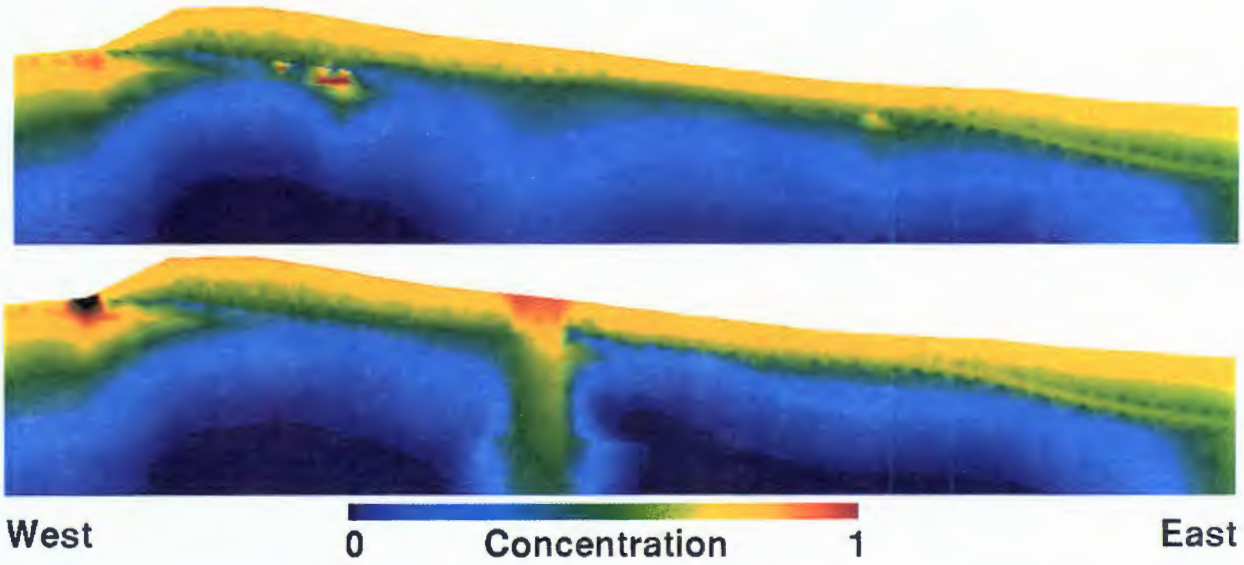

Figure 6-12.Normalized Chlorine-36 concentrations in infiltrating water. Top figure is for uniform infiltration of 0.1 mm/yr and no uniquely specified fault properties. Lower figure has increased infiltration of 0.4 mm/yr over fault region.

DRAFT

6.6 Three-Dimensional Simulations

6.6.1 Equivalent Continuum Model

The three-dimensional grid used for most of the three-dimensional site-scale flow and transport models is shown in Figure 6-13. The grid describes 21 separate regions including the repository and the zeolitic zones of the Calico Hills. A coarse grid of 13,491 nodes and 78,463 elements (used in dual permeability simulations, but not shown in the figure) was used to represent Yucca Mountain on 250 meter centers. To depict Yucca Mountain on 125 meter centers, as shown in Figure 6-13, 51,550 nodes and 312,465 tetrahedral elements were used. The mesh contained 369,810 connections. Figure 6-14 shows an exploded view of the hydrologic units for the finer grid at twenty times vertical exaggeration. Note the numerous pinchouts in the units below the repository. The pinchouts account for much of the complexity in the mesh, though, on average, there are only eight connections per node, about average for a finite element code in three dimensions. The two-part repository shown in the figure is not necessary for the flow solution but is important for transport simulations and in future studies for repository heat load simulations. The hydrologic parameters used in the model are given in Table 6-3. These values are the same as those in the LBL/USGS model with the exception of the zeolitic units, which were representative values from the catalog of hydrologic properties compiled by Loeven (1993). They are also identical to those used in the two-dimensional simulations described above.

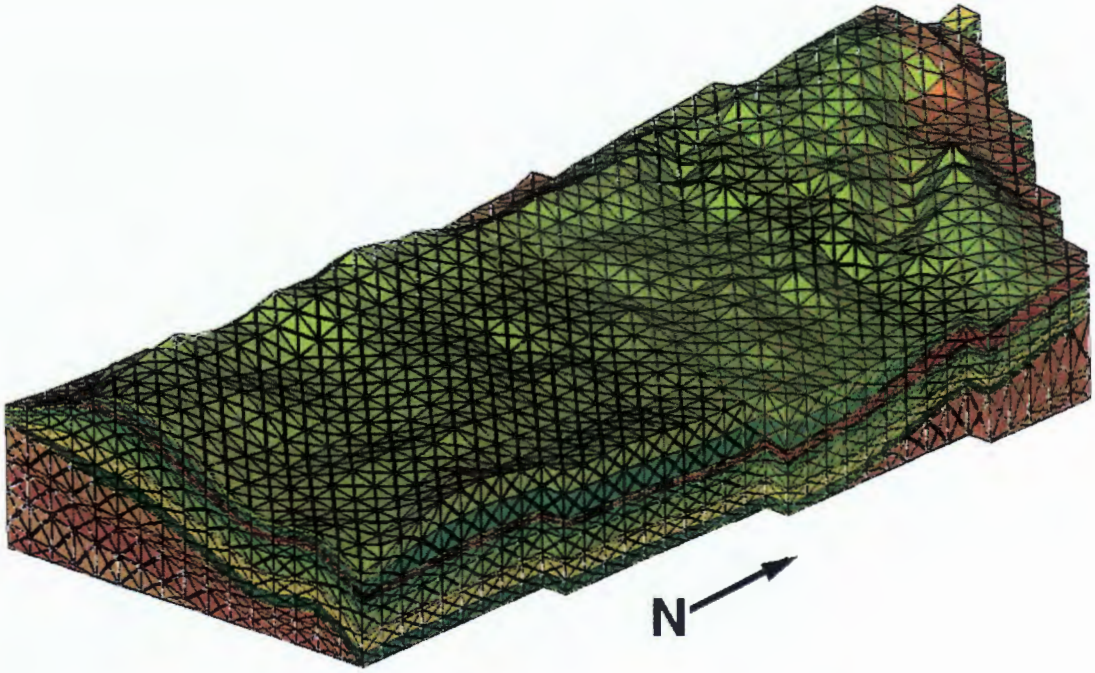

Figure 6-13.Three-dimensional grid used in site scale flow and transport models at three times vertical exaggeration.

DRAFT

The infiltration rates considered first are 0.1 mm/y and 1 mm/y. The saturation fields computed for the infiltration rate of 0.1 mm/y is shown in Figure 6-15. In both the low and higher resolution models, the saturation generally follows the stratigraphy except that there is a saturation buildup on the East and South boundaries. The saturation buildup at these boundaries is an indication of enhanced downward flux, the result of lateral flow from the West and North. The 1 mm/y saturation results, shown in Figure 6-16, show trends similar to the 0.1 mm/yr. However, the fence diagrams show a much higher saturation in the Northeast in the units below the Paintbrush Tuff. This will impact fluid travel time in that region.

As a first indication of how infiltrating water moves in the 1 mm/y infiltration problem, a set of particles were introduced at the surface in the Northwest and their travel paths were observed. Indicating the true three-dimensionality of the system, the particles traveled in a southeastern direction. Further, they stayed near the surface for a substantial portion of their travel before moving downward. Figure 6-17 shows the isoconcentration surface defining the extent of the plume in this simulation.

6.6.2 Three-Dimensional Dual Permeability Model

We have also run dual permeability flow and transport simulations of the site scale model because of the importance of fractures in transport. To date, we have computed three-dimensional, dual permeability solutions on the 13,491 node grid. The data needed for the dual permeability runs consists of that required for the equivalent continuum model, as well as fracture spacing data. The spacing data were obtained from Wilson et al. (1994) and are presented in Table 6-3. Infiltration rates of 0.1 mm/y and 1 mm/y were run to obtain steady state flow fields. The saturation distributions in the fractures and matrix are displayed in Figures 6-18 and 6-19 for the 1 mm/y infiltration rate. A noticeable difference between the dual permeability matrix solution and the equivalent continuum solution given in Figure 6-16 are the lower matrix saturations on the top of Yucca Mountain. Other features such as the saturation buildup in the East and the South are evident in both models.

One important phenomenon that is more likely to occur in dual permeability models than in equivalent continuum models is the development of capillary barriers near the boundaries of regions of contrasting hydrologic properties. This process is important as it serves to drive lateral flow. In Figure 6-19, note the very thin zone of high fracture saturation in the East-West transect, similar to that in the two-dimensional simulations (Figure 6-6). The significance of that high fracture saturation will be demonstrated in the solute transport sensitivity analysis.

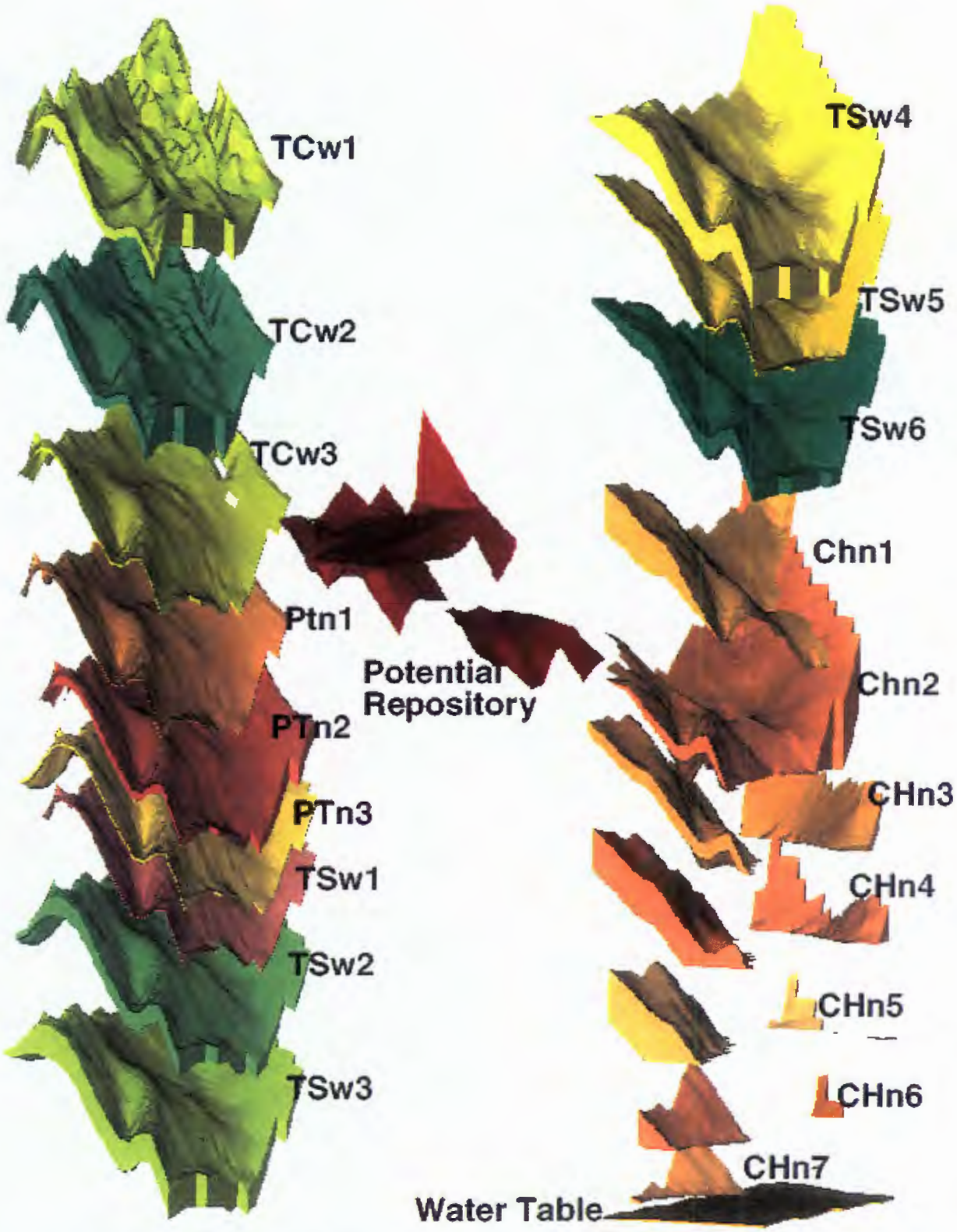

Figure 6-14.Exploded view of stratigraphic units in three-dimensional model at ten times vertical exaggeration.

DRAFT

6.7 Chlorine-36 Simulations

The difficulty and uncertainty associated with calibrating a hydrologic flow model to saturations alone leads us to believe that other information relating to infiltration strength and flow pathways must be considered in these modeling exercises. Such information can serve to help identify what component of the shallow infiltration estimated by Hudson and Flint (1995) continues downward as deep percolation and eventually groundwater recharge. The most accessible information regarding flow pathways of infiltrating water is provided by the naturally occurring isotopes discussed in Section 3.4. Our first example demonstrating how naturally occurring isotopic data can be used in model calibration and validation involves simulations of the movement of ^{36}Cl into the unsaturated zone over the past forty years. We are particularly interested in the high concentrations of atmospheric ^{36}Cl which were produced during atmospheric nuclear testing in the 1950's and early 1960's (the so-called "bomb pulse"). The chloride then entered the subsurface with rainfall and began migrating through the unsaturated zone. The signal is strong enough (Liu et al. 1995) that in the shallow zone the elevated levels of ^{36}Cl is usually an unambiguous indicator of young water.

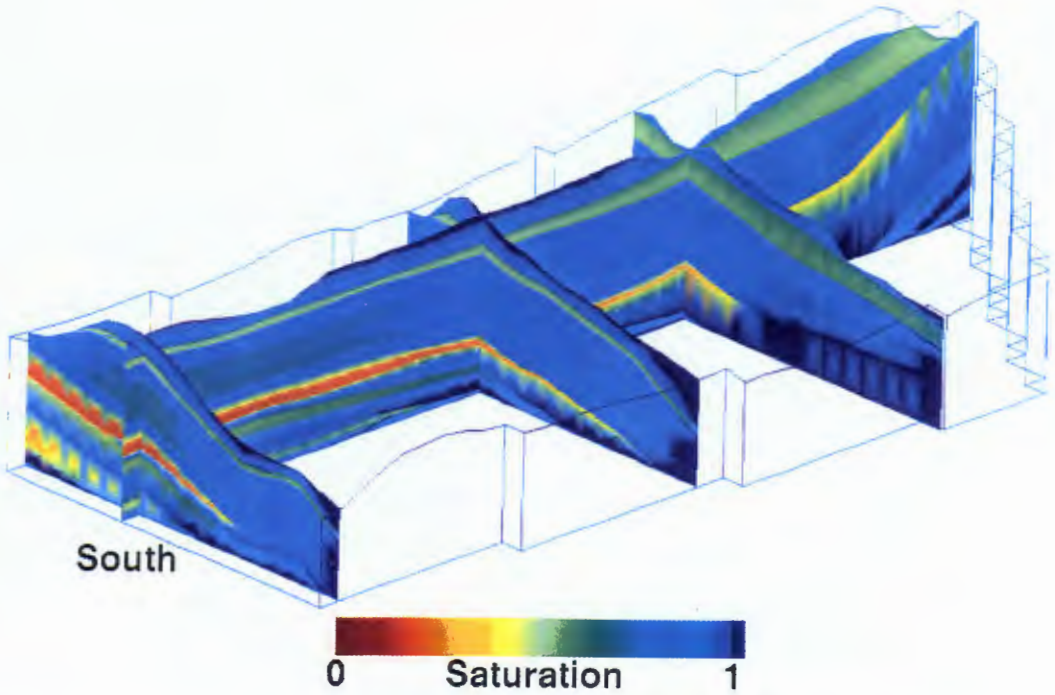

Figure 6-15.Saturation field for 0.1 mm/y infiltration rate; Equivalent Continuum Model.

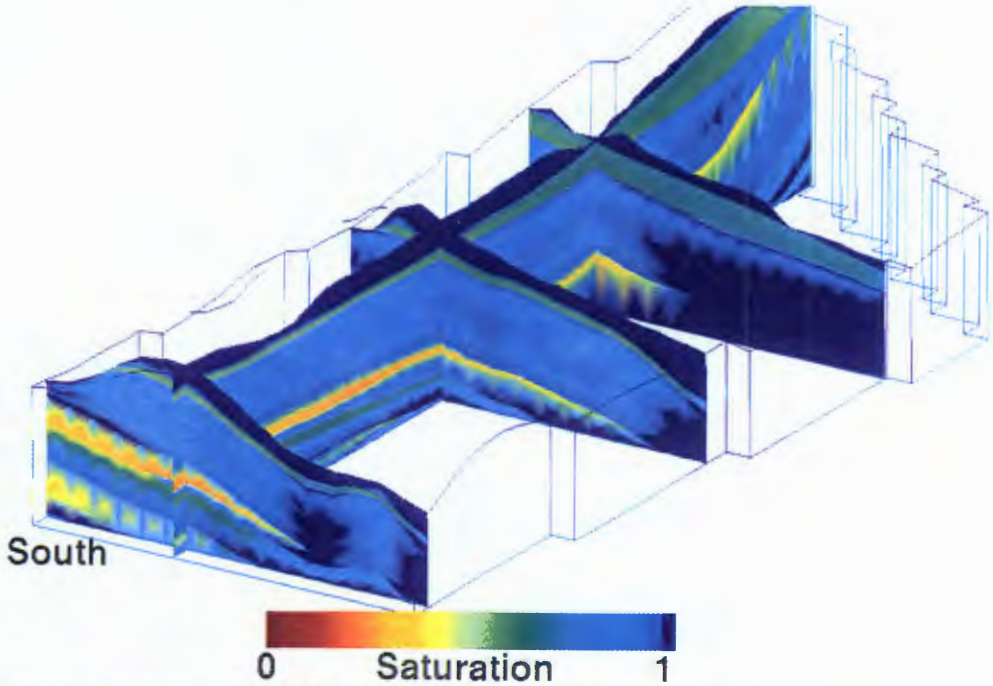

Figure 6-16.Saturation field for 1 mm/y infiltration rate; Equivalent Continuum Model.

DRAFT

The numerical simulation consists of injecting particles into the system at the surface for the first ten years of a 42 year simulation. The ten years represents, approximately, the time from 1953 to 1963 that global fallout of ^{36}Cl was substantially greater than natural background levels. The simulations are performed with the both three-dimensional equivalent continuum model and the three-dimensional dual permeability model, and a uniform infiltration rate of 1 mm/y is assumed for both cases. The movement of the particles into the system in the equivalent continuum model (not shown in a figure) is relatively uneventful. After 42 years, they remain distributed near the surface and show very little movement from their initial location. A substantial contrast is seen in the dual permeability simulation, where the location of injected ^{36}Cl after the 43 year simulation is shown in Figure 6-20. Figure 6-20 shows that the bomb-pulse chloride travels rapidly through the fractures in the Tiva Canyon welded tuff. It then moves into the matrix of the Paintbrush tuff, where its vertical progress is slowed. In some regions, particularly in the South, we see bomb-pulse chloride at the basal vitrophyre between the Topopah Springs and Calico Hills units. The flow path appears to be lateral, initiating at the unit outcrops on the West side of the model domain. This initial simulation represents one mechanism that may eventually be incorporated into mixing models to describe where the contributions to an individual sample for radiometric dating come from. This dual permeability model is the first three-dimensional flow and transport model to provide a numerical simulation that explains the rapid transport of bomb pulse to depths significantly below the surface..

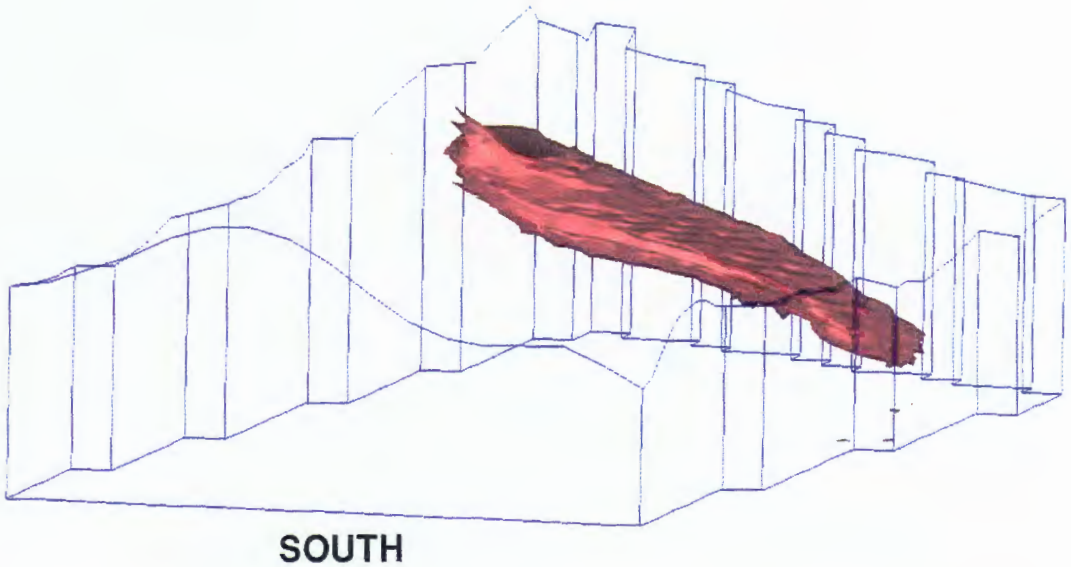

Figure 6-17.Solute plume isoconcentration surface from release at single surface point.

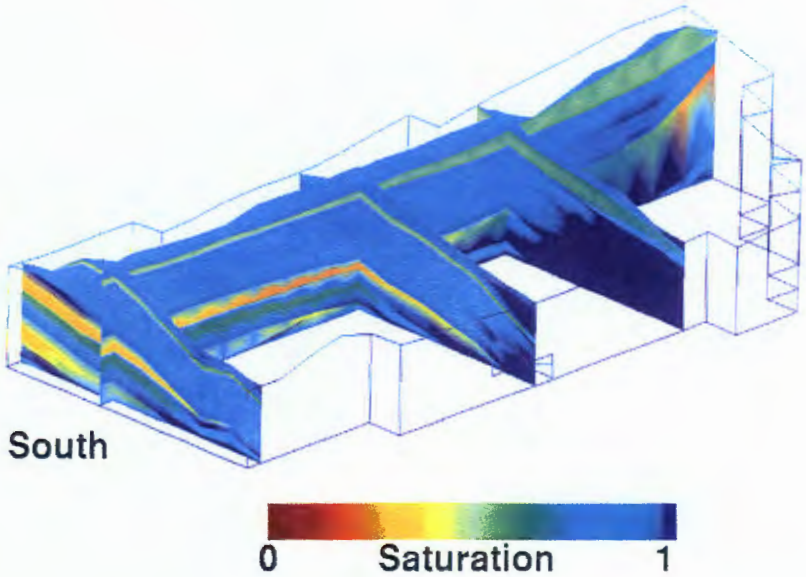

Figure 6-18.Dual permeability matrix saturations for 1 mm/y infiltration.

DRAFT

Another important link in the groundwater calibration problem involves relating isotopic measurements to infiltration source location and strength. Unlike the bomb-pulse problem described above which focuses on whether the bomb-pulse isotope is present or not, these studies utilize the long half-lives associated with the isotopes, ^{36}Cl in this case, to identify long subsurface travel times.

The nonuniform shallow infiltration map provided by Hudson and Flint (1995) has a mean of 21 mm/y over the area of interest. The map represents an effort to correlate neutron log measurements with topography, alluvial cover, and measured infiltration. That work is preliminary and advises that certain processes may not be adequately accounted for to relate shallow infiltration to net infiltration. For example, all components of evaporation may not be accounted for. Likewise, barometric pumping as a means of conducting shallow infiltrated water back to the atmosphere was not considered. Therefore, we normalized the shallow infiltration to a mean of 1 mm/y and acknowledge that work is in progress to relate shallow infiltration to net infiltration. The scaled nonuniform infiltration map was then used to investigate both the potential for nonuniform infiltration to drive lateral flow in the subsurface as well as the use of measured naturally occurring isotopes to identify flow paths and infiltration rates.

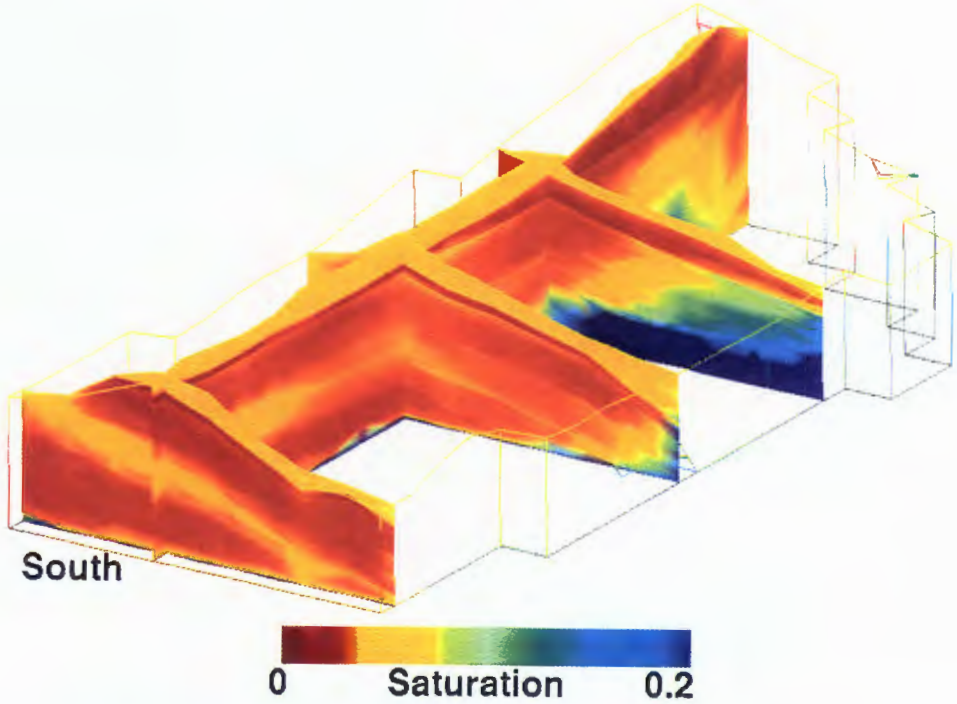

Figure 6-19.Dual permeability fracture saturations for 1 mm/y infiltration.

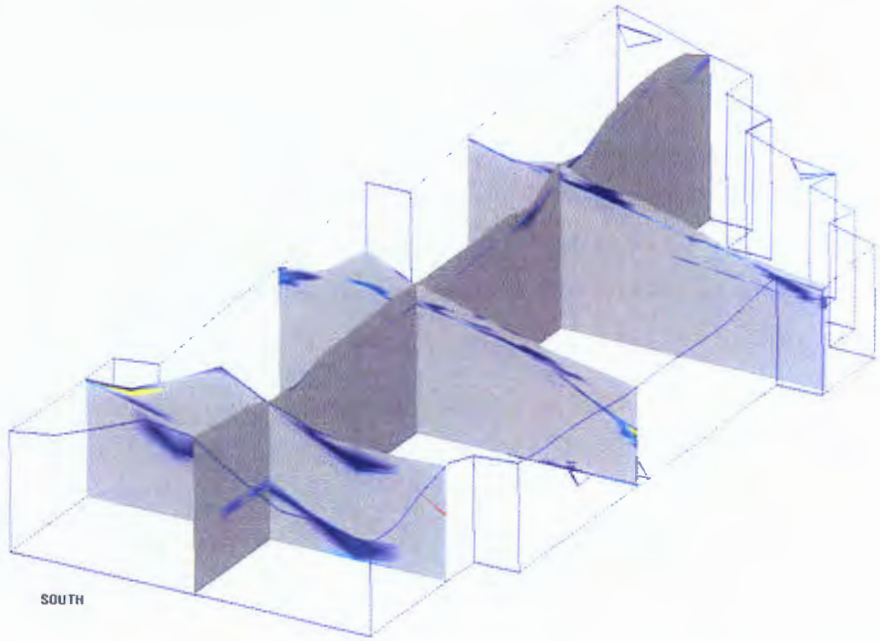

Figure 6-20.Bomb-pulse ^{36}Cl distributions for dual permeability solution.

DRAFT

The scaled version of the infiltration map of Hudson and Flint (1995) was used as an upper boundary for flow and transport simulations for both the two- and three-dimensional models. In this preliminary investigation of ^{36}Cl migration, the equivalent continuum formulation was used. After steady state flow was computed, the movement of ^{36}Cl was modeled. The concentration of ^{36}Cl was assumed constant in the infiltrating water and the radioactive decay of ^{36}Cl was incorporated in the solution (half-life 301,000 years).

Unlike the case shown in Figure 6-12 (^{36}Cl transport under low infiltration conditions), the two-dimensional simulations (through our Antler Ridge cross section) with this infiltration field using the equivalent continuum method did not highlight many significant flow patterns yielding vertical age inversions (younger water under older water) as might be expected considering the data in borehole UZ-16. This, however, does not indicate that there is no lateral flow in the model. It only shows that the infiltration rates used were all high enough to generate flow through the entire modeled section. In fact, Figure 6-21 shows that in the modeled scenario, lateral flow does carry the infiltrating water underneath the small section of virtually no infiltration on the east side of the Antler Ridge cross section.

When the entire three-dimensional flow field is considered, we see a very different situation than was shown in two dimensions. Figure 6-22 shows slices through the steady-state flow field with contours of age calculated from the ^{36}Cl concentrations. Here we see a number of structures showing younger water flowing under older water. The three-dimensional ^{36}Cl simulation shows two very important processes. First, the stratigraphy, when considered in three dimensions, leads to simulations that begin to show the mechanisms which match the observations, specifically, the occurrence of younger water under older water. Second, rather surprisingly, we found that the nonuniform infiltration map, as we scaled it, had very little effect on the three-dimensional ^{36}Cl profile. When a uniform infiltration of 1 mm/y was prescribed at the surface (not shown in a figure), the results were very similar and the same general flow pattern was found. The next step in investigating the role spatially nonuniform infiltration plays in driving three-dimensional flow in the subsurface will be to perform these simulations with the dual permeability model formulation. The bomb-pulse simulations described above already show the significance of fracture flow in transmitting some flow through fractured units very quickly. That result, combined with long-time ^{36}Cl simulations should help evaluate the significance of spatial zones of high infiltration in combination with moisture monitoring and isotopic analyses.

DRAFT

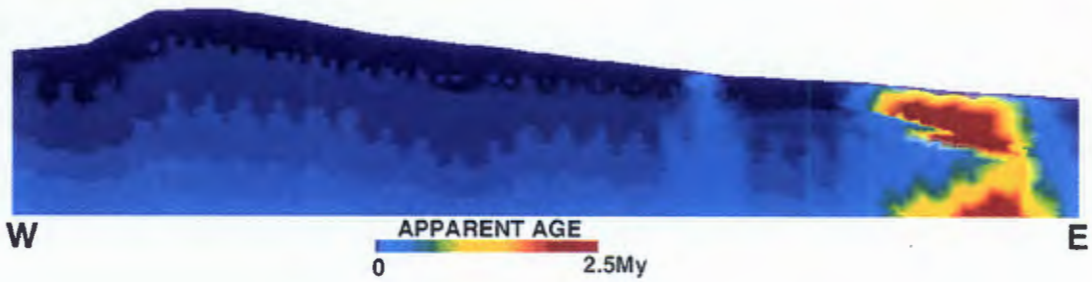

Figure 6-21.Apparent ages calculated from ^{36}Cl concentrations for Antler Ridge cross section with non-uniform infiltration field; Equivalent Continuum Model.

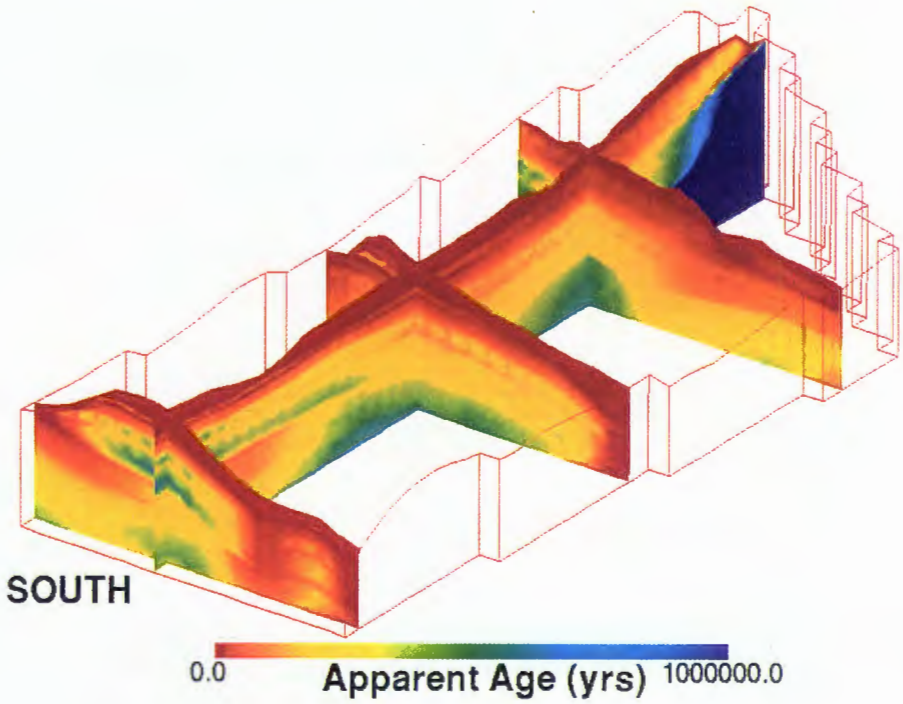

Figure 6-22.Apparent ages calculated from ^{36}Cl concentrations for the three-dimensional non-uniform infiltration field; Equivalent Continuum Model.

DRAFT

6.8 Numerical Performance

In this section we discuss some of the code performance issues associated with the calculations presented in this study. The process of obtaining steady state flow solutions on a large grid with heterogeneous and nonlinear properties can sometimes be tedious. Most newer simulation codes, including TOUGH2 and FEHM, are fully coupled and fully implicit. They use a Newton-Raphson iteration (outer iteration) and some kind of preconditioned conjugate gradient method to solve the associated linear system of equations (inner iteration). The Newton-Raphson method requires continuous derivatives and a relatively close initial guess of the solution to obtain its optimal second-order convergence. The nonlinear van Genuchten capillary functions are defined with residual liquid saturations. During the Newton-Raphson iteration the solution often overshoots below the residual liquid saturation. This in turn causes a break in the derivatives and a consequent deterioration in the numerical performance. Similar behavior occurs during phase changes, as when a node reaches complete saturation. The phenomena described affect the steady state flow simulations at Yucca Mountain because the transient simulation from an inital state is being used to obtain a steady state flow field. During this process, unrealistic initial guesses result in intermittent saturation of certain units, followed by draining to achieve the final saturation profile. Various smoothing techniques have been incorporated into simulation codes to help convergence but there is still work to be done in that area. Due to the importance of reproducing the results in this report, we are reporting the techniques we used to help speed convergence of the steady state flow solutions. They are listed below. We also note that all of the results in this report were obtained using the fully two-phase formulation of FEHM.

For equivalent continuum calculations, to speed up convergence:

- Use 0.5 saturation as an initial guess of the saturation.
- Use the result of a low infiltration run as an initial guess for a higher infiltration run, rather than starting the flow solution from scratch.
- If necessary, first use a "loose" tolerance and use that result as an initial guess for a run with a tighter tolerance.

For dual permeability calculations:

- Use the same techniques as in the equivalent continuum calculations.
- When setting constant saturation conditions on the bottom boundary, set the fracture saturation to a lower value than was employed in the equivalent continuum simulations (say, 0.6). The corresponding matrix saturation will still be fully saturated.
- Use an equivalent continuum solution as an initial guess for the dual permeability problem.

In reference to the last bullet, we wrote a simple code which reads the initial value file for FEHM and produces another with a user inputted value of fracture saturation for use in Dual Permeability simulations.

All of the three-dimensional site scale flow solutions were run on an IBM RISC 6000/590 machine with 512 Mb of memory. Code performance for two of the problems run for this report are given in Table 6-2. As can be seen from the table, performance varies almost linearly from small to large problems.

Table 6-2. Numerical Performance of FEHM for Steady State Flow Calculations (transient simulation is run until steady state is achieved).

Problem	Size (Equations/Connections)	Time Steps	Newton Iterations	CPU Time (s)
FEHM Simulation compared to LBL/ USGS Model	28300/99073	81	319	1518
Los Alamos Site Scale Model (nominal zeolite case)	103000/396800	101	385	6256

DRAFT

Table 6-3. LBL/USGS Rock Matrix Properties†

Hyrdogeologic Unit	Geologic Zone, per Scott & Bonk	Model Sub-Layer	Porosity (%)	Matrix Permeability (m^2)	Fracture Permeability (m^2)	Fracture Spacing § (m)	α Matrix (m^{-1})	α Fracture‡ (m^{-1})	n Matrix
Tiva Canyon (welded tuff)	caprock	1.1	17	1E-18	1.0E-08	0.618	0.0066 (Same as 1.2)	0.8	1.33
	upper cliff								
	upper lithophysae								
	clinkstone zone								
	lower lithophysae	1.2	17	2E-18	1.0E-08	0.618	0.0066	0.8	1.33
	hackly zone								
	columnar zone								
	vitrophyre	1.3	6	1E-18 (Assumed similar to 1.2)	1.0E-08	0.618	0.0066 (Same as 1.2)	0.8	1.33
Paintbrush (nonwelded tuff)	shardy base	2.1	33	1E-13	1.0E-08	2.22	0.160	10.0	1.20
	nonwelded tuffs	2.2	37	5E-14	1.0E-08	2.22	0.587	10.0	1.19
	bedded tuffs								
	nonwelded tuffs	2.3	32	1E-13	1.0E-08	2.22	0.424	10.0	1.17

† from Wittwer et al. (1995).
§ from Wilson et al. (1994).
‡ Fracture α described in Section 6.4. Fracture **n** set to 3 in all units as reported by Wilson et al. (1994).

DRAFT

Table 6-3. LBL/USGS Rock Matrix Properties† (Continued)

Hyrdogeologic Unit	Geologic Zone, per Scott & Bonk	Model Sub-Layer	Porosity (%)	Matrix Permeability (m^2)	Fracture Permeability (m^2)	Fracture Spacing§ (m)	α Matrix (m^{-1})	α Fracture‡ (m^{-1})	n Matrix
Topopah Spring (welded tuff)	vitrophyre	3.1	6	1E-18	1.0E-08	0.74	0.0066 (Assumed same as 3.6)	1.0	1.41
	caprock	3.2	15	4E-16	1.0E-08	0.74	0.012	1.0	1.22
	rounded zone				1.0E-08	0.74		1.0	
	upper lithophysae	3.3	13	4E-18	1.0E-08	0.74	0.020	1.0	1.28
	middle non-lithrophysae	3.4	14	5E-18	1.0E-08	0.74	0.013	1.0	1.33
	lower lithophysae								
	repository								
	lower non-lithophysae	3.5	12	5E-18	1.0E-08	0.74	0.0066	1.0	1.33
	vitrophyre	3.6	5	1E-18	1.0E-08	0.74	0.0066	1.0	1.41

† from Wittwer et al. (1995).
§ from Wilson et al. (1994).
‡ Fracture α described in Section 6.4. Fracture **n** set to 3 in all units as reported by Wilson et al. (1994).

DRAFT

Table 6-3. LBL/USGS Rock Matrix Properties† (Continued)

Hyrdogeologic Unit	Geologic Zone, per Scott & Bonk	Model Sub-Layer	Porosity (%)	Matrix Permeability (m^2)	Fracture Permeability (m^2)	Fracture Spacing § (m)	α Matrix (m^{-1})	α Fracture‡ (m^{-1})	n Matrix
Calico Hills (nonwelded tuff)	bedded tuffs	5.1	35	2E-13	1.0E-08	1.62	0.20	0.5	1.15
	nonwelded vitric	5.2	28	3E-13	1.0E-08	1.62	0.20	0.5	1.14
	bedded tuffs								
	nonwelded tuffs	5.3	39	3E-13	1.0E-08	1.62	0.20	0.5	1.14
	slightly zeolitized	5.4	25	1E-16	1.0E-08	1.62	0.010	0.5	1.23
	zeolitized, partly argillic	5.5	25	1E-16	1.0E-08	1.62	0.010	0.5	1.23
	zeolitized, devitrified								
	zeolitized								

† from Wittwer et al. (1995).
§ from Wilson et al. (1994).
‡ Fracture α described in Section 6.4. Fracture **n** set to 3 in all units as reported by Wilson et al. (1994).

Table 6-3. Rock Matrix Properties - Modified † (Continued)

Hyrdogeologic Unit	Geologic Zone	Model Sub-Layer	Porosity (%)	Matrix Permeability (m^2)	Fracture Permeability (m^2)	Fracture Spacing (m)	α Matrix (m^{-1})	α Fracture‡ (m^{-1})	n Matrix
Calico Hills (nonwelded tuff)	vitric non-welded	4.1	37	4E-16	6E-10	1.62	0.020	0.5	0.54
	zeolitized	4.2	29	7E-18	6E-10	1.62	0.0035	0.5	0.33
	devitrified	4.3	27	4E-16	6E-10	1.62	0.027	0.5	0.28
	zeolitized	4.4	29	7E-18	6E-10	1.62	0.0035	0.5	0.33
	devitrified	4.5	27	4E-16	6E-10	1.62	0.029	0.5	0.55
	zeolitized	4.6	29	7E-18	6E-10	1.62	0.0035	0.5	0.33
	devitrified	4.7	27	4E-16	6E-10	1.62	0.029	0.5	0.55

† Deliniation: Vaniman (personal communication, 1995).
¥ Properties: Loeven(1993).
‡ Fracture α described in Section 6.4. Fracture **n** set to 3 in all units as reported by Wilson et al. (1994).

DRAFT

DRAFT

7.0 Neptunium Migration Results

7.1 Criteria Used for Assessing Neptunium Migration Rates

To place the simulations of ^{237}Np transport into perspective, it is necessary to develop criteria for reducing the results and comparing them to one another. No single criterion will suffice for encapsulating the results because the behavior of ^{237}Np depends on many factors, including:

- Hydrologic properties and resulting flow conditions;
- Infiltration rate;
- Time-dependent ^{237}Np release function;
- Sorption properties;
- Diffusion properties.

In the present study we develop several criteria for assessing the results of a simulation and comparing the results. These criteria will allow the results to be presented in a variety of ways to gain the maximum information possible.

7.1.1 Travel time to water table

The time required for ^{237}Np to reach the water table is the most straightforward and understandable way to present the results of the simulations. Since the first arrival of ^{237}Np is strongly dependent on the degree of numerical dispersion, the preferred definition is the time required for the concentration to reach a given value at the water table. This definition is appropriate for a source term that is essentially constant. For a source term that more closely resembles a pulse of radionuclide, the time required for a given fraction of the released pulse is preferred. A value of 5% of the release concentration or 5% of the pulse mass represents the behavior of the most rapid moving radionuclide, whereas the 50% value represents an average travel time for the simulation. In the present study, we found that the pulse injection technique yielded a more straightforward analysis of the quantity of ^{237}Np reaching the water table.

7.1.2 Effective retardation factor

The travel time is a measure of transport performance that is dependent on the many factors listed above. To examine the impact of transport parameters such as sorption coefficient and matrix diffusion effects, the impact of the hydrologic properties must be factored out of the comparison. This is done by computing an Effective Retardation Factor (ERF) R_{eff} as follows:

$$R_{eff} = \frac{\tau_{Np}}{\tau_{cons}} \tag{7-1}$$

DRAFT

where τ_{Np} is the ^{237}Np travel time and τ_{cons} is the travel time of a conservative solute computed on the same flow field with the same release function from the potential repository and the same half-life as ^{237}Np. Thus the additional delay of ^{237}Np due to transport processes such as sorption is represented by the ERF. Even if there is uncertainty in the hydrologic conditions, the ERF should still provide a measure of the impact of transport parameters on travel time.

Different forms of the ERF are used in the present study to illustrate different points. First, the travel times used in the calculation still require the selection of a percentage of the release concentration or pulse strength, and the selection of this percentage is important to the interpretation. For example, an ERF based on the 5% value is used to establish the impact of retardation processes on the most rapid moving radionuclide. The ERF definition can also be tailored to examine the impact of individual transport processes. For example, if both the conservative solute and ^{237}Np are assumed to undergo matrix diffusion but only the ^{237}Np sorbs, then the ERF measures the effect of sorption on the matrix rock on travel time.

7.1.3 Other Comparison Methods

In some cases, less quantitative techniques must be used to compare the results of simulations, such as when the conceptual model is being altered. An example is the comparison of equivalent continuum and dual permeability model calculations. In these cases a variety of measures must be used to examine the simulation results. Both the particle tracking and finite element transport models will be used in these simulations because each transport model lends itself to examining different aspects of the transport system. Another type of comparison is pictorial, used to observe the extent of spreading of the radionuclide plume.

7.2 2-Dimensional Equivalent Continuum Calculations

In this section we present the results of a wide range of calculations performed on various two-dimensional cross sections of the Los Alamos unsaturated zone site scale flow and transport model. All calculations in this section utilize the equivalent continuum model for flow and transport, a model commonly used in the Project for numerical simulations. The assumption must be critically assessed for the validity ot the underlying assumptions, particularly the assumption that the fracture and matrix attain the same value of state variables such as capillary and gas pressure. For transport, an even more restrictive assumption is that the concentration of solute is equal in the fracture and matrix. Thus, regardless of the relative flow rates in the fractures and matrix, processes such as fracture-matrix flow and molecular diffusion are assumed to be rapid enough to homogenize the concentration, and the transport system behaves as one with an effective volumetric water content very close to that in the matrix. The validity of this assumption can be examined through order of

magnitude arguments and by utilizing models such as dual permeability that account for fracture flow and transport more explicitly. Both approaches will be used: the dual permeability simulations and a comparison with the equivalent continuum model are presented in Section 7.4.3.

In the remainder of this section, we first discuss the rationale for performing two-dimensional simulations to study the sensitivity of the transport system. We then present the cross sections and finite element grids used in the sensitivity analyses. A key issue for flow and transport is the accuracy of the numerical results, which is affected by the spatial discretization of the grid and the time step size. Section 7.2.2 presents the results of a study that address the numerical accuracy issue. Finally, in the bulk of this section we examine the sensitivity of the transport of ^{237}Np to the key parameters and uncertainties of the system, including: the infiltration rate and degree of nonuniformity of the infiltration rate; the point of release of the radionuclides within the region currently defined as the potential repository; the sorption coefficient K_d of ^{237}Np on the zeolitic tuffs; and the assumed thicknesses and spatial extents of the zeolitic units within the Calico Hills hydrogeologic unit.

7.2.1 Discussion of need for two-dimensional simulations

In Section 7.3 we demonstrate the importance of considering the three dimensional nature of the hydrogeologic system. Nonetheless, it is impractical to perform all of the necessary sensitivity analyses in three dimensions. This is especially true when one considers that we probably cannot, with current computational technologies, perform even a single three-dimensional calculation at a high enough spatial resolution to eliminate numerical dispersion when the dispersivity is low. Such a calculation might require 500,000 nodes, whereas in the present study 100,000 nodes was the practical limit. Future improvements in machine hardware and transport codes will make this goal a reality in the next few years. However, for now the three-dimensional calculations must be regarded as useful for examining issues related to the three-dimensional structure of the transport system, but not appropriate for repetitive sensitivity analysis calculations.

When interpreted properly, two-dimensional calculations provide a means for examining many issues important to the transport of ^{237}Np. Although three dimensional effects are of course ignored, the impact of key parameters such as infiltration rate, sorption coefficient, and assumed extent of the sorptive zeolitic units within the Calico Hills hydrogeologic unit can be studied. Also, by comparing two and three dimensional transport simulations, we can identify any systematic deviations and factor this comparison into the analysis. In this way the majority of the sensitivity analyses can be performed in two dimensions, thus saving computational time

and simplifying the process of distilling the calculational results into a form that can be readily understood.

7.2.2 Assessment of Numerical Errors

To examine the possibility of numerical errors in the two-dimensional transport calculations, a series of transport calculations were performed on the three grids constructed on the Antler Ridge cross section. Both finite element solute transport and particle tracking simulations were carried out to sort out the differences between changes in numerical dispersion of the solute transport calculation and changes in the flow field itself brought on by the more finely resolved flow solution. The grids used for the numerical accuracy study are shown in Figure 4-5. The first grid, called the coarse grid, was extracted directly from the three-dimensional grid constructed on 250 ft centers, and represents the most coarse grid in the accuracy study. An intermediate grid was constructed by applying one level of refinement to the coarse grid in each unit. The most finely resolved grid, called the fine grid, was then developed by applying an additional level of refinement to all layers at or below the potential repository. This last level of refinement was employed to provide additional resolution in the region where ^{237}Np will be traveling in the simulations. Figure 7-1 shows the results of particle tracking simulations in the absence of hydrodynamic dispersion for the three grids. In each simulation, 100,000 particles were injected at each of two positions at the potential repository, one near the middle of each segment of the repository on either side of the Ghost Dance fault. The particles are injected at time zero, and the cumulative breakthrough curves at the water table are recorded. There are subtle differences in the breakthrough curves for the three cases. These differences could reflect either changes in the flow field or grid orientation effects of the particle tracking technique. Since either of these numerical inaccuracies will be lower on the more finely resolved grid, this calculation shows that the finest resolution grid should be used in transport calculations.

A comparison of the particle tracking and finite element solute transport model is illustrated in Figure 7-2. The dispersivity was taken to be 25 m in these calculations. For the finite element simulations, it is unclear whether the differences as a function of grid discretization are due to flow field changes or to a lessening of numerical dispersion as grid resolution increases. Nonetheless, the curves seem to be converging to a solution that no longer varies significantly at the highest level of refinement. In theory, the particle tracking and finite element solutions should agree when numerical errors are reduced. The differences even at the highest level of refinement may be due to the limited range of dispersivities that can be solved accurately by both transport models (Robinson and Henderson, 1995). It is impossible to cite a single value for the grid Peclet number for an unstructured grid with widely varying element sizes, and in fact the criteria for accuracy of both methods probably are violated in some portions of the grid.

DRAFT

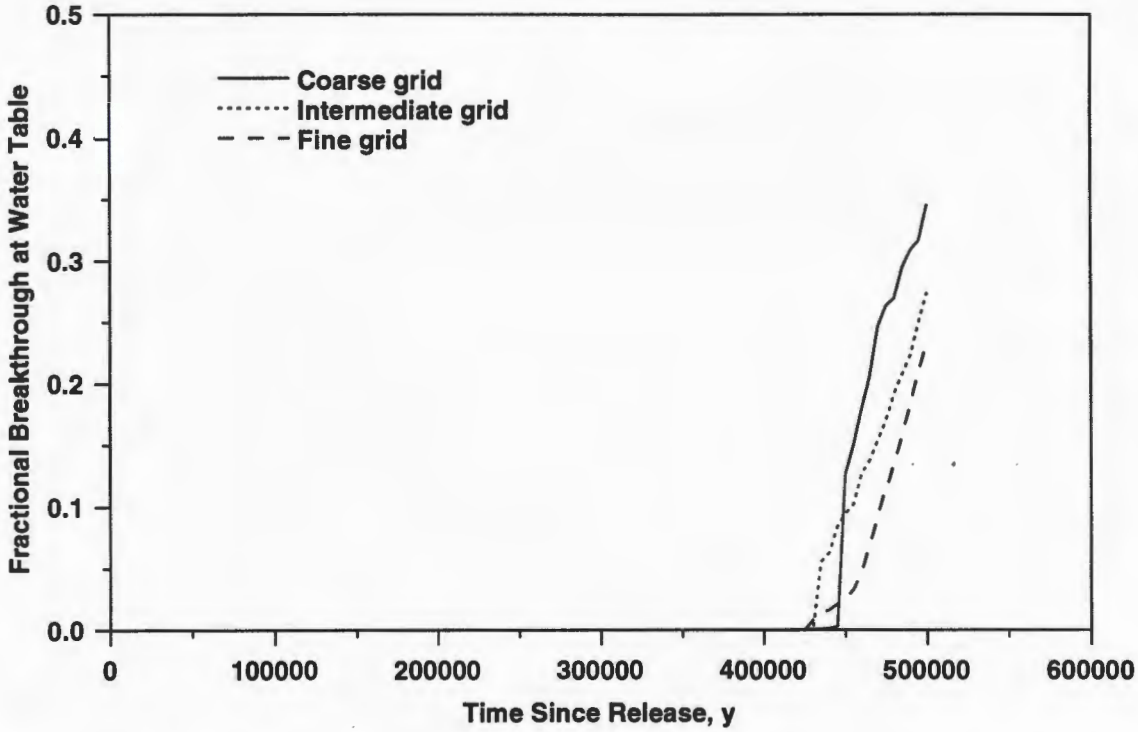

Figure 7-1. Particle breakthrough curves at the water table for the three finite element grids tested. In each calculation, the particles were released at two positions at the potential repository.

Nonetheless, the agreement at the highest level of refinement is close enough for the purposes of this study, as long as the breakthrough of the most rapid moving solute, say, the 1% breakthrough time, is not the measure of performance. Because of numerical dispersion, the finite element solution will provide an earlier arrival time than the particle tracking, and thus should not be used.

7.2.3 Base case simulations

In this section we present a "base case" simulation in some detail to illustrate the nature of the transport system and introduce some of the quantitative analysis techniques used in this study. We first examine the transport of a nonsorbing, conservative species compared to that of ^{237}Np in some detail for nominal values of infiltration rate and ^{237}Np sorption coefficient K_d. For this calculation on the Antler Ridge Cross section, we assume an infiltration rate of 1 mm/y, K_d of 2.5 g/cc, and the nominal case for the extent of zeolitic horizons within the Calico Hills. Figures 7-3a-c show the movement of a conservative radionuclide from positions approximately in the middle of each segment of the potential repository at times of 5000 y, 30,000 y, and

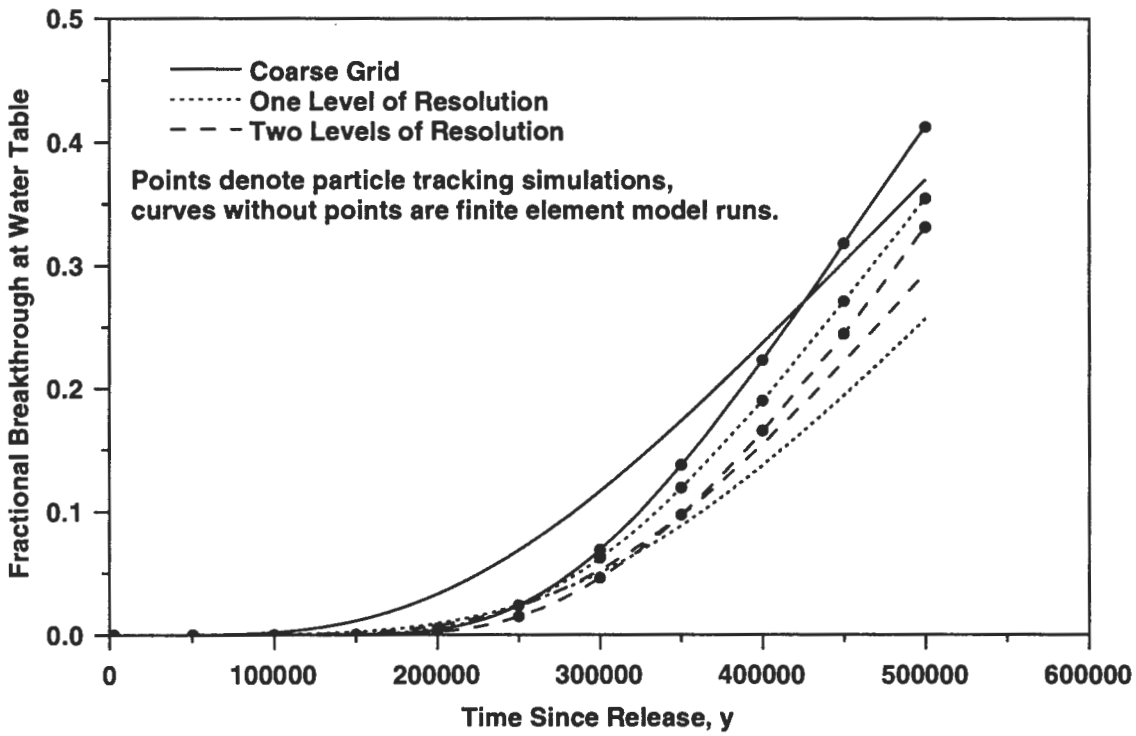

Figure 7-2. Breakthrough curves at the water table for the three finite element grids tested. Simulations for both particle tracking and finite element solute transport are shown. A dispersivity of 25 m was assumed.

75,000 y, respectively. The source term is a constant concentration at the release position, in keeping with our assumed source term for ^{237}Np. At this infiltration rate, the equivalent continuum solution dictates essentially one dimensional, downward movement of solutes from the potential repository to the water table. The dispersivity selected for this simulation results in a spreading of the front, but the mean arrival time at the water table is essentially a simple function of the downward flux of water and the volumetric water content (porosity times liquid saturation). Figures 7-4a-e are similar diagrams for the movement of ^{237}Np, simulated using a sorption coefficient model and radioactive decay modeled as an irreversible, temperature-independent first order reaction. To place the conservative solute and ^{237}Np calculations on the same basis, the same normalized release concentration is used in both cases. Thus the results would need to be normalized to the actual release concentration to estimate the quantity of radionuclide reaching the water table. Notice that the times for the figures a-c are the same for the two solutes, illustrating the retarded movement of ^{237}Np relative to that of the conservative solute. The final two figures are at much longer times of 250,000 y and 900,000 y when the ^{237}Np actually reaches the water table. The sorption coefficients are non-zero only in the

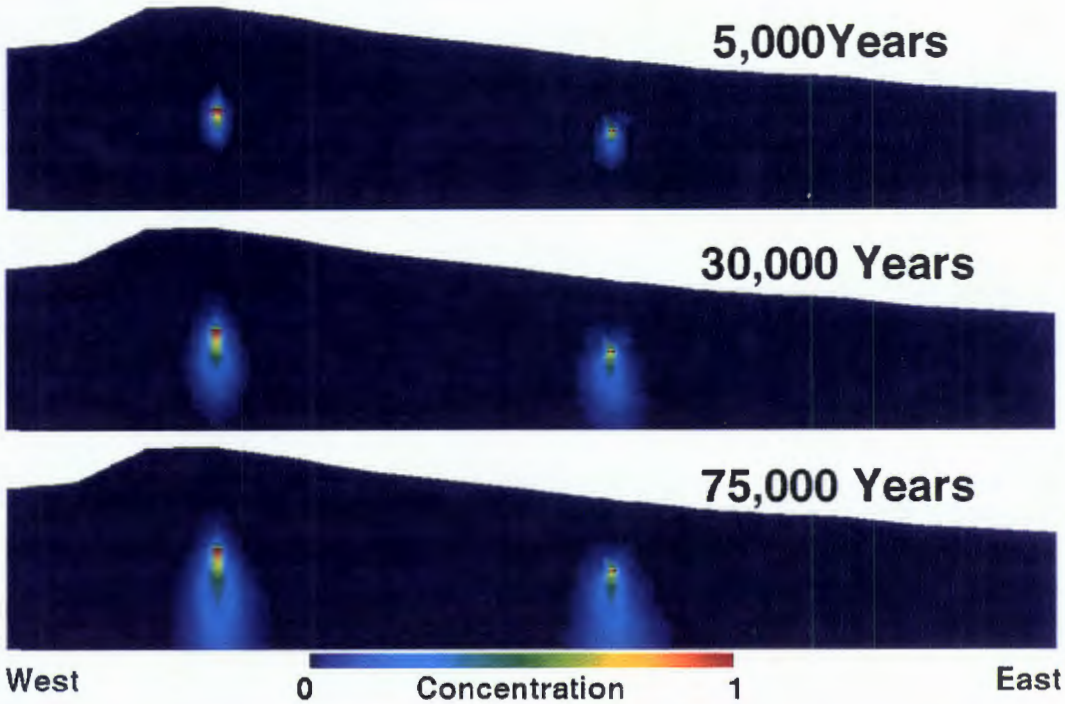

Figure 7-3. Base Case simulation of transport of a conservative radionuclide from positions on each segment of the potential repository. a) 5000 y; b) 30,000 y; c) 75,000 y.

zeolitized units, highlighted in Figure 4-2 as the shaded units. As explained in Section 2.2.1, the retardation factor within these units is of order 20 (for a sorption coefficient of 2.5 cc/g), with no retardation in the Topopah Springs units or the vitric and devitrified subunits of the Calico Hills. Transport times to the water table are the result of transport in alternating sorptive and nonsorptive units. Note that the ^{237}Np results are affected somewhat by radioactive decay. Strictly speaking, the conservative solute could be made to decay with a half-life of 2.14×10^6 y to place the two solutes on the same basis. However, unless the travel times are of the order of one million years or greater in the unsaturated zone, the effect on the breakthrough times and ERF values will be minor.

Figure 7-4e also illustrates that the impact of sorption is not uniform across the potential repository. At this cross section, ^{237}Np encounters somewhat more sorptive zeolites during its travel to the water table in the western release point. Thus the results of a specific simulation will depend on many factors including the sorption coefficient, flow and transport direction, geologic structure, and release point. It will be necessary to consider all of these points in interpreting the quantitative results that follow.

DRAFT

Breakthrough curves for this same transport system may be generated to obtain quantitative results for this example. The simulation technique is to inject a pulse of conservative or sorbing solute and record the fraction of the solute that reaches the water table versus time. Figure 7-5 illustrates the effect of sorption of ^{237}Np in delaying the arrival at the water table. The times for 5% and 50% of the released ^{237}Np to reach the water table from the Western point in this simulation are 313 ky and 864 ky, respectively, compared to values of 38.6 ky and 76.1 ky for the conservative solute. Thus the effective retardation factors ERF for 5% and 50% arrivals at the water table are 8.11 and 11.4. Despite the spreading caused by dispersion, the impact of sorption on travel time as measured by the ERF value is relatively constant. This illustrates that even with uncertainty in the transport parameters such as the dispersivity, the ERF is a useful parameter for capturing the role of sorption.

Particle tracking simulations in the absence of dispersion are another way to assess the sensitive parameters of the transport system. When the dispersivity is set to zero, the only spreading of the radionuclide is due to large scale velocity variations resulting in different pathways to the water table. Figure 7-5 also shows a particle tracking breakthrough curve for a dispersivity of 0. The 5% and 50% arrival times of ^{237}Np are 750 ky, and 839 ky, respectively. The 50% breakthrough time agrees closely to the finite element simulation with a dispersivity value of 25 m, since to a first approximation dispersion affects the spreading of the solute but not the central tendency of the solute front. However, the 5% breakthrough time is significantly affected by dispersion, illustrating that if the performance measure is the arrival of the most rapid moving radionuclide, the dispersivity is a key parameter.

Finally, though it appears from these illustrations of radionuclide movement that a simple one-dimensional model would suffice, this of course is true only for the simplest assumptions about the transport system, and is not valid in general. Even in cases for which the transport appears one dimensional, the flux of water through the potential repository horizon depends on the infiltration rate at the surface and the fraction of water that is diverted laterally at the contact between the Tiva Canyon welded unit and the nonwelded Paintbrush tuff underneath. Furthermore, we showed in Section 6.0 that three-dimensional effects and nonuniform infiltration will also cause flow and transport to be more complex than can be described with a one-dimensional model.

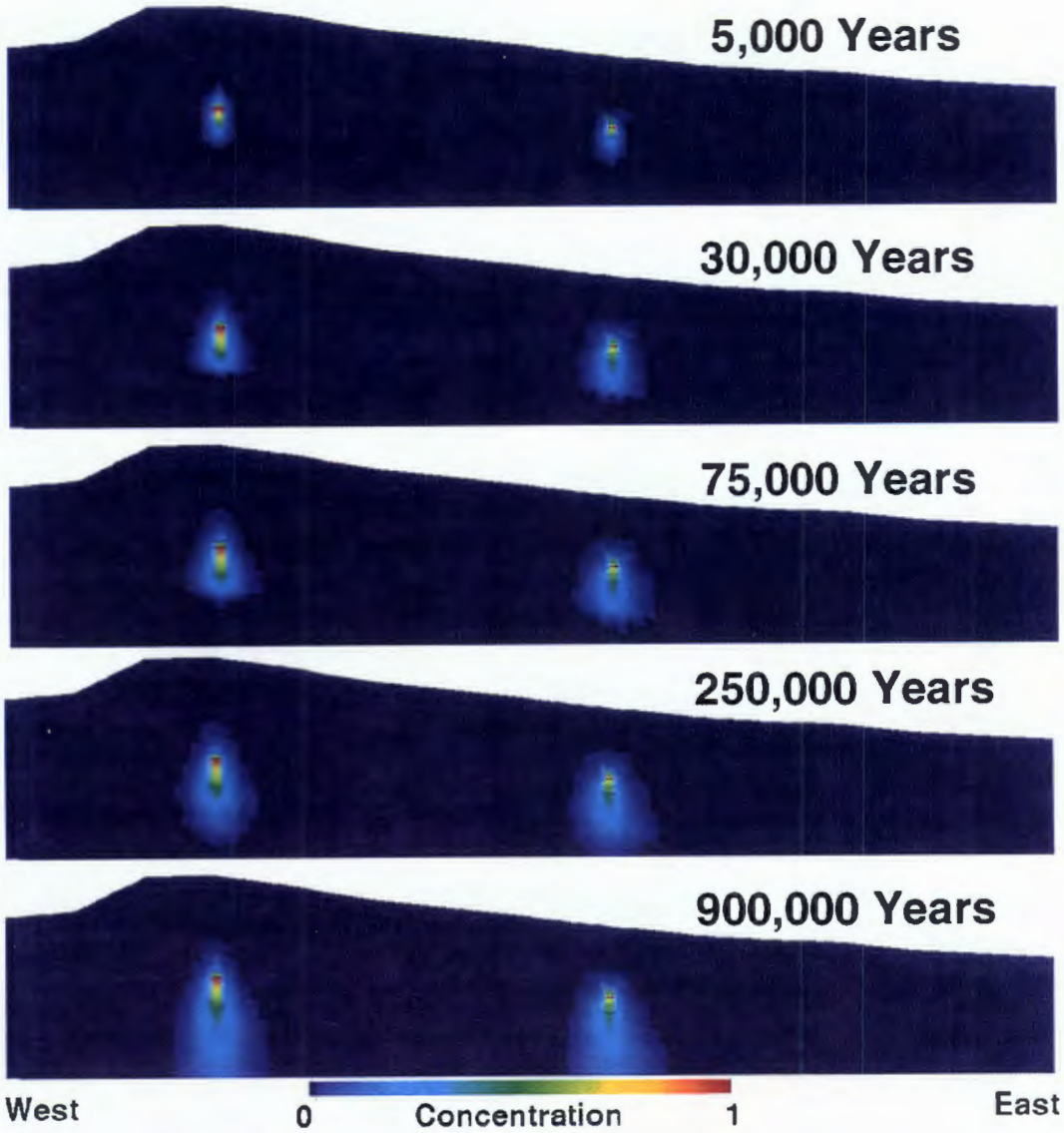

Figure 7-4. Base Case simulation of transport of ^{237}Np from positions on each segment of the potential repository. a) 5000 y; b) 30,000 y; c) 75,000 y; d) 250,000 y; e) 900,000 y.

7.2.4 Migration as a function of infiltration rate and position of release

In this section we employ the equivalent continuum model in a series of two-dimensional simulations to study the sensitivity of ^{237}Np transport to the infiltration rate and position of release of the radionuclide. As discussed in the previous section, if the performance measure is the time required for a given percentage of the released radionuclide to reach the water table, then it is more convenient to release a pulse of radionuclide at the start of the simulation. These simulations take this approach. The infiltration rate is assumed to be uniform along the surface.

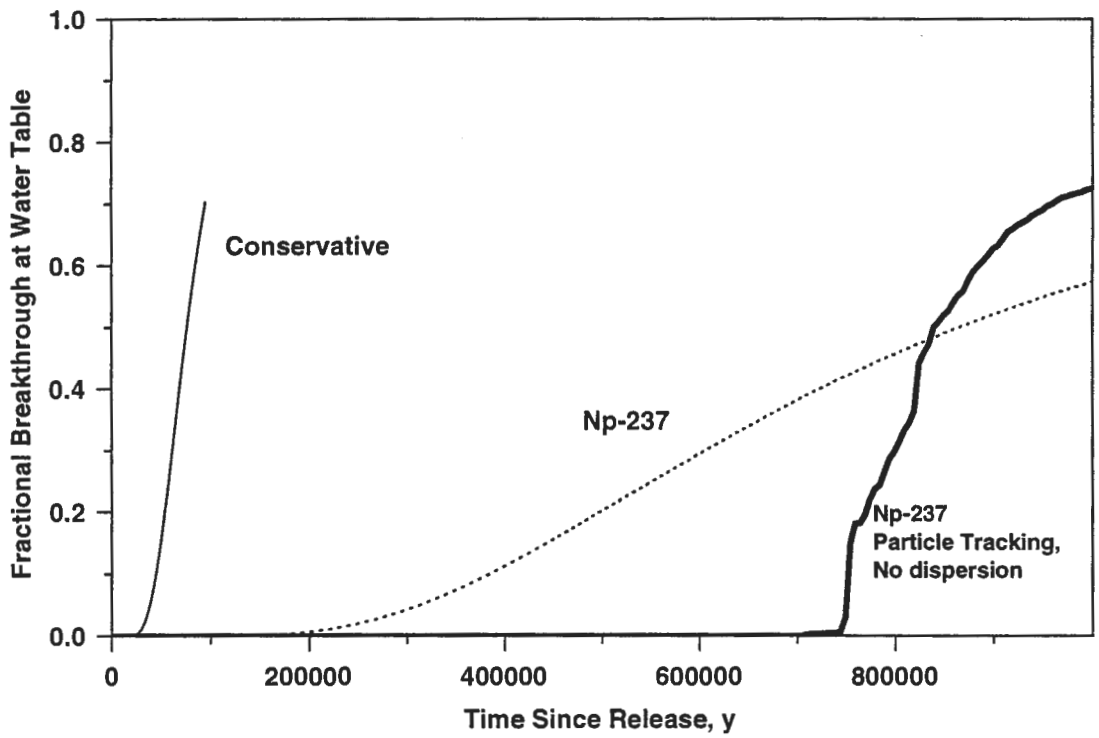

Figure 7-5. Base Case simulation of breakthrough curves for a conservative solute and ^{237}Np.

An East-West and a North-South cross section are studied because each of these cross sections allows specific aspects of the transport system to be studied. For example, the East-West cross section captures the predominant dipping of the hydrogeologic units and its impact on lateral flow and transport, while the North-South cross section can incorporate variations in the hydrostratigraphy in that direction. The position of release is varied because the system may exhibit sensitivity to the specific flow paths taken from the potential repository horizon to the water table.

Numerical Simulation Considerations. For each of the two-dimensional, East-West cross section simulations, the Antler Ridge cross section with two levels of refinement below the potential repository was used. This 8000 node grid was determined in Section 7.2.2 to minimize numerical errors for both flow and transport. The North-South cross section (with an East-West Nevada State Coordinate of 170,750 m) was generated with the same level or refinement, and contains 16,195 nodes. The fluid flow simulations are carried out using the isothermal air-water module of FEHM, which assumes that the gas phase contains air but no water vapor. To set the upper boundary condition, a pre-processor was used to compute the surface area associated with each node along the upper surface. Then, a constant infiltration rate is converted into a spatially

dependent mass flow rate at each node for input into FEHM. The bottom boundary is prescribed as a high saturation using the FEHM option that sets the outlet flow rate $\dot{m}$ at each lower boundary node to $\dot{m} = A_p(S - S_{set})$, where S_{set} is the prescribed saturation at the node. When the impedance parameter A_p is set high enough, the saturation S approaches the prescribed value. For a water table boundary condition, S_{set} is set to a value of 0.95 or greater, typically 0.999, and the parameter A_p is adjusted to obtain a final, steady state saturation within 0.1% of S_{set}. The two sides of the model domain are no flow boundaries for flow and transport. With a constant infiltration rate at the surface and constant saturation at the water table, the model is run until a steady state flow field is obtained. A steady state flow field is identified by nonchanging pressures and saturations throughout the model domain. The mass balance is checked by ensuring that the sum of the flows into the domain at the surface equals the sum of the flows out the bottom at the water table to within 0.1%

Once a steady state flow field is obtained at a given set of hydrologic input parameters, finite element or particle tracking simulations are run by restarting the code with the same hydrologic parameters and the restart file which contains the pressures and saturations from the steady state calculation. Once the flow field is re-established upon restart, the fluid flow solution may be turned off to save computational time and the transport calculation performed. Radionuclides are introduced into the system either by identifying the node number directly or by specifying the coordinates of the release position and allowing FEHM to locate the node point closest to the chosen position. In either case, an individual node is selected for a point source of radionuclide. The concentration of radionuclide is held at a constant concentration over a prescribed period of time (typically a short interval for a pulse injection). Although radionuclide release from the entire potential repository zone could easily have been simulated, point sources were employed to allow the details of the transport from the repository to the water table to be observed more readily. To measure the performance, the fraction of released radionuclide that exits the model domain (and thereby enters the saturated zone) versus time is recorded.

East-West Cross Section Simulations. Figure 7-6 shows the model domain for the East-West cross section through Antler Ridge, highlighting the two segments of the potential repository. The Ghost Dance fault separates these two segments in this cross section. Also shown are the six release points from which radionuclides emanate from the repository, three on

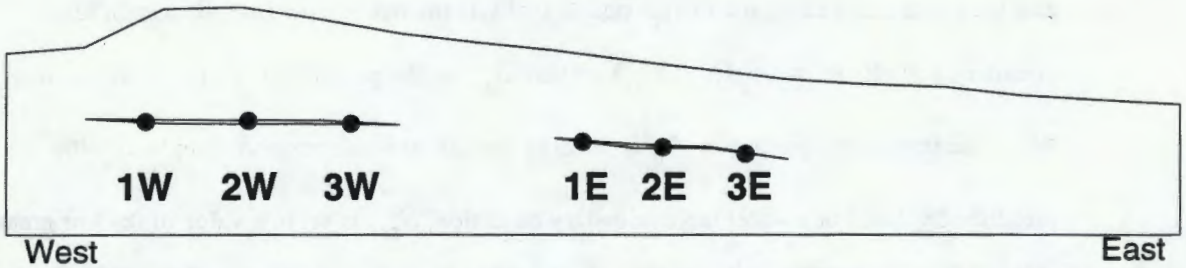

Figure 7-6. Diagram of two-dimensional, East-West model domain at Antler Ridge, showing the positions of release within the two segments of the potential repository.

either side of the Ghost Dance fault. Figures 7-7 and 7-8 show the breakthrough curves at the water table for solutes released at each of the six points selected within the potential repository. For all of the equivalent continuum simulations presented in this section, the finite element solution is used to simulate transport. Figure 7-7 shows simulations of a conservative, non-decaying solute, while Figure 7-8 shows the results for ^{237}Np, assuming a K_d of 2.5 cc/g (the average value determined from the batch sorption studies) in the three zeolitized units and 0 elsewhere. The ^{237}Np calculations also include radioactive decay with a half-life of 2.14×10^6 y. Taking point 2W as an example, median (50%) breakthrough time for the conservative solute at 1 mm/y is 76.1 ky, while the corresponding time for ^{237}Np is 864 ky. The ratio of these times results in a 50% ERF of 11.4 for point 2W. Recalling that the retardation factor for ^{237}Np is about 20 in the zeolites, this value of roughly half of the zeolite retardation factor is reasonable, considering that the ^{237}Np travels through alternating layers of zeolitized and vitric or devitrified tuffs. This increase in arrival time at the water table of roughly an order of magnitude for ^{237}Np compared to a conservative solute is typical for the Yucca Mountain unsaturated zone.

Of course, there is not simply one arrival time for solute at the water table in any real system. The relatively large spread in arrivals times over which the solutes reach the water table is due to two effects: the dispersivity of the medium and the macroscopic spreading of the solute due to the different pathways resulting from the stratigraphic variations from the potential repository to the water table. To understand the relative magnitudes of the two effects, compare the breakthrough curves for ^{237}Np in Figure 7-8, which contrasts the breakthrough curves for dispersivities of 0 and 25 m. The relatively large dispersivity chosen results in more spreading of radionuclides than the macroscopic dispersion effects.

DRAFT

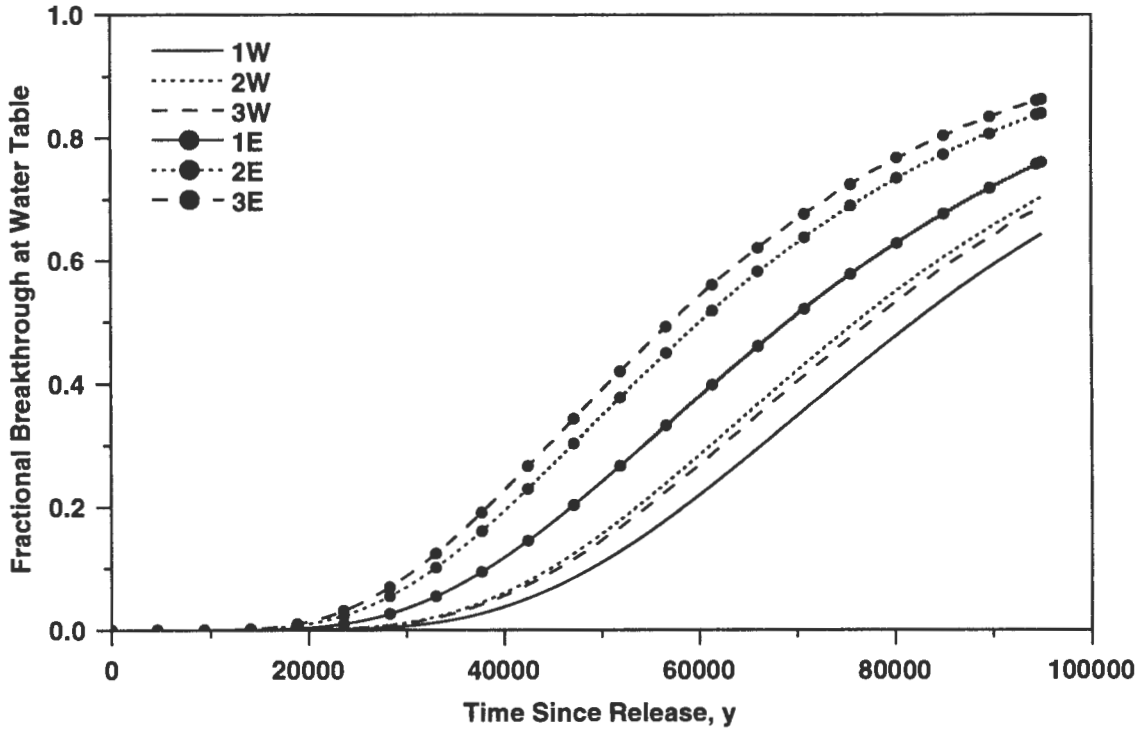

Figure 7-7. Breakthrough curves at the water table for the six release points for a conservative, non-sorbing solute at 1 mm/y uniform infiltration rate.

The practical consequence of hydrodynamic and macroscopic dispersion is that the median arrival time may not be the appropriate one for examining the transport system. For example, if the fastest moving radionuclide is of interest, then a more appropriate measure is the 5% arrival times, to capture the transport characteristics of the front edge of the contaminant plume. Lower percentage arrival times could be selected, but the results would probably be negatively impacted by numerical dispersion. Even if an accurate transport calculation for the 0.1% or 1% arrival time could be performed, the vagaries of the advective-dispersion model for characterizing front movement call into question whether such a low value should be used for comparison. Thus we select the 5% arrival time for examining the fastest moving radionuclides. Again using point 2W for comparison, the 5% breakthrough time for the conservative solute at 1 mm/y is 38.6 ky, while the corresponding time for ^{237}Np is 313 ky, or a 5% ERF of 8.11.

There are at least two reasons for a somewhat lower 5% ERF than the median ERF. First, when the arrival times approach or even exceed the half-life of ^{237}Np, radioactive decay plays a more prominent role in the breakthrough curve. Since the median arrival times are considerably longer than the 5% arrival times, radioactive decay has more time to act on the ^{237}Np, so that the arrival times are longer than they would have been in the absence of decay. Part of the

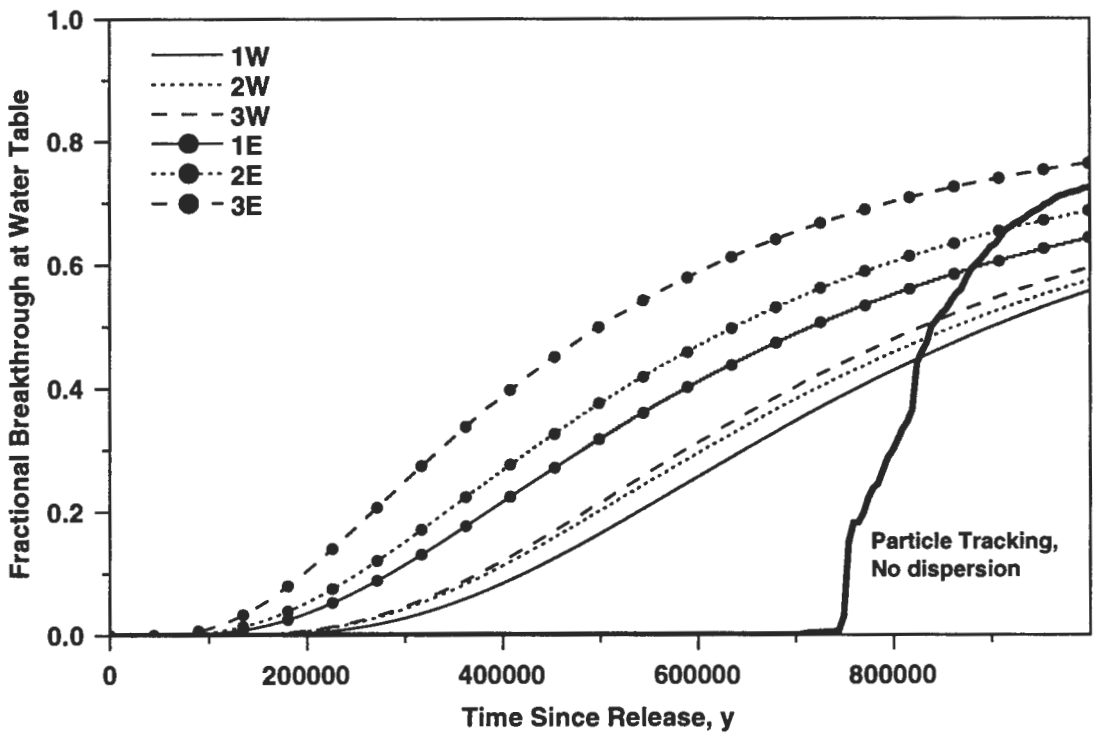

Figure 7-8.Breakthrough curves at the water table for the six release points for ^{237}Np at 1 mm/y uniform infiltration rate.Sorption coefficient K_d = 2.5 cc/g.

difference in the 5% and 50% ERF values can be attributed to this effect. Also, some of the fastest moving radionuclides could be traveling preferentially through strata that do not contain zeolites, thereby lowering the 5% ERF. Given the predominantly vertical transport in this simulation, the latter reason is probably not as important in this case, though in other simulations we demonstrate that lateral diversion plays a significant role.

The position of release also affects the arrival times and ERF values of the conservative solute and ^{237}Np. Table 7-1 shows the computed 5 and 50% arrival times and ERF values at 1 mm/y, uniform infiltration rate for all six release points. Regarding the conservative solute, which is indicative of the movement of water, there is a general trend toward smaller arrival times from West to East, both within a segment of the potential repository, and when the Eastern segment is compared to the western segment. The travel times range from 26.2 ky to 42.3 ky (5% arrival), or 57 ky to 82 ky (50% arrival). The corresponding ^{237}Np transport times are 154 ky to 346 ky (5% arrival), or 500 ky to 902 ky (50% arrival). Part of the trend from West to East is due to the shorter travel distance from the potential repository to the accessible environment. There is also an effect due to lateral diversion above the potential repository at the contact between the PTn and TSw hydrologic units. When flow travels laterally at this contact

Table 7-1. Arrival Times and Effective Retardation Factors for a Conservative Solute and ^{237}Np, 1 mm/y Uniform Infiltration

5% Arrival Position	Conservative Time, ky	^{237}Np Time, ky	5% ERF
1W	42.3	346	8.18
2W	38.6	313	8.11
3W	39.2	306	7.81
1E	32.5	222	6.83
2E	27.8	196	7.05
3E	26.2	154	5.88
50% Arrival Position	**Conservative Time, ky**	**^{237}Np Time, ky**	**50% ERF**
1W	81.9	902	11.0
2W	76.1	864	11.4
3W	77.5	831	10.7
1E	69.0	716	10.4
2E	60.1	639	10.6
3E	57.1	500	8.76

toward the East, the downward component of flow in the East is enhanced, since there is a no-flow boundary at the Eastern edge of the model domain, corresponding to the Bow Ridge fault. If this boundary accurately represents the hydrologic behavior of the fault, then the trend being discussed is a real effect. Otherwise, it would be an artifact of the boundary condition. This phenomenon is discussed further in the dual permeability transport simulations (see Section 7.4).

Regarding the ^{237}Np transport times, the retardation due to sorption is present regardless of where the radionuclide is released in this cross section. This is because there are ample zeolites between the potential repository and the water table throughout the repository region. There appears to be a slight decrease in the benefit of sorption in the Easternmost point simulated, especially for the 5% ERF, representing the fastest moving radionuclide. A small fraction of the radionuclide travels laterally to the East before migrating downward to the water table, thereby traveling through thinner zones of zeolitic rock. This means that the geologic barrier may be somewhat less effective at retarding the movement of ^{237}Np. Nonetheless, at the nominal infiltration rate of 1 mm/y, sorptive retardation plays a significant role regardless of the release point. One of the key issues for these calculations then is the extent to which different model conceptualizations affect the amount of lateral diversion that manifests itself in the units

beneath the potential repository. Dual permeability calculations are presented to address this issue more fully in Section 7.4. Tables 7-2 and 7-3 show the computed arrival times at

Table 7-2. Arrival Times and Effective Retardation Factors for a Conservative Solute and ^{237}Np, 0.1 mm/y Uniform Infiltration. Values in () are the maximum percent reaching the water table when the 50% arrival is not attained.

5% Arrival Position	Conservative Time, ky	^{237}Np Time, ky	5% ERF
1W	358	4370	12.2
2W	325	3750	11.5
3W	305	3120	10.2
1E	283	2470	8.73
2E	229	1950	8.52
3E	213	1480	6.95
50% Arrival Position	**Conservative Time, ky**	**^{237}Np Time, ky**	**50% ERF**
1W	734	(11%)	N/A
2W	668	(13%)	N/A
3W	628	(16%)	N/A
1E	620	(19%)	N/A
2E	515	(23%)	N/A
3E	489	(29%)	N/A

infiltration rates of 0.1 and 4 mm/y, respectively. The general trend toward shorter travel times of the conservative solute at higher infiltration rates is to be expected due to the more rapid flow velocities. The travel times are in general inversely proportional to infiltration rate, as expected. Slight deviations from this relationship are to be expected. At higher infiltration rates, fluid saturations are higher, resulting in slightly larger travel times than would be implied by the ratio of the infiltration rates. However, saturation differences are expected to be small even over a wide range of infiltration rates. For example, the nominal value of saturation rises from 0.9 to close to fully saturated in the TSw despite a change by a factor of 40 in assumed infiltration rate. This means that a match to the saturation profile in the model domain is by no means sufficient for predicting the migration of radionuclides. It is far more important to set the infiltration rate properly, since it has a first order effect on transport times. Conversely, even though the saturations at the highest infiltration rates studied are higher than the measured values in some units, this fact is expected to have only a secondary effect on transport time

Table 7-3. Arrival Times and Effective Retardation Factors for a Conservative Solute and ^{237}Np, 4 mm/y Uniform Infiltration

5% Arrival Position	Conservative Time, ky	^{237}Np Time, ky	5% ERF
1W	11.4	81.8	7.18
2W	10.3	72.9	7.08
3W	10.2	71.3	6.99
1E	8.12	50.7	6.24
2E	6.86	43.4	6.33
3E	6.16	33.2	5.39
50% Arrival Position	**Conservative Time, ky**	**^{237}Np Time, ky**	**50% ERF**
1W	22.2	198	8.92
2W	20.5	193	9.41
3W	20.2	185	9.16
1E	17.5	159	9.09
2E	15.0	140	9.33
3E	13.8	112	8.12

predictions, as long as the computed flow patterns and fluid flux values between the potential repository and the accessible environment are accurate.

The travel times for ^{237}Np as a function of infiltration rate follow a trend similar to that of the conservative solute (travel time inversely proportional to infiltration rate). The main effect complicating the interpretation is the impact of radioactive decay. At the low infiltration rate of 0.1 mm/y, the 5% travel times range from 1480 ky to 4370 ky (East to West). At this infiltration rate, there are no 50% arrival times for ^{237}Np for any of the release points: travel times are long enough for radioactive decay to reduce the amount released to less than 50% of the mass introduced. Thus, instead of the 50% arrival time, Table 7-2 indicates the percent of released ^{237}Np that reaches the water table after 10 my. This value is effectively a steady state value, since there is little ^{237}Np remaining in the system by this time (10 my is roughly five half-lives for ^{237}Np). If the infiltration rate is really this low, ^{237}Np transport times in the unsaturated zone will be long enough for radioactive decay to reduce concentrations considerably.

At the highest infiltration rate of 4 mm/y, ^{237}Np travels fairly rapidly to the water table. The 5% arrival time ranges from 33.2 ky to 81.8 ky (East to West), while the median arrival time ranges from 112 ky to 198 ky. These travel times are still quite large despite the high

infiltration rate selected, illustrating the effectiveness of the geologic barrier at retarding the movement of radionuclides. Note that for these travel times, the impact of radioactive decay should be small. Therefore, the systematic difference in the 5% and 50% ERF values as a function of infiltration rate indicates that the fastest moving ^{237}Np actually takes a path that to some extent bypasses the zeolitic rocks (though not completely, or else the ERF would be 1), even though the center of mass of the plume travels through the zeolites. Whether this effect is important depends largely on the performance measure to be applied to the waste isolation system. A criterion based on a 10,000 y minimum time for release to the accessible environment is likely to be dominated by the fastest moving radionuclide, while a dosed-based standard will lead toward a focus on the movement of the center of mass of the plume.

North-South Cross Section Simulations. A similar set of calculations were performed on the 16,000 node, North-South cross section at a uniform infiltration rate of 1 mm/y. This cross section cuts through the Western segment of the potential repository such that Point 2W of the Antler Ridge cross section is the middle point of the three studied in the North-South Cross section. The other two release points were North and South of this one. Table 7-4 shows the

Table 7-4. Arrival Times and Effective Retardation Factors for a Conservative Solute and ^{237}Np, 1 mm/y Uniform Infiltration, North-South Cross Section. Value in () are for simulations at the same location in the East-West croess section.

5% Arrival			
Position	Conservative Time, ky	^{237}Np Time, ky	5% ERF
South	68.8	685	9.96
Middle	66.8 (69.0)	797 (750)	11.9
North	61.0	588	9.64
50% Arrival			
Position	Conservative Time, ky	^{237}Np Time, ky	50% ERF
South	75.7	780	10.3
Middle	75.3 (76.0)	953 (839)	12.7
North	70.1	764	10.9

results of the transport simulations, comparing the results with that of release position 2W of the Antler Ridge cross section. The transport simulations in this case were carried out using particle tracking. There is good agreement with the results of the Antler Ridge cross section. Furthermore, there is very little sensitivity to the release position in the North-South cross section, implying that the in both cases the flow is essentially one-dimensional vertical flow,

DRAFT

and that the thickness of zeolites encountered by radionuclides is not a strong function of position in the Western segment of the potential repository. This point is discussed further in Section 7.2.7.

7.2.5 Migration as a function of dispersivity

The simulations discussed in this section compare the transport times to the water table from positions 2W and 2E at 1 mm/y, uniform infiltration rate for various values of dispersivity α ranging from 0 to 25 m. The simulation at 0 m is a particle tracking calculation, whereas the 10 and 25 m runs used the finite element solution to the convective-dispersion equation. This approach was taken to utilize the transport model best equipped to simulate the case at hand: particle tracking for advection-dominated transport with no hydrodynamic dispersion, and a finite element solution for systems with significant dispersion-induced spreading of the solute plume. Both approaches automatically include solute spreading caused by macroscopic effects such as the presence of hydrologic units of contrasting properties.

Table 7-5 summarizes the results of simulations studying the effect of dispersivity α on the behavior of the transport system. The arrival time of the fastest moving conservative solute is a strong function of the dispersivity, with values for position 2W of 69.0 ky, 44.9 ky, and 38.6 ky

Table 7-5. Arrival Times and Effective Retardation Factors for a Conservative Solute and ^{237}Np, 1 mm/y Uniform Infiltration, Different Dispersivities

5% Arrival Position	Conservative Time, ky	^{237}Np Time, ky	5% ERF
2W, α = 0 m	69.0	750	10.9
2W, α = 10 m	44.9	372	8.29
2W, α = 25 m	38.6	313	8.11
2E, α = 0 m	51.4	535	10.4
2E, α = 10 m	31.8	228	7.17
2E, α = 25 m	27.8	196	7.05
50% Arrival Position	**Conservative Time, ky**	**^{237}Np Time, ky**	**50% ERF**
2W, α = 0 m	76.0	839	11.0
2W, α = 10 m	75.7	878	11.6
2W, α = 25 m	76.1	864	11.4
2E, α = 0 m	59.8	699	11.7
2E, α = 10 m	59.6	665	11.2
2E, α = 25 m	60.1	639	10.6

DRAFT

for α values of 0, 10, and 25 m, respectively. Increased spreading of the solute front results in earlier arrival of the fastest moving solute. By contrast, the 50% arrival time is almost unaffected by dispersivity, since the centroid of the solute plume is not affected by dispersion.

Examination of Table 7-5 yields similar conclusions for the impact of dispersivity for ^{237}Np. Thus the importance of dispersivity to the transport predictions is a function of which performance measure is used. A travel-time based standard is likely to stress the importance of the fastest moving radionuclide, and the dispersivity will exert a strong influence on the results. Under the scenario of a dosed-based standard, the median arrival time is more important, and dispersivity will consequently be less important.

7.2.6 Migration as a function of assumed value of K_d

As captured by the histogram of K_d values (Figure 2-1), there is uncertainty in the value of the sorption coefficient K_d for ^{237}Np on zeolitic tuffs. This uncertainty translates to differences in the predicted travel time to the water table. The mean value of 2.5 cc/g was used in all of the calculations presented so far. In this section we examine the sensitivity to sorption coefficient by varying K_d in the zeolitic units by one standard deviation (1.4 cc/g) in each direction, from 1.1 to 3.9 cc/g. Table 7-6 shows the results of these calculations. As expected, the travel times and ERF values of ^{237}Np are directly related to the sorption coefficient. Since to a first approximation the radionuclide spends the majority of its time in the zeolitic rocks, changing the K_d value directly impacts the travel time.

Given the range of 50% ERF values from 5 to 19 resulting from varying K_d, one might, in the interest of conservatism, select an ERF value on the low end of the range when assessing the robustness of the geologic barrier for ^{237}Np transport. However, this would probably result in an overly conservative prediction, for the following reason. The many samples collected and measured for ^{237}Np sorption coefficient resulted in a fairly wide range in K_d values. This wide range occurred even for samples from the same well in close proximity to one another. Therefore, it appears that the K_d varies spatially with a very short correlation length, probably due to mineralogic changes in the samples. Therefore, it is very unlikely that an entire zone of zeolitic rock that exhibits small scale differences in K_d behaves as a system with K_d on the low or high end of the range.

One final simulation of the K_d distribution within the unsaturated zone was carried out to examine the sensitivity of ^{237}Np transport to sorption on the welded TSw tuffs and the vitric and devitrified tuffs of the Calico Hills formation. As pointed out by Triay et al. (1994a) there

Table 7-6. Arrival Times and Effective Retardation Factors for a Conservative Solute and ^{237}Np, 1 mm/y Uniform Infiltration, Different Sorption Coefficients

5% Arrival Position	Conservative Time, ky	^{237}Np Time, ky	5% ERF
2W, K_d = 1.1	38.6	161	4.17
2W, K_d = 2.5	38.6	313	8.11
2W, K_d = 3.9	38.6	467	12.1
2W,K_d = 2.5 and 0.2	38.6	407	10.5
2E, K_d = 1.1	27.8	105	3.78
2E, K_d = 2.5	27.8	196	7.05
2E, K_d = 3.9	27.8	288	10.4
2E, K_d = 2.5 and 0.2	27.8	284	10.2
50% Arrival Position	**Conservative Time, ky**	**^{237}Np Time, ky**	**50% ERF**
2W, K_d = 1.1	76.1	398	5.23
2W, K_d = 2.5	76.1	864	11.4
2W, K_d = 3.9	76.1	1431	18.8
2W,K_d = 2.5 and 0.2	76.1	1030	13.5
2E, K_d = 1.1	60.1	301	5.01
2E, K_d = 2.5	60.1	639	10.6
2E, K_d = 3.9	60.1	1029	17.1
2E, K_d = 2.5 and 0.2	60.1	788	13.1

is a discernible amount of sorption of ^{237}Np on some of these rocks, albeit at a significantly lower value of K_d than for the zeolitic rocks. For this simulation we assume the nominal value of 2.5 cc/g for the zeolitic units, and 0.2 cc/g elsewhere. The entries in Table 7-6 labelled K_d = 2.5 and 0.2 indicate that the increase in ^{237}Np travel times due to sorption on the nonzeolitic rocks are quite modest for sorption on the non-zeolitic rocks in the unsaturated zone. The travel times fall within the range of the variations due to the distribution of K_d values for sorption on the zeolitic rocks. An ERF that compares the travel time of the present case to that of sorption only on the zeolitic rock is a numerical measure of the added benefit of including sorption on the nonzeolitic rock. For these simulations such a calculation produces a 5% ERF of 1.29, and a 50% ERF of 1.18 for release point 2W, and a 5% ERF of 1.45, and a 50% ERF of 1.24 for release point 2E. Triay et al. (1994a) concluded that the additional laboratory work required to confirm the sorption values on vitric and devitrified rocks probably would not alter the transport predictions enough to warrant the expense. The low ERF values calculated here confirm this conclusion. Further study of sorption on whole rock samples not

containing zeolites should not be performed. A possible exception is the study of sorption on fracture walls, where large sorption coefficients have been observed.

7.2.7 Migration as a function of assumed extent of zeolitized units

In this section we examine the impact of our assumptions on the extent of the zeolitized units within the Calico Hills on the transport of ^{237}Np. Since the assumed extent of the zeolitic units has the potential to change both the hydrologic and transport characteristics of the system, the stratigraphic representation of the system was rebuilt and a new two-dimensional, Antler Ridge Cross section was generated, using the methods outlined in Section 4.0. Transport calculations of conservative solutes and ^{237}Np were performed at a 1 mm/y uniform infiltration rate to assess the impact of the extent of the zeolitized units on system performance. Table 7-7

Table 7-7. Comparison of transport results for a Conservative Solute and ^{237}Np, 1 mm/y uniform infiltration, maximum zeolite case. Values in () are for the nominal zeolites case.

5% Arrival			
Position	Conservative Time, ky	^{237}Np Time, ky	5% ERF
1W	43.0 (42.3)	485 (346)	11.3 (8.18)
2W	39.0 (38.6)	430 (313)	11.0 (8.11)
3W	37.5 (39.2)	391 (306)	10.4 (7.81)
1E	32.4 (32.5)	226 (222)	6.98 (6.83)
2E	28.0 (27.8)	192 (196)	6.86 (7.05)
3E	26.9 (26.2)	157 (154)	5.84 (5.88)
50% Arrival			
Position	Conservative Time, ky	^{237}Np Time, ky	50% ERF
1W	84.6 (81.9)	1300 (902)	15.4 (11.0)
2W	77.7 (76.1)	1190 (864)	15.3 (11.4)
3W	74.9 (77.5)	1080 (831)	14.4 (10.7)
1E	68.7 (69.0)	690 (716)	10.0 (10.4)
2E	60.7 (60.1)	624 (639)	10.3 (10.6)
3E	58.4 (57.1)	509 (500)	8.72 (8.76)

compares the travel times and ERF values for a conservative solute and ^{237}Np for the nominal and maximum zeolite extent stratigraphic models. The 5% and 50% arrival times of the conservative solute are virtually identical for the two representations of the Calico Hills. This indicates that differences in the *flow* characteristics of these two models are negligible below the potential repository, despite the changes in the hydrologic characteristics of the zeolitized units.

DRAFT

Because of sorption, transport of ^{237}Np is more sensitive than conservative solute transport to the representation of the zeolitic units. Transport times and ERF values are significantly larger for the maximum zeolite case for all release points on the Western segment of the potential repository. However, for release points on the Eastern segment, the two models yield virtually identical ^{237}Np transport times. Examination of Figure 4-2 shows why this is the case. The largest differences in thicknesses of the zeolitized units occurs in the Western half of the model domain (beneath the Western segment of the potential repository). By contrast, the thickness of the single zeolitized unit that exists between the potential repository and the water table beneath the Eastern segment is approximately the same for the two models.

This agreement of the qualitative observation with the numerical simulations on this cross section justifies a qualitative examination of the entire three-dimensional model domain to compare the impact of zeolite thickness on ^{237}Np transport. Figure 7-9 shows plan views of the sum of the thicknesses of all zeolitic Calico Hills units. These figures were generated from the original hydrostratigraphic structural models using Stratamodel. Figure 7-9a is the zeolite thickness profile for the nominal case, Figure 7-9b is the same profile for the maximum zeolite case, and Figure 7-9c is the difference between the two. For the purposes of this discussion, the simplified conceptual model of transport is one of uniform, downward flow and transport. Therefore, the thickness profile can, under this conceptual model, be viewed as a proxy for retardation of ^{237}Np. For the nominal case, the results of both the two-dimensional Antler Ridge simulations (discussed above) and the North-South cross section ^{237}Np simulations can be understood with reference to Figure 7-9a. Along the North-South cross section, the zeolite thickness profile for the nominal case is quite flat, with a maximum occurring near the middle release point. The ERF values from the simulations, a measure of the benefit due to sorption, also are higher for this point than for the South or North point.

Figure 7-9c represents the additional benefit provided by ^{237}Np sorption if it can be convincingly demonstrated that the maximum zeolite case is valid. For the Western segment of the potential repository, there would be a significant positive impact on ^{237}Np travel times (longer predicted times) if the maximum zeolites case could be confirmed. This is especially true for ^{237}Np release points in the South and West portion of this part of the repository. Additional site characterization work in this region to pin down the total zeolite thicknesses would appear to be warranted. By contrast, there appears to be little impact on release points in the Eastern segment of the potential repository, since there is little or no difference in the zeolite thicknesses for the nominal and maximum zeolite cases. Part of the reason for the thinning of the zeolitic layers to the East is the overall dipping of the hydrogeologic units

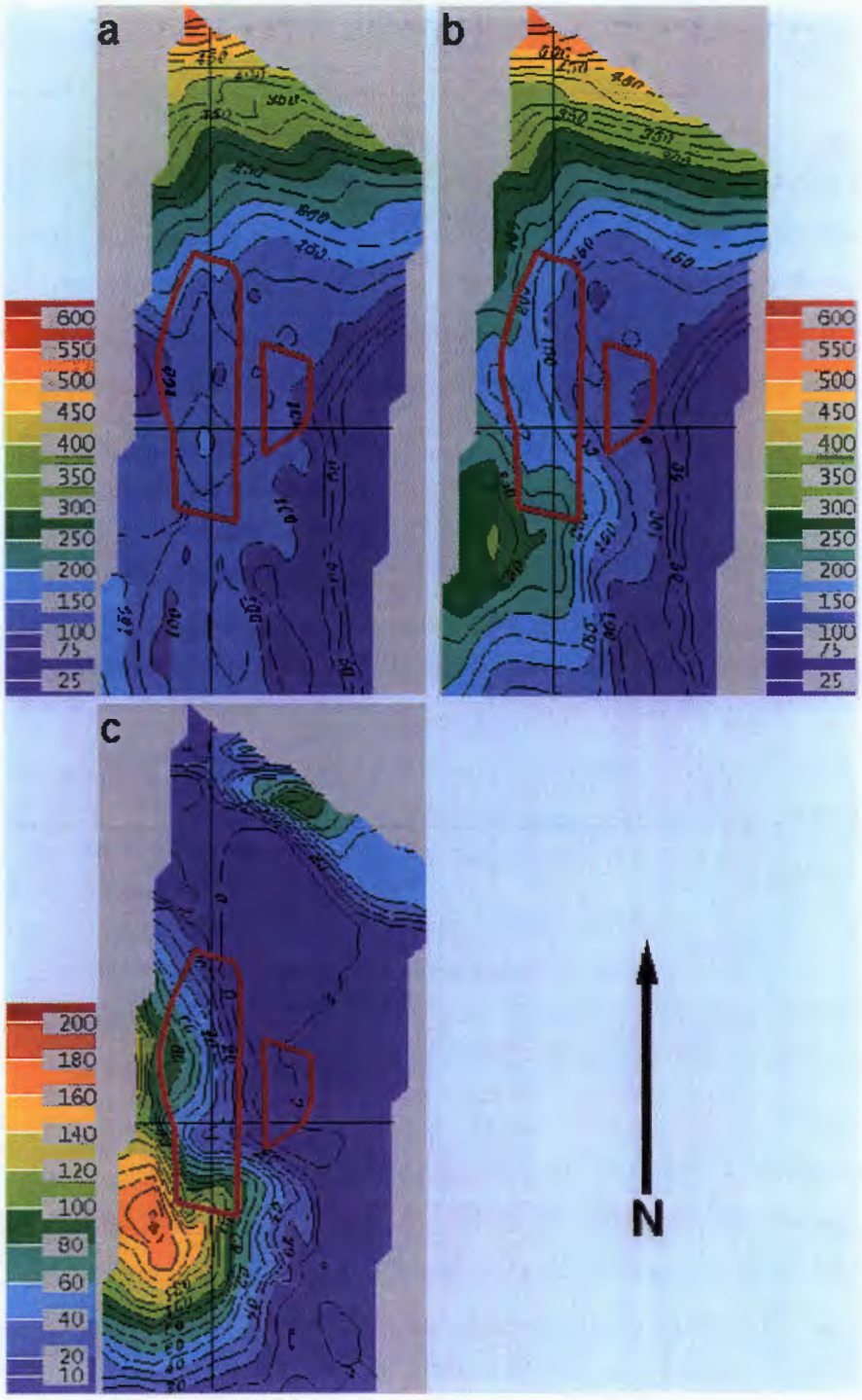

Figure 7-9. Sum of the thicknesses of all zeolitic Calico Hills units. Top figure: nominal case; Middle figure: maximum zeolites case; Bottom figure: difference between the maximum and nominal zeolites case.

DRAFT

superimposed on a relatively flat water table. The units that are zeolitic in the unsaturated zone are actually below the water table in the Eastern section of the model domain. Therefore, the unsaturated zone ^{237}Np transport model yields less sorption retardation for release points in the Eastern segment.

One other important point to consider is that although this is an unsaturated zone model, transport of ^{237}Np will not terminate at the water table. Since there is likely to be ample clinoptilolite and other sorptive minerals below the water table to retard the movement of ^{237}Np, it is premature to ignore the delay in migration experienced in the saturated zone, or to conclude from unsaturated zone modeling alone that the Western segment of the potential repository makes better use of the retardation of the geologic barrier than does the Eastern section.

7.3 3-Dimensional Equivalent Continuum Calculations

Although the two-dimensional calculations presented in Section 7.2 (equivalent continuum) and Section 7.4 (dual permeability) represent the majority of the ^{237}Np transport sensitivity analyses of the present study, it is clear that the development of an accurate site scale flow and transport model requires the use of selected three-dimensional simulations. The goal of the three-dimensional calculations is to examine whether the specific two-dimensional cross sections utilized in the present study provide reasonable transport results. Lateral flow or other three-dimensional effects may not be reproducible in two dimensions. The discussion of the two- and three-dimensional ^{36}Cl simulations presented in Section 6.7 suggest that there are three-dimensional effects on the flow field that are not well reproduced in two dimensions. In this section, three-dimensional equivalent continuum calculations on the 51,000 node finite element grid are performed to identify discrepancies and assess the validity of two-dimensional transport sensitivity analyses.

Figure 4-3 showed a plan view of the three-dimensional model domain with the release positions for the radionuclide migration calculations. Table 7-8 lists the arrival times and ERF values for conservative solutes and ^{237}Np in the 1 mm/y, three-dimensional simulation. For comparison, shown in parentheses are the corresponding travel times and ERF values obtained from the closest release position on either the North-South or Antler Ridge cross section. The most noticeable difference in the calculations is the longer travel times obtained in the three-dimensional simulations. For example, the 50% ^{237}Np travel times do not exist for any of the release positions on the Western segment of the potential repository, even at 1 mm/y infiltration rate (radioactive decay reduces the amount of released ^{237}Np to less than 50% of the injected value). For the release points in the Eastern segment, travel times are much shorter than in the Western segment, especially the 5% arrival time of ^{237}Np. The earliest arriving ^{237}Np appears to miss the zeolitic units, as

Table 7-8. Comparison of transport results for a Conservative Solute and ^{237}Np, 1 mm/y uniform infiltration, three-dimensional simulations. Values in () are for points at the same locations in the East-West or North-South simulations.

5% Arrival Position	Conservative Time, ky	^{237}Np Time, ky	5% ERF
1W	167 (61.0)	791 (588)	4.74 (9.64)
2W	290 (69.0)	2650 (750)	9.14 (10.9)
3W	457 (68.8)	4020 (685)	8.80 (9.96)
1E	156	235	1.51
2E	139 (51.4)	207 (535)	1.49 (10.4)
50% Arrival Position	**Conservative Time, ky**	**^{237}Np Time, ky**	**50% ERF**
1W	277 (70.1)	>10000 (45%) (764)	N/A (10.9)
2W	418 (76.0)	>10000 (24%) (839)	N/A (11.0)
3W	639 (75.7)	>10000 (15%) (780)	N/A (10.3)
1E	251	2880	11.5
2E	270 (59.8)	3280 (699)	12.1 (11.7)

evidenced by the low 5% ERF values (of order 1.5) for release positions 1E and 2E. By contrast, the 50% ERF values are of order 11 to 12 for points 1E and 2E, implying that although the fastest moving ^{237}Np from the Eastern segment does not contact significant zeolites, the central tendency of the plume is one in which the zeolitic tuffs are being contacted.

This analysis implies that there are three-dimensional effects due to differences in the flow distribution that are not fully captured in the two-dimensional simulations. First, given that travel times for both conservative and sorbing radionuclides are in general considerably greater in the three-dimensional simulations, lateral flow above the potential repository is much more prevalent in three dimensions. Recall from Figure 6-17 the pathway taken by fluid injected at a location in the Northern part of the model domain. Significant lateral diversion of flow occurs, with the fluid traveling East and to a lesser extent to the South. Therefore, the flux through the potential repository is much lower than the 1 mm/y entering at the surface, and in fact considerably lower than in the two-dimensional, equivalent continuum simulations.

Next, we examine the migration of a conservative solute and ^{237}Np from a release location in the Western segment of the potential repository. Figure 7-10 shows the results for a centrally located release point. In both cases, the conservative solute and ^{237}Np concentrations are shown at the time at which 5% of the released conservative solute has reached the water table. Significant

DRAFT

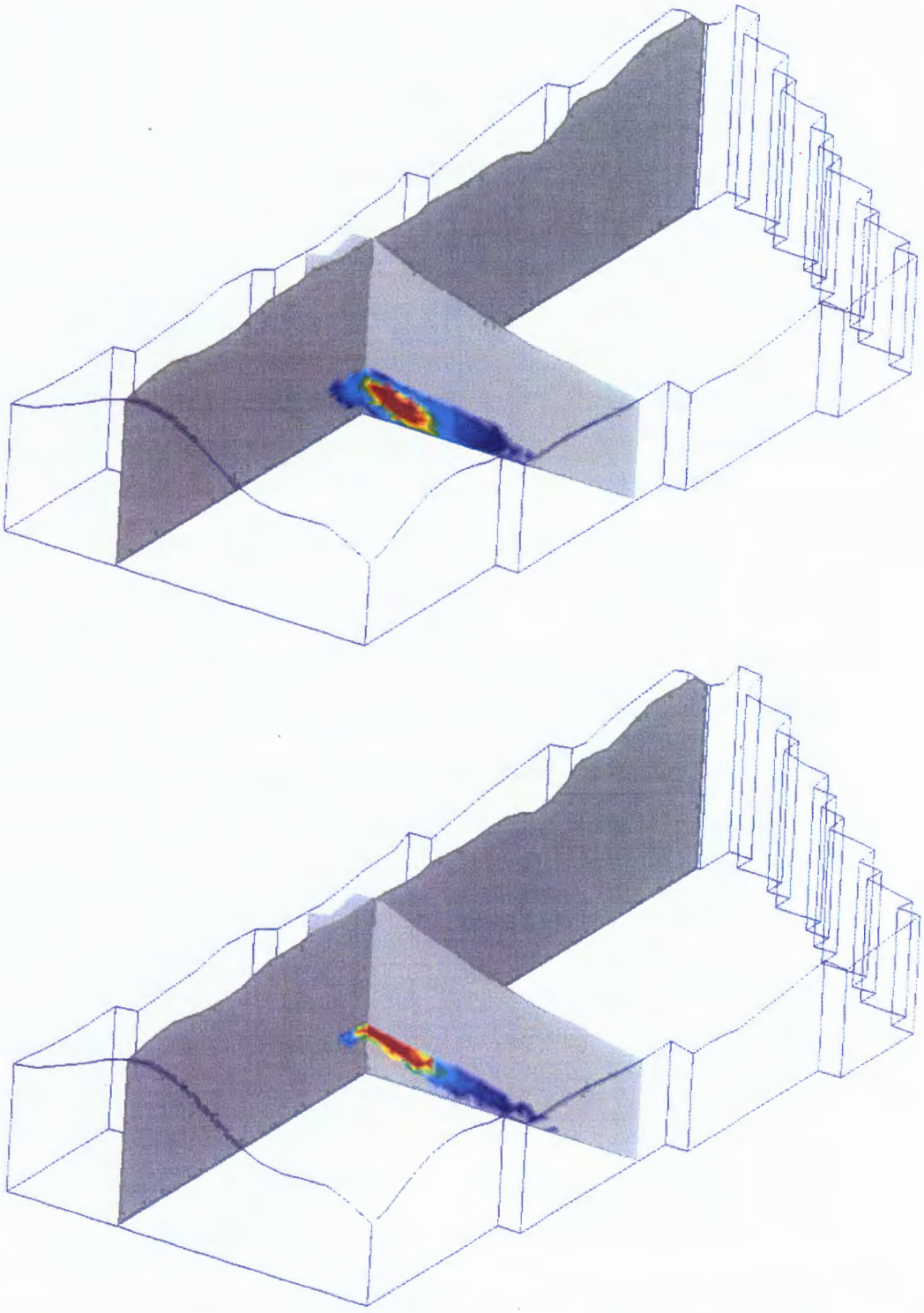

Figure 7-10.Concentration distributions for a conservative radionuclide and ^{237}Np for a release position in the middle of the Western Segment of the potential repository. Concentrations are drawn at the time at which 5% of the conservative solute reaches the water table.

DRAFT

lateral transport occurs from this release position to the East and South, resulting in longer travel times than for the Northern release point. The difference in concentration pattern for the conservative solute and ^{237}Np is also very noticeable in Figure 7-10: the abrupt cutoff in the concentration distribution for ^{237}Np coincides with the zeolitic rock that sorbs ^{237}Np strongly. By contrast, release points in the North exhibit essentially vertical flow and transport.

Clearly, three-dimensional calculations illuminate aspects of the flow and transport system that are not observed in two-dimensional analyses. Further work is required to identify precisely the structural controls on the three-dimensional system that give rise to the complex transport patterns observed in the simulations. However, the fundamental flow and transport processes involved are similar in two or three dimensions. Therefore, the finely resolved two-dimensional simulations in which variations of a given parameter such as K_d should exhibit the correct trends, even if the exact values for travel times are different than the three-dimensional simulations.

Ideally, all sensitivity analyses would be performed in three dimensions. This seems possible for examining moisture distributions and flow patterns using FEHM, since simulations using 50,000 or even larger numbers of nodes is practical. However, for transport calculations, even more finely resolved grids are needed. Until grid resolutions of say 500,000 nodes are practical, a combination of two- and three-dimensional simulations will be necessary to study the flow and transport system.

7.4 2-Dimensional Dual Permeability Calculations

7.4.1 Rationale for dual permeability calculations

The equivalent continuum model calculations presented in Section 7.2 provide a basis for assessing the transport of ^{237}Np and conservative solutes in the unsaturated zone. One of the key assumptions of the equivalent continuum approach is that solute travels through the entire fluid volume associated with the grid block. Even though the flow model accounts for both fracture and matrix flow, solute that originates in the fractures is assumed to have enough time to diffuse fully into the matrix block, so that the concentration in the fractures and matrix are equal, analogous to the equilibration of pressure in the equivalent continuum flow model.

However, this assumption is difficult to justify under conditions of significant fracture flow, given the following order-of-magnitude calculation. The characteristic diffusion time τ_{diff} is of order S^2/D_{AB}, where S is the fracture half-spacing and D_{AB} is the molecular diffusion coefficient. If the transport time within the fractures is not at least as large as τ_{diff}, then the assumption embodied in the equivalent continuum model is invalid. For S = 0.5 m and

D_{AB} = 10^{-11} m^2/s, the characteristic diffusion time is 792 y. Thus, under conditions of fracture flow it is difficult to justify the assumption of equilibration of concentration between fractures and matrix.

The dual permeability model, with its explicit consideration of a fracture network with continuum properties coupled to an additional continuum to represent the matrix rock, circumvents the problems associated with the equivalent continuum approach. Of course, more explicit consideration of the role of individual fractures could be attempted using a discrete fracture model. However, the data needs for such a model and the computational requirements make it impractical for site scale model calculations. Such a model is more appropriate for simulations of block experiments for which fractures are mapped, or in numerical studies that test the validity of the assumptions of simpler models. The dual permeability formulation is a compromise between the need to account for the role of fractures and computational and data needs.

7.4.2 Dual Permeability transport model options

Both a dual permeability finite element transport solution and a particle tracking option are available in FEHM. These two model formulations employ different assumptions for simulating the interaction of solutes between the fractures and matrix that are valid under different conditions. Therefore, both models are used in the present study to simulate the transport of conservative solutes and ^{237}Np. The finite element solution accounts for advective transport between the continua as well as transport via molecular diffusion. However, the steep concentration gradients that are likely to exist adjacent to a fracture will not be reproduced with the finite element transport model because only a single node is used to characterize the matrix. Therefore, the only cases that we can expect to be simulated accurately are those in which the diffusional time constant based on the fracture spacing τ_S is of the same order or less than the advective time constant within the fracture τ_{fr}, that is

$$\tau_S = \frac{S^2}{D_{AB}} \leq \tau_{fr} \tag{7-2}$$

In cases of rapid flow within fractures this criterion will not hold. Alternatively, the particle tracking model is employed to simulate transport of radionuclides. A hybrid model may be set up whereby for dual permeability, advective movement of solute with the flowing fluid is simulated, while matrix diffusion is included as a separate term. In Section 5.2.2, the matrix diffusion particle tracking model was presented in the context of an equivalent continuum

approach in which the travel time of a particle is adjusted to account for matrix diffusion. In dual permeability, we apply this model to particles traveling in the fractures, while matrix transport is treated using the advective-dispersion particle tracking option. Thus, a particle traveling through the fracture continuum can either flow into the matrix by advective movement, or travel through the fracture with a residence time controlled by the advective-dispersion model with matrix diffusion. The inherent assumption of the matrix diffusion transfer function is that the solute has insufficient time to diffuse fully to the center line between the fractures. Recall that this is the opposite of the assumption of the finite element dual permeability solution. The two transport model options allow us to examine the sensitivity of the predictions to extremes in the rate of diffusive transport between the two continua.

7.4.3 Comparison of dual permeability and equivalent continuum transport results

Before embarking on a series of dual permeability model predictions for ^{237}Np transport, we first present a comparison of the predicted radionuclide migration behavior for the two model formulations. To compare to previously discussed equvalent continuum simulations, a series of dual permeability calculations were performed at a uniform infiltration rate of 1 mm/y on the 8000 node Antler Ridge cross section. The grid, hydrologic parameters, and release points for radionuclides are identical for the two cases. Differences in the transport model predictions result from the changes in the flow field as a result of the different model formulation and any differences in the transport model. To keep the non-flow related transport models as close as possible for this comparison, the finite element dual permeability was used instead of the particle tracking. A diffusion coefficient of 10^{-11} m^2/s was applied for the fracture-matrix diffusive transport term, which is large enough to force an equilibration of the concentrations in the two media at a given position. Table 7-9 compares the transport times and ERF values for the two model formulations. Recall from Section 6.5.2 that in the Western segment of the potential repository, lateral flow diverts water above the Westernmost release points in dual permeability. The result is longer travel times of conservative solutes and ^{237}Np than for the equivalent continuum model. As discussed in the previous section, some of this flow proceeds downward before it reaches the Ghost Dance fault. Thus, radionuclide released at point 3W travels significantly faster than radionuclides released at points 1W or 2W. To the East of the fault, a similar trend exists, with transport times for 1E greater than those from 3W, but declining significantly when the release point is moved further East. The Easternmost release point (point 3E) experiences enough of a a downward flux to make the dual permeability transport times equal to that of the equivalent continuum model values. Thus values of similar magnitudes are obtained, but there is a greater dependence on release position in the dual

Table 7-9. Comparison of transport results for the equivalent continuum (in parentheses) and dual permeability formulations for a Conservative Solute and ^{237}Np, 1 mm/y uniform infiltration.

5% Arrival Position	Conservative Time, ky	^{237}Np Time, ky	5% ERF
1W	83.9 (42.3)	647 (346)	7.71 (8.18)
2W	190 (38.6)	1580 (313)	8.32 (8.11)
3W	40.0 (39.2)	288 (306)	7.20 (7.81)
1E	65.5 (32.5)	382 (222)	5.83 (6.83)
2E	49.0 (27.8)	306 (196)	6.24 (7.05)
3E	23.1 (26.2)	147 (154)	6.36 (5.88)
50% Arrival Position	**Conservative Time, ky**	**^{237}Np Time, ky**	**50% ERF**
1W	184 (81.9)	2840 (902)	15.4 (11.0)
2W	364 (76.1)	6510 (864)	17.9 (11.4)
3W	87.2 (77.5)	969 (831)	11.1 (10.7)
1E	141 (69.0)	1380 (716)	9.79 (10.4)
2E	106 (60.1)	1120 (639)	10.6 (10.6)
3E	52.5 (57.1)	489 (500)	9.31 (8.76)

permeability model, a consequence of the increased lateral flow above the potential repository and enhanced downward flux near the Ghost Dance fault and the rightmost boundary of the model domain.

The ERF values for ^{237}Np transport are of similar magnitude for the equivalent continuum and dual permeability models, indicating that the main differences in the dual permeability transport predictions are caused by differences in the flow distribution. This conclusion is not surprising, given that the diffusion coefficient governing transport between fractures and matrix was set to approximate equivalent concentrations in the two media at a given location. Simulations presented later using particle tracking will relax this assumption.

7.4.4 Dual permeability model transport results

A full suite of dual permeability calculations were performed at the infiltration rates of 0.1, 1, and 4 mm/y (the 1 mm/y calculations were discussed in the previous section), and the impact of assumed extent of the zeolitic rocks in the Calico Hills units were also examined. Tables 7-10 and 7-11 tabulate the results of the infiltration rate simulations, comparing the travel times and ERF values with those of the equivalent continuum model. The conclusions described for the 1 mm/y comparison also apply at higher and lower infiltration rates:

Table 7-10. Comparison of transport results for the equivalent continuum (in parentheses) and dual permeability formulations for a Conservative Solute and ^{237}Np, 0.1 mm/y uniform infiltration.

5% Arrival Position	Conservative Time, ky	^{237}Np Time, ky	5% ERF
1W	690 (358)	2.4% (4370)	N/A (12.2)
2W	997 (325)	.73% (3750)	N/A (11.5)
3W	668 (305)	4.1% (3120)	N/A (10.2)
1E	393 (283)	4332 (2470)	11.0 (8.73)
2E	393 (229)	3937 (1950)	10.0 (8.52)
3E	360 (213)	2502 (1480)	6.95 (6.95)
50% Arrival Position	**Conservative Time, ky**	**^{237}Np Time, ky**	**50% ERF**
1W	>1000 (734)	2.4% (11%)	N/A (N/A)
2W	>1000 (668)	.73% (13%)	N/A (N/A)
3W	>1000 (628)	4.1% (16%)	N/A (N/A)
1E	875 (620)	16% (19%)	N/A (N/A)
2E	874 (515)	17% (23%)	N/A (N/A)
3E	829 (489)	24% (29%)	N/A (N/A)

- for dual permeability, lateral diversion of flow results in lower flux rates through the potential repository and concomitant larger travel times, except near the Ghost Dance fault and the Easternmost release point, where downward flow is forced due to the stratigraphic impact of the fault and/or the influence of the Eastern boundary of the model domain, and;
- similar ERF values for ^{237}Np are obtained for dual permeability, implying that the choice of model formulation does not influence the extent to which the zeolitic units retard the movement of ^{237}Np relative to that of a conservative solute.

Beyond these conclusions, the impact of infiltration rate on transport is shown in the tables. At the 0.1 mm/y infiltration rate, there is a low enough flux through the potential repository to significantly limit the releases at the water table. In many cases the 50% or even the 5% arrival times are not even reached; for these cases the percent of ^{237}Np reaching the water table after 10 my is given. For all release points in the Western segment of the potential repository, less than 5% of the release ^{237}Np even reaches the water table. Radioactive decay reduces the ^{237}Np concentrations significantly during the migration through the unsaturated zone. Although the 5% arrival times are finite for all positions in the Eastern segment, 50% travel times are all large enough to limit the fraction reaching the water table to 29% or less. Thus under these conditions the dual permeability model predicts reductions in the quantities reaching the water

DRAFT

Table 7-11. Comparison of transport results for the equivalent continuum (in parentheses) and dual permeability formulations for a Conservative Solute and ^{237}Np, 4 mm/y uniform infiltration

5% Arrival			
Position	Conservative Time, ky	^{237}Np Time, ky	5% ERF
1W	18.4 (11.4)	132 (81.8)	7.17 (7.18)
2W	15.8 (10.3)	112 (72.9)	7.09 (7.08)
3W	8.37 (10.2)	49.8 (71.3)	5.95 (6.99)
1E	11.9 (8.12)	76.1 (50.7)	6.39 (6.24)
2E	6.64 (6.86)	37.5 (43.4)	5.65 (6.33)
3E	5.94 (6.16)	29.7 (33.2)	5.00 (5.39)
50% Arrival			
Position	Conservative Time, ky	^{237}Np Time, ky	50% ERF
1W	38.2 (22.2)	306 (198)	8.01 (8.92)
2W	30.6 (20.5)	264 (193)	8.63 (9.41)
3W	17.2 (20.2)	148 (185)	8.60 (9.16)
1E	25.5 (17.5)	229 (159)	8.98 (9.09)
2E	15.3 (15.0)	138 (140)	9.02 (9.33)
3E	13.9 (13.8)	112 (112)	8.06 (8.12)

table. At 4 mm/y, all travel times are reduced essentially in proportion to the ratio of the infiltration rates.

Results of dual permeability simulations comparing the nominal and maximum zeolite cases are shown in Table 7-12. As in the equivalent continuum model comparison discussed in Section 7.2.7, the differences in the representation of the extent of the zeolitized Calico Hills units has almost no impact on the migration of the conservative solute. By contrast, the transport of ^{237}Np is impacted by the stratigraphic representation of the Calico Hills units. For release positions in the Western segment of the potential repository, ^{237}Np transport is delayed to a greater degree in the maximum zeolite case, while releases in the Eastern segment show little difference from the nominal case. The discussion presented in Section 7.2.7 on the sums of the thicknesses of the zeolitized units and its impact on ^{237}Np transport apply to these dual permeability results as well.

7.4.5 Migration as a function of diffusion coefficient

Diffusion into the rock matrix is a transport process that impacts the migration of radionuclides in cases in which fracture flow and transport is important. When solute diffuses from a fracture into the matrix, the velocity of movement in the direction of flow decreases

Table 7-12. Comparison of transport results for the nominal (in parentheses) and maximum zeolite cases, 1 mm/y uniform infiltration, dual permeability model.

5% Arrival Position	Conservative Time, ky	^{237}Np Time, ky	5% ERF
1W	82.8 (83.9)	902 (647)	10.9 (7.71)
2W	205 (190)	2530 (1580)	12.3 (8.32)
3W	36.0 (40.0)	333 (288)	9.25 (7.20)
1E	63.2 (65.5)	372 (382)	5.89 (5.83)
2E	50.0 (49.0)	301 (306)	6.02 (6.24)
3E	23.4 (23.1)	149 (147)	6.37 (6.36)
50% Arrival Position	**Conservative Time, ky**	**^{237}Np Time, ky**	**50% ERF**
1W	182 (184)	(47%) (2840)	N/A (15.4)
2W	400 (364)	(22%) (6510)	N/A (17.9)
3W	80.0 (87.2)	1200 (969)	15.0 (11.1)
1E	137 (141)	1240 (1380)	9.05 (9.79)
2E	109 (106)	1100 (1120)	10.1 (10.6)
3E	53.4 (52.5)	495 (489)	9.27 (9.31)

dramatically, and travel times increase. Furthermore, diffusion provides a mechanism for radionuclides to contact the matrix rock, where sorption-induced retardation can take place.

In the present study, the dual permeability model formulation allows us to examine the impact of diffusion on the transport characteristics of conservative solutes and ^{237}Np. Under conditions in which fracture flow is important, the particle tracking model may be used with matrix diffusion applied to solute traveling in the fractures (the so-called "hybrid" transport model described in Section 7.4.2). When fluid moves from fractures to matrix, say, at the contact between a unit with large fracture flow and one with predominantly matrix flow, the advective flow term of the particle tracking model dominates. This transport model option is ideal for examining the effect of the diffusion coefficient, as long as the criterion for the validity of the matrix diffusion transport model is satisfied (Eqn. 7-2), namely, that the time required for diffusion to the centerline of two fractures in the fracture continuum is long compared to the advective transport time within the fracture. This necessitates the restriction that only the highest infiltration rates be studied using the particle tracking hybrid transport model.

A series of transport simulations were carried out using the 4 mm/y, dual permeability flow solution computed on the 8000 node, Antler Ridge cross section to examine the effect of matrix

diffusion on transport. Table 7-13 shows the travel times resulting from these simulations. The first two columns are the 5% or 50% travel times to the water table for a conservative solute, the first with no matrix diffusion, the second with an assumed diffusion coefficient of 10^{-11} m^2/s. Notice first that the transport times to the water table using the hybrid transport model are significantly shorter than the values for the 4 mm/y equivalent continuum model or the dual permeability, finite element transport solution (these results are summarized in Table 7-14).

This is to be expected since the previous simulations used either the equivalent continuum model or, for dual permeability, applied a diffusion coefficient large enough to allow solute to spread rapidly between the fracture and matrix continua. Thus the effective volumetric water content, which directly scales the transport time at a given flux, is of the order of the matrix volumetric water content, rather than the much smaller fracture water content. The particle tracking dual permeability travel time results are probably more indicative of the true transport times to the water table *at infiltration rates sufficient to sustain fracture flow.*

Table 7-13. Transport results examining the effect of matrix diffusion on conservative solute and ^{237}Np travel times, 4 mm/y uniform infiltration, dual permeability model

5% Arrival Position	Conservative Time, ky (D_{AB} = 0)	Conservative Time, ky (D_{AB} = 10^{-11} m^2/s)	^{237}Np Time, ky (D_{AB} = 10^{-11} m^2/s)	5% ERF
1W	24.5	27.5	279	10.1
2W	13.7	16.9	167	9.88
3W	4.09	4.98	15.5	3.11
1E	3.51	6.57	73.2	11.1
2E	661 days	0.67	11.8	17.6
3E	606 days	0.25	6.07	24.3
50% Arrival Position	**Conservative Time, ky (D_{AB} = 0)**	**Conservative Time, ky (D_{AB} = 10^{-11} m^2/s)**	**^{237}Np Time, ky (D_{AB} = 10^{-11} m^2/s)**	**50% ERF**
1W	38.4	41.8	467	11.2
2W	28.9	31.8	427	13.4
3W	13.5	15.5	234	15.1
1E	20.7	22.9	357	15.6
2E	6.50	14.7	291	19.8
3E	5.26	11.3	202	17.9

DRAFT

Table 7-14. Transport results examining the effect of matrix diffusion coefficient on ^{237}Np travel times, 4 mm/y uniform infiltration, dual permeability model

5% Arrival	
Position and D_{AB} value	^{237}Np Time, ky
2W, ($D_{AB} = 10^{-10}$ m^2/s)	258
2W, ($D_{AB} = 10^{-11}$ m^2/s)	167
2W, ($D_{AB} = 10^{-12}$ m^2/s)	72.0
2E, ($D_{AB} = 10^{-10}$ m^2/s)	67.9
2E, ($D_{AB} = 10^{-11}$ m^2/s)	11.8
2E, ($D_{AB} = 10^{-12}$ m^2/s)	1.62
50% Arrival	
Position	^{237}Np Time, ky
2W, ($D_{AB} = 10^{-10}$ m^2/s)	522
2W, ($D_{AB} = 10^{-11}$ m^2/s)	427
2W, ($D_{AB} = 10^{-12}$ m^2/s)	411
2E, ($D_{AB} = 10^{-10}$ m^2/s)	367
2E, ($D_{AB} = 10^{-11}$ m^2/s)	291
2E, ($D_{AB} = 10^{-12}$ m^2/s)	88.5

Further examination of the conservative solute results of Table 7-13 shows that matrix diffusion has a relatively small impact on the travel times of a conservative solute, except for release points 2E and 3E, for which the extremely low transport times of 661 days and 606 days in the absence of diffusion are mitigated by diffusion. For these two release points, the reason that the 5% arrival times for the conservative solute without matrix diffusion are so small is that a fraction of the released solute is traveling through fractures continuously from the potential repository to the water table. Significantly larger travel times are determined for all other release points, but for these other points matrix diffusion does little to lengthen the travel times. This behavior can be explained by the fact that the vitric and devitrified units are dominated by matrix flow and transport even at the infiltration rate of 4 mm/y. For the conservative solutes the transport times to the water table are heavily influenced by the slow migration in these units, and the relatively rapid travel through fractures in the zeolitized units are a minor contributor. Since significant thicknesses of vitric and devitrified tuffs underlay the Western release points, longer travel times are computed.

DRAFT

The ^{237}Np transport results for a matrix diffusion coefficient value of 10^{-11} m^2/s are also shown in Table 7-14. Since sorption is only non-zero in these calculations for the rock matrix, the significant retardation compared to the conservative solute indicates that matrix diffusion serves to carry ^{237}Np into the rock matrix of the zeolitic units. This fact is better seen in Table 7-14,which shows the role of matrix diffusion for the transport of ^{237}Np. The critical issue for migration of ^{237}Np or any other sorbing radionuclide under conditions of fracture flow is whether or not the molecular diffusion transport mechanism allows radionuclide to contact the sorptive minerals in the matrix rock. Clearly, in these simulations, diffusion of ^{237}Np is rapid enough to allow sorption and retardation to take place, as evidenced by the large ERF values obtained in Table 7-13.

7.4.6 Migration as a function of fracture sorption

As presented in Section 2.4.3, ^{237}Np has been shown to sorb to the walls of natural fractures in Yucca Mountain tuff samples. This dual permeability particle tracking transport model allows us to examine the effectiveness of sorption on fracture walls relative to sorption on the matrix rock. The experiment analyzed in Section 2.4.3 yielded a retardation factor in the fracture of order 70. This value was used as a starting point for this retardation sensitivity analysis. For all transport runs in this analysis, the diffusion coefficient in the matrix rock was 10^{-11} m^2/s, and for each ^{237}Np calculation, sorption was assumed in the matrix with a K_d of 2.5 cc/g. Table 7-15 indicates that including fracture sorption with a retardation factor of 70 has almost no effect on the ^{237}Np travel times. The differences are so small that they can be attributed to slight inaccuracies in the method for outputting and postprocessing the particle tracking information, and thus should not be considered to be real effects.

The reason that fracture sorption has no impact on the ^{237}Np travel times in these simulations is best understood by examining the matrix diffusion model with sorption (Eqn. (2-3)). The relative importance of fracture and matrix sorption can be illustrated by assigning parameter values typical to those for the zeolitized units and examining the results. For this one-dimensional calculation, the following values were used:

- fracture residence time - 0.1 y
- matrix porosity - 0.3
- matrix diffusion coefficient - 10^{-11} m^2/s
- matrix retardation factor - 20
- fracture retardation factor - 1 or 70

Figure 7-11 shows that, like the site scale model results, including fracture sorption has very little effect on the breakthrough of solutes, except for slight differences for the earliest part of

Table 7-15. Transport results examining the impact of fracture sorption on ^{237}Np travel times, 4 mm/y uniform infiltration, dual permeability model

5% Arrival Position	Conservative Time, ky	^{237}Np Time, ky No Fracture Sorption	^{237}Np Time, ky Fracture Sorption	5% ERF
1W	27.5	279	279	10.1
2W	16.9	167	167	9.88
3W	4.98	15.5	15.3	3.08
1E	6.57	73.2	73.8	11.4
2E	0.67	11.8	11.8	17.6
3E	0.25	6.07	6.11	23.5
50% Arrival Position	**Conservative Time, ky**	**^{237}Np Time, ky No Fracture Sorption**	**^{237}Np Time, ky Fracture Sorption**	**50% ERF**
1W	27.5	467	467	11.2
2W	16.9	427	427	13.4
3W	4.98	234	234	15.1
1E	6.57	357	357	15.6
2E	0.67	291	291	19.7
3E	0.25	202	201	17.6

the curve. The physical explanation lies in the nature of the matrix diffusion model. When matrix diffusion occurs, solute spends the majority of its time in the matrix, rather than sorbed to the surface of fractures. Only while the solute resides in the fracture is the fracture sorption acting to delay the movement of solute. Thus the magnitude of the fracture sorption effect is of order fracture fluid residence time times the fracture retardation factor, for this example 0.1 y. Compared to the time spent by the solute in the rock matrix, this time is insignificant. Therefore, sorption on the fracture walls is insignificant.

At a large enough fracture retardation factor or a very small matrix diffusion coefficient, sorption on fracture walls would start to contribute significantly to the overall travel time. Figure 7-11 shows a simulation with matrix diffusion and the fracture retardation factor equal to 10000, indicating that only for this high a value will fracture sorption play an important role in retarding the movement of ^{237}Np when matrix diffusion is operative. By contrast, for the case of little or no matrix diffusion, the travel time is increased due to fracture sorption by the full factor of 70, but only from the very small starting point of 0.1 y travel time. The travel time thus is still quite low under this scenario as well.

Of course, we have examined only a single set of flow and transport parameters with a simplistic transport model (and only for ^{237}Np), so it would be premature to rule out the impact of fracture sorption based on these calculations. For example, the matrix diffusion model has a

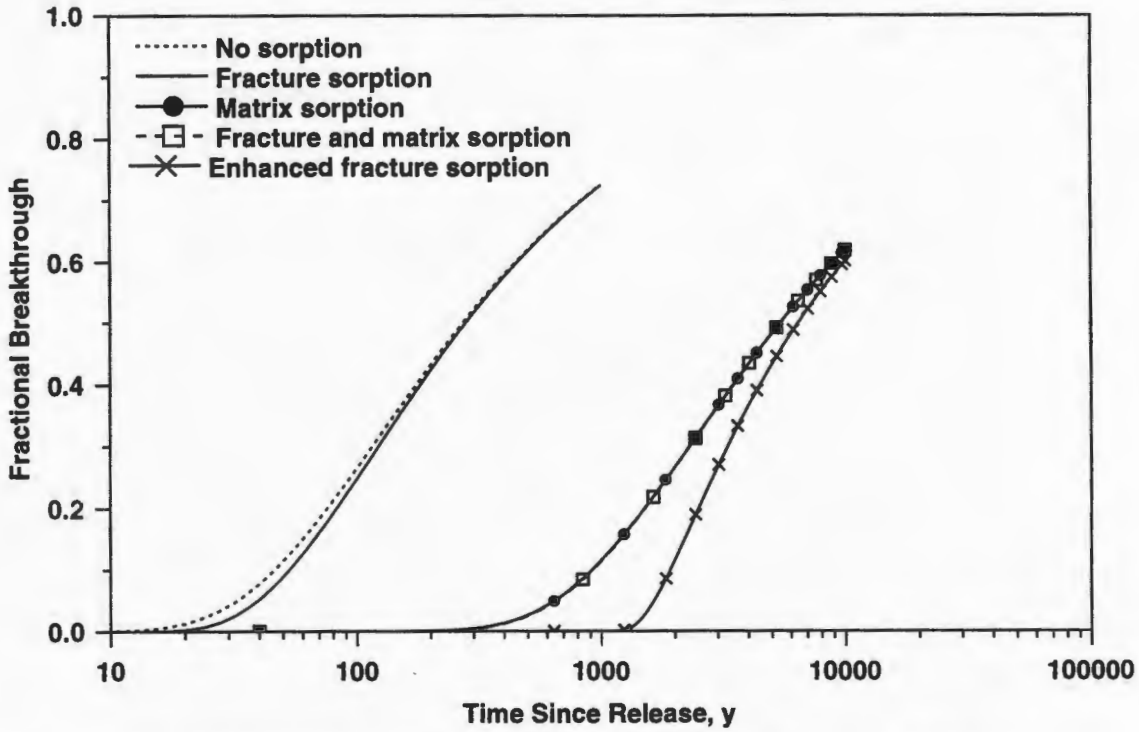

Figure 7-11.Breakthrough curves for a one-dimensional matrix diffusion calculation for parameter values similar to those in the zeolitized Calico Hills units. Simulations with and without matrix diffusion. Curves labeled "fracture sorption" use fracture retardation factor R_f = 70; for "enhanced fracture sorption," R_f = 10000.

rather restrictive view of fracture sorption, treating it as a phenomenon occurring only in the fracture itself. If secondary mineralization with favorable sorptive characteristics is found even a few centimeters into the matrix rock away from a fracture, the benefit of sorption would be enhanced. Nonetheless, there appears to be a rather narrow range of conditions under which fracture sorption is important from a performance perspective. Under conditions in which matrix diffusion is operative, radionuclides quickly diffuse away from the sorptive fracture minerals, spending the bulk of their time in the matrix. Under a scenario of no matrix diffusion, fracture travel times are so low that only extremely sorptive minerals would be likely to have an impact on the performance of the site.

7.4.7 Migration as a function of key uncertainties in hydrologic properties

Although a systematic sensitivity analysis of the impact of uncertainties in hydrologic properties on the transport of ^{237}Np is beyond the scope of the present study, in this section we examine a few key hydrologic uncertainties to demonstrate their effect on transport model

results. Specifically, in one set of calculations we include the Ghost Dance fault as a zone of distinct hydrologic characteristics, and in another suite of runs we alter the nature of fracture/ matrix interaction in the dual permeability model. These sensitivity studies are best thought of as studies of conceptual model uncertainties, rather than as parameter sensitivity analyses, since the parameter values are being changed in such a way as to fundamentally alter the flow characteristics.

Explicitly Modeled Fault. Using the flow field computed in Section 6.5.4, we performed a series of simulations to investigate the effect of explicitly specified fault properties in the Ghost Dance fault on radionuclide migration from the potential repository. In this set of calculations, the hydrologic properties of the Ghost Dance fault are represented using the fracture properties of the TSw units (the most highly fractured units in the model), while the matrix properties are assigned values of the vitric Calico Hills units. In summary, the fault is modeled as a zone of rock 130 m thick, extending from the surface to the water table, with relatively high fracture permeability and properties of the surrounding matrix resembling one of the more permeable hydrogeologic units of the unsaturated zone. Table 7-16 compares the results of conservative solute travel time calculations with the case in which the fault is not explicitly represented. In

Table 7-16. Comparison of conservative solute transport results for flow models with and without the fault explicitly represented, 1 mm/y uniform infiltration, dual permeability model.

5% Arrival		
Position	With fault Time, ky	Without fault Time, ky
1W	83.7	83.9
2W	190	190
3W	41.5	40.0
1E	215	65.5
2E	89.8	49.0
3E	26.5	23.1
50% Arrival		
Position	With fault Time, ky	Without fault Time, ky
1W	185	184
2W	366	364
3W	90.3	87.2
1E	490	141
2E	213	106
3E	60.3	52.5

DRAFT

the Western segment of the potential repository, travel times are not affected by explicitly representing the fault. The overall behavior for the Western segment is quite similar to the base case of no fault present. The overall pattern of flow remains one in which the fault diverts flow downward near it, resulting in short travel times for position 3W compared to points further West. Thus the flow diversion in the dual permeability calculations without the fault explicitly present (due to the undulation of the stratigraphy caused by the fault offset) was similar to that when the fault is explicitly modeled, at least with respect to transport of radionuclides from the potential repository. The Eastern segment release points have markedly larger travel times for the simulations with the fault explicitly represented, however. The Ghost Dance fault acts to divert a greater fraction of the flowing water, resulting in smaller downward flux through the Eastern segment of the potential repository.

This effect was illustrated in Figure 6-11, which showed the movement of a tracer released with the infiltrating fluid at locations to the West of the Ghost Dance fault. The lateral flow above the potential repository is arrested by the presence of the fault, which for these property values acts as a conduit for vertical, downward flow. Since the flow diversion occurs above the potential repository, radionuclide transport from the Western segment is little affected because both simulations in fact show the effect of the fault.

Fracture-Matrix Interaction Effects. In Section 6.5.3 we also examined the effect of the fracture-matrix interaction terms of resulting flow fields and saturations. Namely, depending on how those uncertain terms are specified, fractures may or may not flow in a given unit for a specified infiltration rate. The impact of the different assumptions regarding the onset of fracture flow is shown in the transport results of Table 7-17. Regarding the conservative solute travel times, the change in parameter value resulting in fracture flow at lower matrix saturations results in a system with greater fracture flow and shorter travel times from the potential repository to the water table. Furthermore, the disparity in travel times at different release points within a segment of the repository is much less than for the base case. This behavior can be explained as a more uniform, vertical downward flow with less lateral diversion above the potential repository. Units that in the base case could not support fracture flow at a given matrix saturation value are able to transmit fluid through fractures when the fracture α values are lowered.

For ^{237}Np transport, similar trends are followed, with the largest impact on travel times occurring for release positions where there is the greatest disparity in travel times for the two models. This sensitivity analysis demonstrates the need to calibrate flow and transport models

against chemical data such as environmental isotope data and field scale transport tests using tracers.

Table 7-17. Comparison of arrival times for the base case and low fracture α simulations, 4 mm/y uniform infiltration, dual permeability model

5% Arrival Position	Base Case Conservative Time, ky	Low α Conservative Time, ky	Base Case ^{237}Np Time, ky	Low α ^{237}Np Time, ky
1W	27.5	8.79	279	22.6
2W	16.9	6.98	167	15.6
3W	4.98	4.01	15.5	21.4
1E	6.57	0.913	73.2	7.06
2E	0.67	0.862	11.8	11.9
3E	0.25	0.780	6.07	14.0
50% Arrival Position	**Base Case Conservative Time, ky**	**Low α Conservative Time, ky**	**Base Case ^{237}Np Time, ky**	**Low α ^{237}Np Time, ky**
1W	41.8	26.4	467	365
2W	31.8	25.6	427	308
3W	15.5	24.6	234	436
1E	22.9	16.1	357	141
2E	14.7	15.5	291	249
3E	11.3	14.0	202	262

DRAFT

8.0 Discussion and Conclusions

8.1 Hydrostratigraphic Characterization and Grid Generation

The two- and three-dimensional flow and transport model calculations discussed in the present study are the product of an integrated program of data collection, interpretation, and modeling. Transport calculations require the integration of data and models from various sources, including hydrologic data and models, hydrostratigraphic and mineralogic information, and geochemical experimental data. The result is a site scale, unsaturated zone flow and transport model representing the efforts of scientists of a variety of disciplines on the Yucca Mountain Site Characterization Project.

The starting point for the flow and transport model is the characterization of the hydrostratigraphy and representation of this information in finite element grids. The structural information of the LBL/USGS site scale flow model of Wittwer et al. (1995) was used as a starting point. The major hydrostratigraphic units and sub-units that comprise the model were supplied by scientists at LBL. This input represents a great deal of integration work to construct a realistic structural framework model. One area that we determined needed improvement was the representation of the Calico Hills hydrogeologic units, particularly the relative thicknesses of the vitric, devitrified, and zeolitic sub-units of this important stratigraphic unit. It was determined that the cause of the inaccuracy in the LBL structural model was in applying proportionality rules for sub-dividing the major units. Although this approach is probably adequate for units that do not intersect the water table, treating the water table as the bottom surface forced units that dip below the water table to the East to pinch out unnaturally at the water table. Since the prediction of ^{237}Np transport depends critically on the zeolitic units beneath the potential repository, the Calico Hills units needed to be reconstructed. Input from Los Alamos Min/Pet staff was critical in this characterization effort. It is recommended that this revised representation of the Calico Hills be used in future site scale modeling studies as it represents the latest thinking of the Project's geologists.

The approach employed in the present study for developing accurate representations of the hydrostratigraphic structure employs a series of software tools to proceed from structural information to finite element grids. This integrated approach allows for different representations of the hydrostratigraphy to be created quickly at different spatial resolutions, allowing more aspects of the system to be studied numerically. The first step in the process is to incorporate spatial data on the thickness of each unit into the Stratamodel software package. This software allows a numerical representation of the field data to be generated. The visualization features of this package allows geologists and other scientists to examine the model quickly and judge its adequacy. Changes to the

model to better reflect the intuition of the scientist are made easily. The result is the best possible structural model.

The output from Stratamodel is a description of structure, but not a finite element grid upon which calculations can be performed. The GEOMESH software, developed by Los Alamos scientists, is used to perform this step of the process. This software produces unstructured, two- and three-dimensional finite element grids that can be input directly to FEHM. The grids generated with this software automatically preserve the interfaces between the hydrostratigraphic units, so that if a thin unit exerts control over the hydrologic system, it will be represented as accurately as possible. The other criterion that is satisfied in the generation of the grids is that the Delaunay conditions are satisfied. This requirement is necessary for the finite element simulations using these grids to be accurate and free of grid orientation effects. No such adverse effects have been identified in any of the FEHM calculations. Finally, the GEOMESH software allows the original structural information to be discretized to any level. The grid may be made more finely resolved in areas where finer discretization is needed, such as beneath the potential repository in the present study.

This suite of software packages is a powerful approach to generating finite element grids for flow and transport calculations. In the present study, three-dimensional calculations were performed on three grids: one to reproduce the LBL/USGS model for comparison purposes, one at a somewhat finer spatial resolution than the grid used for comparison, with the new representation of the Calico Hills, and a fine resolution grid with an additional level of discretization in the units beneath the potential repository. In addition, a total of five two-dimensional grids were used: three at different degrees of resolution for the Antler Ridge cross section, one Antler Ridge cross section for the "maximum zeolites" case, and one North-South cross section. The versatility and ease of use of the approach to grid generation used in the present study made this possible.

8.2 Hydrologic Conclusions

The hydrologic analysis section of this report provided the flow fields in which the solute transport sensitivity analyses were performed. It also served to highlight some important processes for consideration. A characteristic that was observed on all flow fields considered was that the saturation distributions followed the stratigraphy. The welded tuffs always had higher saturations than the nonwelded tuffs. These characteristics were found in both the two- and three-dimensional simulations just as they can be found in other three-dimensional models (e.g. Wittwer et al., 1995) and even one-dimensional simulations of unsaturated flow through layered systems such as those described by Ho (1995). However, the hydrologic flow analyses here have demonstrated that the nature of the flow distribution through the variably saturated layered system is strongly dependent on the dimensionality of the problem. Just as one-dimensional systems are characterized as overly

restrictive, or preventative to lateral flow, the results here have demonstrated that the two-dimensional flow systems, too, are restrictive to possible flow paths when compared with three-dimensional simulations. This was demonstrated with simulations of the migration of ^{36}Cl, a naturally occurring radioisotope which can be used to trace the percolation of infiltrating water. For infiltration rates of 1 mm/y, the percolation flux through the two-dimensional domain was great enough to yield a young signal (apparent age), meaning mostly undecayed ^{36}Cl was found at all locations in the cross-section. In the three-dimensional simulations, on the other hand, the infiltrating water followed preferential flow paths and the apparent age distribution in the unsaturated zone spanned a range of over a million years. The flow paths, visualized with fence diagrams of the apparent groundwater ages, are complex and strongly dependent on hydrostratigraphy. In some regions of the domain, primarily vertical flow is observed while in other regions there are clear flow paths channeling younger water to regions underlying older water. These lateral dipping pathways primarily occur at the interface between the Tiva Canyon welded tuff and the Paintbrush welded tuff as well as the generally deeper interface between the Topopah Springs welded tuff and the Calico Hills non welded tuff (a zone occupied by the thin basal vitrophyre).

The complexity of the flow field is also better resolved by implementing the dual permeability model formulation. It is only with this method, which explicitly accounts for fractures, that we were able to simulate the arrival of bomb-pulse ^{36}Cl (and, by inference, Tritium) in the Paintbrush tuff. The dual permeability method provided for rapid fracture flow of the isotopes until arrival in the higher permeability, less fractured nonwelded tuff. This behavior matches the general belief that infiltrating water can move quickly through the fractures of the welded tuff but is then arrested and driven laterally in the nonwelded tuff. However, the dual permeability simulations also identified in the three-dimensional model some pathways leading to deeper units. These generally occurred south of the potential repository and provided for lateral transport across the entire width of the model domain. These simulations of rapid movement of ^{36}Cl through fractured welded tuff in conjunction with the three-dimensional equivalent continuum simulations, which showed down-dip flow, provide encouraging initial indications that hydrologic flow models in conjunction with solute transport models of naturally occurring isotopes will lead to greater confidence in modeling unsaturated flow systems. The dual permeability model also simulated a capillary barrier in some locations nears the interface between the Topopah Springs welded tuff and the Calico Hills non-welded tuff in both the two- and three dimensional model domains. The result, as demonstrated in the transport studies, was that some radionuclides leaving the potential repository may be diverted laterally and travel above the Calico Hills. However, the increased length in flow path taken by

these radionuclides often served to substantially retard their movement relative to the fastest moving, nonsorbing solutes.

Accurately simulating such complex phenomena as thin capillary barriers at bedding interfaces requires an accurate characterization of the site properties. The use of naturally occurring isotopes should help to reduce uncertainty in specific rock and fracture properties employed in unsaturated zone flow and transport models. We demonstrated that varying the terms in the matrix-fracture interaction model can lead to drastically different matrix saturation predictions. Or, stated another way, similar saturation profiles can be predicted for greatly different infiltration rates by altering the value of a parameter for which there is great uncertainty.

Although significant progress in being made toward understanding the spatial and temporal distribution of infiltration into the unsaturated zone at Yucca Mountain (Hudson and Flint, 1995), there is still uncertainty associated with how much of the estimated shallow infiltration becomes net infiltration. Thus, in calibrating the site scale flow model, there is uncertainty in the boundary condition and the properties of the unsaturated fractured media. In particular the fault systems of Yucca Mountain require better characterization and study. We, and others, have demonstrated that it is possible to incorporate fault properties in flow and transport models and we can address their potential impact. However, there is still much uncertainty on how a fault actually affects the flow system.

As more and more complex flow processes are considered which lead to more and more complex solute transport models, the computational burden of addressing the processes increases. We have demonstrated in this report, that with our package of tools and sophisticated computing environment, we are well suited to address the challenges that lie ahead. Our computing environment includes automatic tools to readily update our models with new or improved geologic representations or engineering designs. We are capable of solving larger and better resolved site scale problems than have ever been performed on the Yucca Mountain Project. It is through these capabilities that we were able to more accurately prescribe the geologic structure of the zeolitized units in the Calico Hills. With our state-of-the-art simulation package, FEHM, we provided two- and three-dimensional dual permeability flow solutions and then computed the migration of ^{237}Np from the potential repository and ^{36}Cl from the surface. Though there is still much work to be done, it is our hope that this report will serve to help understand the flow and transport system at Yucca Mountain and guide future investigations.

8.3 Transport Results

The bulk of the calculations in the present study are transport simulations of the movement of ^{237}Np and conservative solutes from the potential repository to the water table. In addition to the

actual calculations, considerable effort went into synthesizing the works of many researchers studying the behavior of ^{237}Np and the hydrogeologic system. The key uncertainties of the transport system were then explored through systematic sensitivity analyses. Transport parameters such as the sorption coefficient, molecular diffusion coefficient, and the dispersivity were varied within the range of values determined from laboratory studies or from theoretical estimates. The impact of uncertainty in the extent of the zeolitic units of the Calico Hills was also examined. The link to the hydrologic studies discussed in the previous section is strong: several of the analyses explored the impact of variations of parameters that affect the hydrologic system. Two different model conceptualizations were also studied: the equivalent continuum and dual permeability model formulations. Each of these aspects of the transport analyses of the present study are discussed below.

Infiltration Rate and Position of Release. The infiltration rate exerts a strong influence on the travel times of conservative radionuclides (such as ^{99}Tc) and ^{237}Np. At an infiltration rate of 1 mm/y, the equivalent continuum model yields a median (50%) arrival time of between about 60-80 ky for a conservative solute and about 500-900 ky for ^{237}Np. The range depends on the position of release of the radionuclide. The ratio of conservative to ^{237}Np travel time is termed the Effective Retardation Factor (ERF). It represents the delay that can be attributed to sorptive retardation of ^{237}Np. The value of about 10 from these simulations is very typical of the simulations of the present study: there is roughly an order of magnitude difference in travel time between a conservative solute and ^{237}Np, a ratio that remains relatively constant (with a few exceptions) despite differences in the hydrologic system.

Travel times scale approximately with infiltration rate. If the infiltration rate is only 0.1 mm/y, travel times are long enough that radioactive decay of ^{237}Np reduces the concentrations to values such that more than 50% of the radionuclide never reaches the water table. Of course, at the highest infiltration rate studied (4 mm/y), travel times are correspondingly higher. Nonetheless, retardation of ^{237}Np is high enough that the two-dimensional continuum calculations indicate 50% travel times in excess of 100 ky even at this high infiltration rate.

The position of release of the radionuclide also impacts the travel time to the water table. In general, travel times from potential repository positions to the West of the Ghost Dance fault are larger than those to the East. There are several factors that lead to this behavior. First, the distance to the water table is greater for the Western segment. Furthermore, the thickness of the sorptive zeolites beneath the potential repository is greater in the West, so that sorption has a greater impact on reducing the migration rate of ^{237}Np. Finally, lateral flow tends to carry some radionuclides to

the East: release positions further West result in longer travel paths to the water table than those in the East.

Uncertainties in Sorptive Behavior. The two-dimensional calculations were also used to explore how sensitive the transport results are to uncertainties in the sorption behavior of ^{237}Np. The zeolitic tuffs of the Calico Hills hydrogeologic unit were shown in the section summarizing the laboratory work on ^{237}Np to be the only rock types where significant sorption occurs. The range of K_d values for the zeolitic units was 1.1 to 3.9, with the resulting transport times scaling more or less directly with the value of K_d chosen. We conclude that since the differences in measured K_d values occur even from samples collected in a close physical proximity, the average K_d value should probably be the one chosen to obtain a representative calculation of sorptive retardation of ^{237}Np. An important caveat to the transport results is that the chemical conditions in the flow and transport system must be similar to those conditions for which the K_d values were found to be significant, namely J-13 water at pH 7. If fluids are at significantly higher pH values with higher concentrations of competing ions such as Ca^{2+}, then sorption coefficients (and resulting travel times) for ^{237}Np will be lower. When the geochemical site characterization and modeling program provides more definitive results on the character of the unsaturated zone pore fluid, the calculations presented here can be used to assess the effect of geochemical behavior on transport.

Assigning small sorption coefficient values (within the range suggested by the data) to the non-zeolitic rocks was shown to have a relatively minor impact on the travel times because the impact is small compared to the large sorptive delay in the zeolitic units. This conclusion confirms statements by Project geochemists that further work characterizing sorption of ^{237}Np on vitric and devitrified tuffs is not necessary.

The assumed thicknesses of the zeolitic units in the Calico Hills has some impact on the transport of ^{237}Np. The thickness maps generated using the Stratamodel software (Figure 7-9) are an effective way to assess the impact of uncertainties in zeolite thicknesses. As a first approximation, if we assume vertical, downward transport, the maps show that reducing the uncertainty in zeolite thickness will provide more confidence in the longer travel times predicted in the Western part of the potential repository. However, since there is little difference in the zeolite thicknesses in the East, further study and characterization in this region will have little impact on ^{237}Np transport through the unsaturated zone from release points in the Eastern segment. This conclusion applies only to the characterization of the thickness of zeolitic units as it relates to ^{237}Np transport. Of course, there may be many other reasons to study the structural controls on the hydrogeologic system East of the potential repository, especially since many of the calculations show lateral movement of radionuclides in this direction.

DRAFT

Choice of Conceptual Model for Flow and Transport. Both equivalent continuum and dual permeability models were used to explore various aspects of the transport system, and just as importantly, to determine qualitatively the uncertainty associated with our choice of conceptual models. As discussed in the previous section, the dual permeability model predicts much more significant lateral diversion of flow above the potential repository, at the contact between the TCw and PTn units. The impact that this has on transport from the potential repository is significant: in general, less water percolates through the Western segment of the repository, and travel times increase accordingly. However, even in simulations in which the Ghost Dance fault is not explicitly represented in the model, the fault offset is reflected in the structural model as a flattening of the dipping to the East, resulting in increased vertical flow of laterally flowing fluid near the fault. Thus, the Easternmost positions of the Western segment result in much shorter travel times than points to the West. In the Eastern segment, travel times are shorter than in the West, and are shorter as one moves to positions further East. For example, 50% travel times at 1 mm/y for the dual permeability model range from about 1,000 ky to 6,000 ky for the Western Release points, while for the Eastern release points the times range from about 500 ky to 1400 ky.

These results have probably only been observed because of the faithful representation of thin hydrogeologic units in the grid generation step of the process. Structured finite difference grids would be incapable of reproducing this behavior unless exceedingly small grid spacings are used or special efforts are made to tilt the grid in the direction of the dipping beds. Of course, a residual uncertainty that should be addressed through modeling studies is the assumption of continuity of the stratigraphic units. Breaks in any of these thin units that support increased fracture flow would result in downward movement of flow at the point where the unit terminates.

This qualitative difference in transport results leads us to question whether equivalent continuum representations are adequate for predicting transport results. Since the dual permeability model relaxes the assumption of equilibrium of pressures in the fractures and matrix, we believe that it represents the flow and transport processes of an unsaturated, fractured rock mass more appropriately than the equivalent continuum model. The dual permeability approach also more naturally incorporates fracture-matrix solute transport models into the calculation than does an effective continuum approach. Thus the dual permeability model results presented here are thought to be more accurate, and in further studies we should continue to migrate toward these models for predicting flow and transport, despite the added computational burden.

Impact of Hydrologic Uncertainties. The sensitivity analyses of this sort, though not intended as the major focus of the present study, attempted to address some key uncertainties in the flow behavior as they impact transport of ^{237}Np and other radionuclides. The fracture-matrix interaction

term is crucial to predicting the transport behavior. If dual permeability flow models allow fractures to transmit flow at less than 100% matrix saturations, then the transport system is affected as well. This change in the flow model results in more prevalent vertical, downward flow through the potential repository, thus mitigating some of the beneficial effects of lateral diversion above the potential repository horizon. The result is a more uniform percolation of fluid through the potential repository and less variation in travel time with release position.

The simulation case of an explicitly represented Ghost Dance fault is one in which the fault zone acts as a drain for fluid moving laterally at the TCw-PTn contact. Travel times for release points to the West of the fault are not significantly affected. Points to the East show longer travel times because the percolation rate through this segment of the potential repository is lower when the fault acts as a fluid drain. Characterization of the behavior of the Ghost Dance fault is thus important to assess the effectiveness of the geologic barrier for the Eastern segment of the potential repository. This segment usually shows up in these calculations as more problematic from the standpoint of waste isolation because of this liquid flux effect, the relative thinness of the zeolitic rocks there, and the shorter travel path lengths for radionuclides moving laterally beneath the potential repository. If interruption of lateral flow at the Ghost Dance fault can be demonstrated, the travel time predictions for the Eastern segment of the potential repository improve (longer times).

Uncertainties in Transport Parameters. Another advantage of the dual permeability model formulation is that it allows for a more straightforward representation of rapid fracture transport using the particle tracking technique. Sorption in the bulk rock could be studied adequately using the dual permeability finite element solution, but the particle tracking feature of FEHM was needed for studying the parameters of matrix diffusion coefficient and fracture sorption coefficient. For conservative radionuclides, the arrival times at the water table are only significantly impacted by matrix diffusion when there is continuous transport in fractures of at least some of the solute. Whenever a unit is encountered along the flow path in which matrix flow predominates, the slower migration rates in this unit overwhelm the differences in travel times due to matrix diffusion in the units with substantial fracture flow. However, when all units along the path exhibit fracture flow and transport, matrix diffusion serves to increase the extremely short travel times predicted in the absence of diffusion.

Even if matrix diffusion in some cases has little impact on travel times of a conservative radionuclide, the effect on a sorbing species such as ^{237}Np is profound. For radionuclide traveling in a fracture, the only mechanism allowing it to contact rock where it can sorb is matrix diffusion. Thus the travel times of ^{237}Np generally exhibit the beneficial effects of sorption even when significant fracture flow occurs. The value of diffusion coefficient has the expected impact on the

transport results: higher diffusion coefficients result in greater contact of ^{237}Np with the sorptive zeolites and concomitant longer travel times.

Fracture sorption appears to play a relatively minor role in the transport of ^{237}Np. Even fracture retardation factors of order 70 do little to change the travel times compared to a case in which no fracture sorption is assumed. The reason is that whenever matrix diffusion is assumed, the delay in travel time caused by diffusion and sorption on the matrix rock overwhelms any beneficial effects of fracture sorption until the fracture retardation factor approaches values of order 10,000. This conclusion must be tempered by the fact that the model used here restricts fracture sorption to the fracture face itself. If the sorptive minerals found in the fractures penetrate the matrix rock adjacent to the fracture even a few centimeters, the impact of this sorption would become substantial. Therefore, a careful examination of the distribution of the sorptive minerals is required before ruling out fracture sorption as an important process. In addition, this conclusion applies only to ^{237}Np at the fracture retardation factor estimated from a single laboratory measurement. Future measurements on ^{237}Np and other radionuclides will provide more information to strengthen this analysis.

Three Dimensional Effects. Although many of the sensitivity analyses in the present study were carried out in two dimensions, a select number of three-dimensional radionuclide migration calculations were performed to assess any differences that might arise to make the two-dimensional analyses inaccurate or non-conservative. In general, there are three-dimensional effects, but except for a few instances described below, they should not invalidate the conclusions of the sensitivity analyses performed in two dimensions.

In both equivalent continuum and dual permeability three-dimensional calculations, the three-dimensional simulations result in a greater degree of lateral diversion of flow. The reason for this difference will be the subject of further study, but it seems clear that the complex hydrostratigraphy in three dimensions provides additional complex and tortuous pathways that do not appear when a two-dimensional slice is taken through the same system.

The impact on transport of radionuclides from the potential repository depends on the location of the lateral diversion. Much of this effect occurs above the potential repository, resulting in lower percolation fluxes through the repository horizon and longer travel times than in the two-dimensional calculations. There are also some effects observed in flow and transport beneath the potential repository due to increased lateral flow. The predicted 50% travel times to the water table for conservative radionuclides increase dramatically in three dimensions versus two dimensions (up to a factor of eight for the equivalent continuum model for some release positions). However, this

beneficial lateral diversion comes at the expense of a decreased contact of ^{237}Np in the zeolitic units, which are to some extent bypassed for some of the release positions.

This effect is obviously important for making accurate predictions of ^{237}Np transport. It is uncertain whether the effect just discussed is a pervasive effect that will be seen for all three-dimensional transport calculations or if it is an isolated result that will not be reproduced for different assumed model geometries and flow characteristics. For example, when faults are explicitly represented in three dimensions, they may arrest the lateral movement of ^{237}Np, forcing them to travel through the more sorptive units. This effect was shown in the two-dimensional simulations with the fault explicitly represented. Furthermore, the fracture-matrix interaction term was shown in two-dimensional simulations to affect the relative amount of lateral diversion: when fractures flow at lower matrix saturations, there is less lateral diversion. This too would result in greater contact of ^{237}Np with the zeolitic rocks beneath the potential repository. Future studies that simulate the transport system will rely more heavily on three dimensional analyses using the dual permeability model formulation to account for fracture flow and transport more realistically.

Code Considerations. The combination of grid generation capabilities of the Stratamodel/ GEOMESH interface, when coupled to the FEHM flow and transport simulator, has proven to be a robust and versatile suite of software tools for modeling unsaturated zone flow and transport. The result is the ability to spend more time performing analyses of the flow and transport system. One key element of this strategy is the construction of finite element grids that not only preserve the specified structure of the hydrostratigraphic system, but also honor numerical conditions needed to perform accurate numerical simulations. Many grid generation packages do not consider one or the other of these requirements.

The FEHM code has been shown to provide flow and transport solutions on grids containing up to 51,000 nodes and 300,000 elements in three dimensions for equivalent continuum, and 14,000 nodes and 78,000 elements in three dimensions for dual permeability. The number of equations in each of these simulations was double the number of nodes for equivalent continuum and four times the number of nodes for dual permeability. The limitation reached at this point was a memory limitation on the computers being used, rather than a cpu time issue. Increasing the problem size further should not be a major issue. However, the sort of resolution needed in the two-dimensional transport solution implies that further code improvements may be required for finely resolved, three-dimensional transport calculations of the order of 500,000 nodes.

The particle tracking transport option of FEHM was shown to be a robust method for performing transport calculations. In most cases computational speed is not an issue: to a first approximation, the cpu time scales with the number of particles used, rather than the number of grid points or

elements. Furthermore, in dual permeability mode, the particle tracking option accurately accounts for the disparate travel times in the fractures and matrix, dividing the particles in the two media in proportion to the relative flow rates. For particles remaining in the fractures, the matrix diffusion transport option allows this important process to be simulated properly, as long as the solute has insufficient time to diffuse to the centerline between two fractures. When this is not the case, the model will overestimate travel times because the analytical solution defining the transport is invalid. Other analytical solutions representing the case of pervasive diffusion within the matrix blocks will be added to future versions of the code to allow a wider range of transport situations to be modeled accurately.

The finite element solute transport model option is more appropriate for modeling the case of larger dispersivity transport systems, as the assumption used to simulate dispersion for particle tracking breaks down at high dispersivities. Another advantage of the finite element transport solution that was not used extensively in this study is the reactive transport option, which simulates the transport of multiple interacting species. As our understanding of the geochemical transport system improves, the sorption coefficient models will gradually be supplanted by more robust chemical transport models. For ^{237}Np, the next generation of transport simulations should include the temperature and chemistry-dependent speciation of ^{237}Np into sorptive and non-sorbing ions as studied by Nitsche et al. (1993, 1994), as well as an ion exchange model for sorption of NpO_2^+ to the zeolitic rocks of the Calico Hills formation as studied by Tate et al. (1995). The reactive transport model of FEHM will allow these calculations to be performed when our understanding of the chemical systems has improved.

DRAFT

9.0 References

Andrews, R. W., T. F. Dale, and J. A. McNeish. Total System Performance Assessment - 1993: An Evaluation of the Potential Yucca Mountain Repository, Civilian Radioactive Waste Management System M&O Contractor Document Number B00000000-01717-2200-00099-Rev.01, March, 1993.

Bentley, H.W., F.M. Philips, and S.N. Davis. Chlorine-36 in the terrestrial environment. In Handbook of Environmental Isotope Geochemistry, IIB, J.C. Fontes and P. Fritz, eds., Elsevier, AMsterdam, pp. 427-480, 1986.

Bern, M. and D. Eppstein, Mesh generation and optimal triangulation, In D. Z. Du and F. Hwang, editors, Computing in Euclidean Geometry, Volume 1 of Lecture Notes Series on Computing, pages 23-90, World Scientific, Singapore, 1992.

Birdsell, K.H., K. Campbell, K.G. Eggert, and B.J. Travis. Simulation of radioactive retardation at Yucca Mountain using a stochastic mineralogical/geochemical model, Proceedings of the fourth international high level radioactive waste management conference, Las Vegas, Nevada, Americal Nuclear Society, La Grange Park, Ill., pp. 153-162., 1990.

Birdsell, K.H., K.G. Eggert, and B.J. Travis. Three-dimensional simulations of radionuclide transport at Yucca Mountain, *Radioactive Waste Management and Environmental Restoration*, 19:165-192, 1994.

Brigham, W. E.Mixing Equations in Short Laboratory Cores, *Soc. Pet. Eng. J.*, 14:91-99, 1974.

Broecker, W.S., T.H. Peng, and R. Engh. Modeling the carbon system, *Radiocarbon*, 22:565-598, 1980.

Brownell, D. H., S. K. Garg, and J. W. Pritchett. Computer Simulation of Geothermal Reservoirs, Paper SPE 5381, *Proceedings of the 45th California Regional Meeting of the Soc. Pet. Eng. of AIME*, Ventura, California (1975).

Combes, J. M., C. J.Chisholm-Brause, G. E. Brown, G. A. Parks, S. D. Conradson, P. G. Eller, I. R. Triay, D. E. Hobart, and A. Meijer. X-ray Absorption Spectroscopy Study of Neptunium (V) Sorbed at the α-FeOOH/Water Interface, *Environmental Science and Technology*, 26:376-382, 1992.

Conca, J. L., and J. Wright. Diffusions Coefficients in Gravel Under Unsaturated Conditions, *Water Resour. Res.*, 26:5:1055-1066, 1990.

Corey, A. T.. The Interrelation Between Gas and Oil Relative Permeabilities, *Prod. Mon.*, 19:38-41, 1954.

Dash, Z. V., B. A. Robinson, and G. A. Zyvoloski. V&V Plan and Procedures for the FEHMN Application, Los Alamos National Laboratory Report No. LA-UR-95-2064, June, 1995.

Dash, Z. V., B. A. Robinson, and G. A. Zyvoloski. V&V Report for the FEHMN Application, Los Alamos National Laboratory Report No. LA-UR-95-2063, June, 1995.

DOE, Strategy for Demonstration of Waste Containment and Isolation, Yucca Mountain Project position paper, August 14, 1995.

Fabryka-Martin. J.T., B.A. Robinson, E.W. Vestal, and S.J. Wightman. Infiltration processes at Yucca Mountain infered from chloride and chlorine-36 distributions,Technical Report LA-12970-MS, Los Alamos National Laboratory, 1995.

Fabryka-Martin. J.T. and B. Liu, Distribution of chlorine-36 in UZ-14, UZ-16, perched water, and the ESF north ramp, Yucca Mountain, Nevada, Yucca Mountain Project milestone report 3431, 1995.

Gable, C. W., H. Trease, T. Cherry, Automatic Grid Generation From Complex Models Of Geologic Structure And Stratigraphy, GSA, abstract, LA-UR-95-2482, 1995.

Gable, C. W. G. Zyvoloski, Site Scale Modeling of Radionuclide Transport At Yucca Mountain, NV: Grid Generation and Reactive Tracers, Los Alamos National Laboratory Report No. LA-UR-94-1041, 1994.

Gable, C. W., G. A. Zyvoloski, and B. A. Robinson, Integration of hydrostratigraphic data in reactive transport models, Chapman Conference on Hydrogeologic Processes: Building and Testing Atomistics- to Basin-Scale Models, Lincoln, New Hampshire, 1994.

George, D.C. and H. E. Trease, The X3D User's Manual, *Los Alamos National Laboratory Report, LAUR-95-3608, November 1995.*

Glass, R. J., and M.J. Nicholl. Quantitative Visualization of Entrapped Phase Dissolution Within a Horizontal Flowing Fracture, *Geophys. Res. Lett.*, Special Issue, Multiphase Flow in Fractured Rock, 1995.

Goltz, M. N., and P. V. Roberts. Using the Method of Moments to Analyze Three-Dimensional Diffusion-Limited Solute Transport From Temporal and Spatial Perspectives, *Water Resour. Res.*, 23:8:1575-1585, 1987.

Hevesi, J.A. and A.L. Flint. A geostatistical model for estimating precipitation and recharge for the Yucca Mountain region, Nevada-California: U.S. Geological Society Open-File Report 95-xxxx, (in review), 1995.

Ho, C.K. Assessing alternative conceptual models of fracture flow, Technical Report Sand95-0324C, Sandia National Laboratories, 8p. 1995..

Hudson, D.B. and A.L. Flint, Estimation of shallow infiltration and presence of potential fast pathways for shallow infiltration in the Yucca Mountain area, Nevada, United States Geological Survey, Open File Report *in review*, 1995.

DRAFT

Khamayseh, A. and A. P. Kuprat, Anisotropic Smoothing and Solution Adaption for Unstructured Grids, Los Alamos National Laboratory Report No. LA-UR-95-2205, International Journal for Numerical Methods in Engineering, (submitted).

Klavetter, E. A., and R. R. Peters. Estimation of Hydrologic Properties of an Unsaturated Fractured Rock Mass, Sandia National Laboratories Report SAND84-2642, 1986.

Kuprat, A. P., D. C. George, E. J. Linnebur, R. K. Smith and H. E. Trease, Moving Adaptive Unstructured 3-D Meshes in Semiconductor Process Modeling Applications, *to be published* 1995.

Liu, B., J. Fabryka_Martin, A. Wolfsberg, B. Robinson, and P. Sharma.Significance of apparent discrepancies in water ages derived from atmospheric radionuclides at Yucca Mountain, Nevada, Technical Report LA-UR-95-572, Los Alamos National Laboratory, 11 p., 1995.

Loeven, C.. A Summary and Discussion of Hydrologic Data from the Calico Hills Nonwelded Hydrogeologic Unit at Yucca Mountain, Nevada, Los Alamos National Laboratory Report No. LA-12376-MS, January, 1993.

Maloszewski, P., and A. Zuber. Tracer Experiments in Fractured Rocks - Matrix Diffusion and the Validity of Models, *Water Resour. Res.*, 29:8:2723-2735, 1993.

Meijer, A.. A Strategy for the Derivation and Use of Sorption Coefficients in Performance Assessment Calculations for the Yucca Mountain Site, in *Proceedings of the DOE/YMP Radionuclide Sorption Workshop at Los Alamos National Laboratory*, September 11-12, 1990, Los Alamos National Laboratory Report No. LA-12325-C, August, 1992.

Mercer, J. W., and C. R. Faust. Simulation of Water- and Vapor-Dominated Hydrothermal Reservoirs, Paper SPE 5520, *Proceedings of the 50th Annual Fall Meeting of the Soc. Pet. Eng. of AIME*, Dallas, Texas, 1975.

Moench, A. F.. Double-Porosity Models for a Fissured Groundwater Reservoir with Fracture Skin, *Water Resour. Res.*, 20:7:831-846, 1984.

Montazar, P., and Wilson,W.E., Conceptual Hydrologic Model of Flow in the Unsaturated Zone,Yucca Mountain, Nevada, Water Resources Investigations Report 84-4355,U.S. Geological Survey,1984.

Moridis, G. and K. Pruess. Flow and Transport Simulations using T2CG1, a package of conjugate gradient solvers for the TOUGH2 family of codes, Lawrence Berkeley Laboratory Report No. LBL 36235, April 1995.

Neretnicks, I.. Diffusion in the Rock Matrix: An Important Factor in Radionuclide Migration? *J. Geophys. Res.*, 85:B8:4379-4397, 1980.

Nicholl, M. J., R. J. Glass, and S. W. Wheatcraft. Gravity-Driven Infiltration Instability in Initially Dry Nonhorizontal Fractures. *Water Resour. Res.*, 30:9:2533-2546, 1994.

Nitsche, H., R. C. Gatti, E. M. Standifer, S. C. Lee, A. Muller, T. Prussin, R. S. Deinhammer, H. Maurer, K. Becraft, S. Leung, S. A. Carpenter. Measured Solubilities and Speciations of Neptunium, Plutonium, and Americium in a Typical Groundwater (J-13) from the Yucca Mountain Region, Los Alamos National Laboratory Report Number LA-12562-MS, July, 1993.

Nitsche, H., K. Roberts, T. Prussin, A. Muller, K. Becraft, D. Keeney, S. A. Carpenter, R. C. Gatti. Measured Solubilities and Speciations from Oversaturation Experiments of Neptunium, Plutonium, and Americium in UE-25p#1 Well Water from the Yucca Mountain Region, Los Alamos National Laboratory Report Number LA-12563-MS, April, 1994.

Ortiz, T.S. et al. A three-dimensional model of reference thermal maechanical and hydrological stratigraphy at Yucca Mountain, Southern Nevada, Technical Report SAND84-1076, Sandia National Laboratories, 76 p., 1985.

Plummer, L. N., and E. Busenberg. The Solubilities of Calcite, Argonite, and Vaterite in CO_2-H_2O Solutions Between 0 and 90°C, and an Evaluation of the Aqueous model for the System CaCO3-H2O, *Geochim. et Cosmochim. Acta*, 46:1101, 1982.

Pruess, K., J. S. Y. Wang, and Y. W. Tsang. On Thermohydrologic Conditions Near High-Level Nuclear Wastes Emplaced in Partially Saturated Fractured Tuff 2. Effective Continuum Approximation, Water Resour. Res., 26:6:1249-1261, 1990.

Pruess, K. TOUGH2 - A general purpose numerical simulator for multiphase fluid and heat flow, Technical Report, LBL-29400, Lawrence Berkeley National Laboratory, 103 p., 1990.

Reeves,M.(ed), Review and Selection of Unsaturated Flow Models", Intera Document B00000000-01425-2250-00001 Rev. 00, 1993.

Reimus, P. W.. The Use of Synthetic Colloids in Tracer Transport Experiments in Saturated Rock Fractures, Ph.D. Dissertation, University of New Mexico, Albuquerque, New Mexico, 1995.

Rockhold, M.L., B. Sager, and M.P. Connelly. Multi-dimensional modeling of unsaturated flow in the viscinity of exploratory shafts and fault zones at Yucca Mountain, Nevada, Proceedings of the first international high level radioactive waste management conference, Las Vegas, Nevada, American Nuclear Society, La Grange Park, Ill., pp. 1192-1199. 1990.

Robinson, B. A.. A Strategy for Validating a Conceptual Model for Radionuclide Migration in the Saturated Zone Beneath Yucca Mountain, *Rad. Waste Manag. Environ. Restor.*, 19:73-96, 1994.

Robinson, B. A., and S. E. Henderson. A Cell-Based Particle Tracking Technique for Solute Transport in Porous Media, to be submitted to *Groundwater*, 1995.

Rogers, P. S. Z., and S. Chipera. Sorption Characteristics of Yucca Mountain Tuffs as a Function of Sample Particle Size, Surface Area, and Water Composition, Los Alamos National Laboratory Report No. LA-12805-MS, 1994.

Rulon, J., G.S. Bodvarsson, and P. Montazer. Preliminary numerical simulations of groundwater flow in the unsaturated zone, Yucca Mountain, Nevada, Technical Report LBL-20553, Lawrence Berkeley National Laboratory, 91 p., 1986.

Scott, R.B. and J. Bonk. Preliminary geologic map of Yucca Mountain with geologic sections, Nye County, Nevada, scale 1:12000, U.S. Geological Survey Open-File Report 84-494, 1984.

Starr, R. C., R. W. Gillham, and E. A. Sudicky. Experimental Investigation of Solute Transport in Stratified Porous Media 2. The Reactive Case, *Water Resour. Res.*, 21:7:1043-1050, 1985.

Tang, D. H., E. O. Frind, and E. A. Sudicky. Contaminant Transport in Fractured Porous Media: Analytical Solution for a Single Fracture, *Water Resour. Res.*, 17:3:555-564, 1981.

Tait, C.D., S. A. Ekberg, D. L. Clark, P. D. Palmer, I. R. Triay, and C. R. Cotter. Sorption as a function of groundwater chemistry to elucidate sorption mechanisms, Milestone Report to the Yucca Mountain Site Characterization Project #3219, September 30, 1995.

Tidwell, V. C., R. J. Glass, and W. Peplinski. Laboratory Investigation of Matrix Imbibition from a Flowing Fracture, *Geophys. Res. Lett.*, Special Issue, Multiphase Flow in Fractured Rock, 1995.

Trease, H.E., Three-Dimensional Free Lagrangian Hydrodynamics, *Proceedings of first Free-Lagrange Conference, Leture Notes in Physics, Springer-Verlag, Vol. 238, 1985.*

Trease, H.E. and Dean, S.H., Thermal Diffusion in the X-7 Three-Dimensional Code, *Proceedings of the Next Free-Lagrange Conference*, Jackson Lake Lodge, Wyoming, June 3-7, 1990, Springer-Verlag Press, Vol. 395, pp. 193-202.

Trease, H.E. Parallel Nearest Neighbor Calculations, *Proceedings of the first Free-Lagrange Conference, Lecture Notes in Physics*, Springer-Verlag, 395:149-156, 1990.

Trease, H.E. X3D: A Time-Dependent, 3-D, Adaptive, Unstructured Grid Generation ToolBox, *to be published Los Alamos National Laboratory 1995.*

Triay, I. R., K. H. Birdsell, A. J. Mitchell, and M. A. Ott. Diffusion of sorbing and non-sorbing radionuclides in tuff, in Proceedings of the Fourth Annual International Conference on High-Level Radioactive Waste Management, April 26 - 30, 1993, Las Vegas, NV, Vol. 2, pp 1527-1532, 1993.

Triay, I. R., C. R. Cotter, M. H. Huddleston, D. E. Leonard, S. C. Weaver, S. J. Chipera, D. L. Bish, A. Meijer, J. A. Canepa. Neptunium Transport through Yucca Mountain Tuffs I: Batch Sorption Results, Los Alamos National Laboratory Yucca Mountain Project Milestone No. 3349, 1994a.

Triay, I. R., A. Furlano, S. C. Weaver, S. J. Chipera, D. L. Bish. Report on the Study of Kinetic Effects using Crushed Tuff Columns: Neptunium in sodium Bicarbonate Waters, Los Alamos National Laboratory Yucca Mountain Project Milestone No. 3041, 1994b.

Triay, I. R., A. Furlano, and M. Espinosa. Diffusion of neptunium through saturated tuffs, Milestone Report to the Yucca Mountain Site Characterization Project #4034, September 30, 1994c.

Tsang, Y.W.,K. Pruess,,and J. S. Y. Wang, The Role of Faults Zones in Affecting Multiphase Flow at Yucca Mountain,Proceedings of the Fourh International High-level radioactive Waste management Conference, Las Vegas, NV, pp 660-666. April 26-30, 1993.

Valocchi, A. J.. Validity of the Local Equilibrium Assumption for Modeling Sorbing Solute Transport Through Homogeneous Soils, *Water Resour. Res.*, 21:6:808-820, 1985.

van Genuchten, M. T.. A Closed Form Equation for Predicting Hydraulic Conductivity of Unsaturated Soils, *Soil Sci. Soc. Am. J.*, 44:892-898, 1980.

Viswanathan, H. S., Modification of the Finite Element Heat and Mass Transfer Code (FEHMN) to Model Multicomponent Reactive Transport, M.S. Thesis, University of Illinois, Champaign-Urbana, Illinois, September, 1995.

Wang, J.S., and T.N. Narisimhan. Hydrologic modeling of vertical and lateral movement of partially saturated fluid flow a fault zone at Yucca Mountain, Nevada, Technical Report SAND-87-7070, Sandia National Laboratories and LBL-23510, Lawrence Berkeley National Laboratory, 98 p. 1987.

Wang, J.S. Variations of hydrological parameters of tuff and soil, Proceedings of the third international conference on high level radioactive waste management, Las Vegas, Nevada, Americal Nuclear Society, La Grange Park, Ill., pp. 77-731. 1992.

Ware, S. D. and I. R. Triay. Transport of radionuclides through natural fractures under saturated conditions, Milestone Report to the Yucca Mountain Site Characterization Project #3063, September 30, 1995.

Warren, J. E., and P. J. Root. The Behavior of Naturally Fractured Reservoirs, *Soc. Pet. Eng. J.*, 3:245-255, 1963.

Wilson, M. L., et al.. Total-System Preformance Assessment for Yucca Mountain - SNL Second Iteration (TSPA-1993), Sandia National Laboratory Report SAND93-2675, April, 1994.

Wittwer C., G. Chen, G.S. Bodvarsson, M. Chornack, A. Flint, L. Flint, E. Kwicklis, and R. Spengler. Prelinary development of the LBL/USGS three-dimensional site-scale model of Yucca Mountain, Nevada, Technical Report LBL-37356/UC-814, Lawrence Berkeley National Laboratory, Berkely, CA, 1995.

DRAFT

Yang, I.C. Status of H-3, C-14, and stable isotope studies to date groundwater in the unsaturated zone at the proposed Yucca Mountain site - results and interpretations. Presented in Las Vegas, NV on 20-21 October, 1994 to the Advisory Committee on Nuclear Waste (ACNW), 1994.

Yang, I.C., G. Rattray, and P. Yu, Chemical and Isotopic data and interpretations, unsaturated-zone boreholes, Yucca Mountain, Nevada. U.S. Geologic Survey, Water Resources Investigation Report, (in prep), 1995.

Zyvoloski, G. A., B. A. Robinson, Z. V. Dash, and L. L. Trease. Users Manual for the FEHMN Application, Los Alamos National Laboratory Report No. LA-UR-94-3788, Rev. 1, July, 1995.

Zyvoloski, G. A., B. A. Robinson, Z. V. Dash, and L. L. Trease. Models and Methods Summary for the FEHMN Application, Los Alamos National Laboratory Report No. LA-UR-94-3787, Rev. 1, March, 1995.

Cover Design: Kay L. Coen

Illustrations (clockwise from left):

1. Stratigraphic contour map of base of Calico Hills Zeolitic unit in meters.

2. 3-D framework model of Yucca Mountain hydrostratigraphy and 2-D finite element grid.

3. Apparent ages of pore fluid in model of Cl-36 infiltration.

4. PA abstraction: breakthrough times to water table for 5% of Np-237.

Los Alamos National Laboratory, an affirmative action/equal opportunity employer, is operated by the University of California for the U.S. Department of Energy under contract W-7406-ENG-36.

This report was prepared as an account of work sponsored by an agency of the United States Government. Neither The Regents of the University of California, the United States Government nor any agency thereof, nor any of their employees, makes any warranty, express or implied, or assumes any legal liability or responsibility for the accuracy, completeness, or usefulness of any information, apparatus, product, or process disclosed, or represents that its use would not infringe privately owned rights. Reference herein to any specific commercial product, process, or service by trade name, trademark, manufacturer, or otherwise, does not necessarily constitute or imply its endorsement, recommendation, or favoring by The Regents of the University of California, the United States Government, or any agency thereof. The views and opinions of authors expressed herein do not necessarily state or reflect those of The Regents of the University of California, the United States Government, or any agency thereof.